SAND88—0660 • UC—70
Unlimited Release
Printed December 1988

SAND--88-0660

DE89 009001

Yucca Mountain Project

Compliance and Strength of Artificial Joints in Topopah Spring Tuff

William A. Olsson

Prepared by
Sandia National Laboratories
Albuquerque, New Mexico 87185 and Livermore, California 94550
for the United States Department of Energy
under Contract DE-AC04-76DP00789

"Prepared by Yucca Mountain Project (YMP) participants as part of the Civilian Radioactive Waste Management Program (CRWM). The YMP is managed by the Yucca Mountain Project Office of the U. S. Department of Energy, Nevada Operations Office (DOE/NV). YMP work is sponsored by the Office of Geologic Repositories (OGR) of the DOE Office of Civilian Radioactive Waste Management (OCRWM)."

Issued by Sandia National Laboratories, operated for the United States Department of Energy by Sandia Corporation.

Printed in the United States of America
Available from
National Technical Information Service
U.S. Department of Commerce
5285 Port Royal Road
Springfield, VA 22161

NTIS price codes
Printed copy: A07
Microfiche copy: A01

DISCLAIMER

Portions of this document may be illegible in electronic image products. Images are produced from the best available original document.

Distribution
Category UC-70

SAND88-0660
Unlimited Release
Printed December 1988

COMPLIANCE AND STRENGTH OF ARTIFICIAL JOINTS IN TOPOPAH SPRING TUFF

William A. Olsson

Geomechanics Division
Sandia National Laboratories
Albuquerque, New Mexico 87185

ABSTRACT

This report establishes the data base for an experimental program to determine the compliance and friction stress of dry sawcuts in Topopah Spring tuff. Friction stresses and compliances of a rough joint are also included. For constant normal stress tests, the friction stress is approximately proportional to the normal stress over the normal stress range of 1 to 6 MPa. The proportionality constant (coefficient of friction), computed from the maximum friction stress at any normal stress, is sensitive to initial surface state and any nonuniformity in normal stress as a result of inexact alignment. This sensitivity to initial conditions raises the question of how best to acquire meaningful data from real joints.

The data presented in this report was collected prior to the implementation of the Project Quality Assurance (QA) Plan at Sandia National Laboratories and, therefore, the QA Level of the data collection process is "TBD". The report itself, however, was prepared under a QA Level 3 Activity within WBS element 1.2.4.2.1.3.

Contents

List of Figures

1 INTRODUCTION

Capabilities for predicting the response of rock masses to thermomechanical loadings are being developed under the Yucca Mountain Project (YMP) for the design of an underground nuclear waste repository at Yucca Mountain on the Nevada Test Site (NTS). An important ingredient in the computer codes being used is the constitutive description of the mechanical discontinuities (mostly joints, but also bedding planes and faults). This report summarizes preliminary laboratory experimental data on the compliance and the friction stress of artificial joints in Topopah Spring tuff in the air-dry, room-temperature condition. Also, data for a laboratory-induced, clean tensile fracture are given.

Details of the analysis of the results are discussed in earlier reports [*Olsson*, 1987a,b]. Therefore, the reader is urged to judiciously use data in this report, consulting the earlier documents when necessary. This report is primarily a catalogue of experiments and a summary of results; hence, little further analysis is given.

Because of the exploratory nature of the investigation, a systematic data base was not developed for the variables (such as sliding velocity, amount of slip, and normal stress history) studied. The results suggest guidelines for further, more systematic, experimentation on fracture properties.

It is critical to clearly understand the nature of the data and their implication; therefore, in the next section the constitutive relations for a joint are defined and the methods for their determination are explained.

1.1 Constitutive Relations

Joint constitutive models are usually based on a displacement decomposition that separates recoverable (elastic) from nonrecoverable (plastic) slip. This leads to the supposition of a stiffness matrix [*Goodman and Dubois*, 1972; *Thomas*, 1982; *Plesha*, 1985; *Chen*, 1986] or its inverse, the compliance matrix [*Sun* et al., 1985]. It is assumed that there exists a 3×1 matrix of relative elastic displacements, δ_i, one normal and two tangential components, caused only by the joint such that

$$\delta_i = C_{ij}\sigma_j \ , \tag{1}$$

where C_{ij} is a 3×3 matrix of compliances, and σ_j is the 3×1 matrix of stress. In the experiments the maximum resolved shear stress is coaxial with the maximum principal slip, and therefore only 2 components each of stress and relative displacement, one

normal and one tangential, need to be considered. The compliance matrix then has only 4 nonzero components. For clarity let the 1 and 2 directions be denoted t and n for tangential and normal, respectively. The deformation of the intact rock between the joints is usually assumed to be an additive elastic component of the total rock-mass deformation. A slip condition that identifies states of stress for which slip occurs is also needed, along with some type of flow rule that governs slip in the plastic regime.

The experimental results for ground surfaces show that there is little elastic shear contribution from the joint, only nonrecoverable (plastic) relative shear displacement (slip). In contrast, a nonlinear elastic component predominates the plastic component of the normal displacement. The above-mentioned type of constitutive model is convenient for computations, but from the viewpoint of an experimentalist, it lacks a complete description of known behavior. Therefore, to more adequately describe the observed response, it is necessary to explicitly introduce the slip condition into the stress-deformation law. To this end, it is useful to make an analogy with the development of an elastic-plastic constitutive law for intact rock [*Rice*, 1975; *Rudnicki and Rice*, 1975]. The model developed below is not intended to supplant that being used in calculations, but rather to clearly define and identify what needs to be measured in the laboratory.

First, because both elastic and plastic joint deformations may occur, the displacement increments should be decomposed as

$$d\delta_t = d\delta_t^e + d\delta_t^p \,, \tag{2}$$

where $d\delta_t^e$ and $d\delta_t^p$ are the tangential elastic and plastic increments, respectively. The normal displacement is

$$d\delta_n = d\delta_n^e + d\delta_n^p \,. \tag{3}$$

The plastic normal displacement is due to irreversible crushing of asperities and frictional effects. The elastic components of displacements are related to the stresses by

$$d\delta_t^e = C_{tt}^e \, d\tau \tag{4}$$

$$d\delta_n^e = C_{nn}^e \, d\sigma \,, \tag{5}$$

where C_{tt}^e and C_{nn}^e are the elastic shear and normal compliances, respectively. These are determined in elastic unloading cycles. The abbreviations $\sigma_t = \tau$ and $\sigma_n = \sigma$ have also been introduced.

The plastic components of slip are related to stress as follows. Assume that the tangent to the slip condition at any normal stress is given by $\tau = c + \mu^* \sigma$, where c is the stress-dependent cohesion and μ^* is the slope of the tangent. The elementary definition of the coefficient of friction is $\mu = \tau_f / \sigma$. When the friction stress, τ_f, is zero at $\sigma = 0$,

$\mu^* \sim \mu$ for $\sigma \to 0$. For the remainder of the paper, no distinction is made between μ^* and μ because the data are nearly linear. In the stress-displacement diagram the inverse slope of the initial linear part is the elastic compliance C^e_{tt}. The plastic compliance, C^p_{tt}, is such that the total compliance during slip hardening is $C_{tt} = C^e_{tt} + C^p_{tt}$. At constant normal stress, $d\sigma = 0$, and $d\delta^p_t = C^p_{tt}\, d\tau$. Thus, when the stress state lies wholly within the slip condition, the elastic compliance describes the behavior; when the stress state lies on the slip condition, an added contribution to the displacement is given by the plastic compliance in conjunction with the quantity

$$d\tau - \mu d\sigma \begin{cases} \leq 0, & \text{elastic unloading} \\ > 0, & \text{slip with hardening} . \end{cases} \tag{6}$$

Normal joint displacements during shear are accounted for by introducing $\beta = d\delta^p_n / d\delta^p_t$, where β is called the dilatancy factor. During slip, $d\delta^p_n = \beta C^p_{tt}(d\tau - \mu d\sigma)$.

Substituting the expressions for stress into the displacement decomposition equations, 2 and 3, the constitutive equation reads

$$d\delta_t = C^e_{tt}\, d\tau + C^p_{tt}(d\tau - \mu\, d\sigma) \tag{7}$$

$$d\delta_n = \beta C^p_{tt}(d\tau - \mu d\sigma) + C_{nn}\, d\sigma . \tag{8}$$

It is shown in the results section that $C^e_{tt} \ll C^p_{tt}$. Contrary to the shear compliance, the normal compliance is mostly (nonlinear) elastic at stresses achieved in this study (about 6 MPa) such that $C^e_{nn} \gg C^p_{nn}$ [*Olsson*, 1987b].

The appropriate types of tests may be discerned from the constitutive law by rearranging Equations 7 and 8 to

$$\begin{aligned} d\delta_t &= - \mu C^p_{tt}\, d\sigma + (C^e_{tt} + C^p_{tt})\, d\tau \\ d\delta_n &= (-\beta C^p_{tt}\mu + C_{nn})\, d\sigma + \beta C^p_{tt}\, d\tau , \end{aligned} \tag{9}$$

so that by holding σ constant, for example, and varying τ, one obtains C^e_{tt}, C^p_{tt}, and β.

The implications of Equation 9 can be understood by a term-by-term examination of the coefficients of the stresses on the right-hand side. The coefficient, μC^p_{tt}, gives the increment in slip, $d\delta_t$, that results from an increment in σ. It would evidently require a somewhat contrived surface geometry, such as a sawtooth shape with both surfaces having the same wavelength and slightly offset so that normal stress increments would cause a "downhill slide." The direct effect of shear stress increments is given by $(C^e_{tt} + C^p_{tt})$. As mentioned, evidence is presented later to show that $C^e_{tt} \approx 0$. Increments in

normal stress are related to increments in normal displacement through $-\beta C^p_{tt}\mu + C_{nn}$. The direct part, C_{nn}, is composed mostly of nonlinear elastic response with smaller contributions from plastic behavior at higher stress. The term $-\beta C^p_{tt}\mu$ admits the possible occurrence of an additional normal closure increment caused by tangential slip. Finally, βC^p_{tt} is the dominant dilatancy coefficient. For smooth surfaces, this is likely to be negligible; it can be significant for rough surfaces.

Equation 9 suggests that there are 6 important coefficients (or functions) that need to be determined: β, μ, C^p_{tt}, C^e_{tt}, C^p_{nn}, and C^e_{nn}. This experimental program provided limited data on β, which were reported earlier [*Olsson*, 1987b] and are not repeated here.

2 APPARATUS AND PROCEDURES

2.1 Test Machine

Tests were done in a rotary shear machine that consisted of a load frame containing a hydraulic rotary actuator in series with a hydraulic linear actuator. The maximum torque capacity was 7000 N-m and the maximum axial force was 900 kN. These actuators were independently servocontrolled by 410 function generators and 442 controllers from *MTS Systems, Inc.* Angle of rotation, axial load, and torque are calibrated yearly by *MTS Systems, Inc.*

In each test, the far-field twist angle, torque, and axial force were recorded by a data acquisition computer and stored on a floppy disk using software described by *Holcomb and Jones* [1983]. The data were transferred immediately to a mainframe computer where they are stored indefinitely for analysis and plotting. When analysis and reporting are completed, the data files are transferred to Sandia's Integrated File Storage System.

2.2 Sample Preparation

The rock tested was densely welded Topopah Spring tuff collected from an outcrop at Busted Butte, near Yucca Mountain on the NTS.

2.2.1 Shear Compliance Samples

Tuff samples began as short, hollow cylinders 44.45 mm long. Inner diameters were 50.8 ± 0.13 mm and outer diameters were 88.9 ± 0.25 mm. Some of the samples were later remachined to lengths of 16.9 mm with inner diameters increased to 69.8 mm. This was done to study samples with a smaller wall-thickness-to-radius ratio. Samples that were used for basic friction studies were first glued to end pieces, either aluminum or steel, that could be bolted into the machine. Before mounting, the sample-endplate assembly was placed in a surface grinder and the surface of the sample was ground flat and parallel to the surface of the endplate. This procedure ensured that the joint would be perpendicular to the axis of rotation when mounted in the machine.

Samples to be studied for rough joint response were selected from precracked pieces described in the next section. These were already cemented to endplates as discussed below and were mounted in the rotary shear machine as they were after normal stiffness testing.

2.2.2 Normal Stiffness Samples

The original samples for normal stiffness testing were hollow cylinders 133.35 mm long with an 88.9 ± 0.25-mm outside diameter and a 50.8 ± 0.13-mm inside diameter. The ends were parallel to within 0.1 mm. Machined into the outside surface was a circumferential groove lying in a plane perpendicular to the cylinder axis. The groove was originally 1.6 mm wide and 3.175 mm deep with an approximately flat bottom. The groove dimensions and shape evolved through testing to the currently used depth of 6.35 mm with a V-shaped bottom having a radius of curvature of 0.127 mm. This change in depth and shape came about through attempts to create a fracture contained entirely within the machined groove. Metal endplates identical to those noted above were glued to the ends of the rock cylinder. Next, the endplate/rock/endplate assembly was mounted in the rotary shear machine and pulled in tension. After creating a fracture within the groove, the sample was ready for normal stiffness testing.

2.3 Test Procedures

2.3.1 Shear Compliance and Friction Stress

The relationship between friction stress and normal stress on the fracture was found by applying a known, constant, uniform normal stress to the fracture and then increasing

the shear stress until sliding was established. In practice, the twist was increased until steady sliding conditions were achieved as evidenced by an essentially constant torque. Then, the torque was reduced to zero, and subsequently the normal stress was reduced to zero. Next, the sample was repositioned before the normal stress was increased to some new value and sliding was again established. This procedure was repeated several times.

2.3.2 Normal Stiffness

After introducing a tensile fracture in the rotary shear machine, the sample was removed to a standard compression frame where a hemispherical loading seat allowed the fracture surface to be in approximately uniform contact initially. Following the stress-closure test in a standard load frame, the sample was returned to the rotary shear machine where the shear response of this rough surface was measured.

The sample had strain gauges mounted on the inside and outside cylindrical surfaces at the ends of two orthogonal diameters. In addition, a linear variable displacement transducer (LVDT) measured total displacement from endcap to endcap. The sample was loaded in compression several times, both with the opposing fracture surfaces mated and unmated. Strains, displacement, and load were recorded continuously throughout the test.

3 DATA REDUCTION

3.1 Friction Stress

The friction stress, τ_f, is the shear stress, resolved into the plane of the fracture, that is needed for slip. There are two ways to calculate this value from the torque. The first uses the torque at the onset of slip. In the preslip, elastic range, the relationship between the tangential shear stress and the applied torque in the joint plane is found from elasticity theory [e.g., *Timoshenko and Goodier*, 1970]. If the torque at first slip is denoted T_0, the maximum shear stress denoted τ_o, and the radial coordinate denoted R_o, then

$$\tau_o = \frac{R_o T_0}{J} , \tag{10}$$

where $J = (\frac{\pi}{2})(R_o^4 - R_i^4)$ is the polar moment for an annulus of inner and outer radii R_i and R_o, respectively. The maximum elastic shear stress is also the friction stress, $\tau_o = \tau_f$, at the outer edge of the fracture.

After establishing steady sliding, that is, when the torque is nominally independent from the rotation, the torque-stress relation has the same form as for a fully yielded plastic tube [*Smith and Sidebottom*, 1969]; that is, the friction stress, τ_f, is found from

$$\tau_f = \frac{3T_{fs}}{2\pi(R_o^3 - R_i^3)} , \tag{11}$$

where the subscript *fs* denotes "fully sliding." The underlying assumption in deriving Equation 11 is that a material element has a flat-topped stress-displacement diagram in direct shear, analogous to the perfect elastic-plastic assumption in the torsion of elastic-plastic tubes.

For an ideal, uniform frictional resistance, the values of τ_f calculated from T_o and T_{fs} are identical. Further, the ratio of the fully sliding torque, T_{fs}, to the torque at the onset of sliding, T_o, is found to be

$$\frac{T_{fs}}{T_o} = \frac{4}{3}\left(\frac{1-\lambda^3}{1-\lambda^4}\right) , \tag{12}$$

where $\lambda = R_i/R_o$ and $0 \leq \lambda < 1$. Thus, for a solid cylinder, $\lambda = 0$ and $T_{fs}/T_o = 4/3$; for an increasingly thinner wall, $\lambda \to 1$ and $T_{fs} \to T_o$. Equation 12 is useful for estimating the variation in friction stress over a given test surface. This is because T_{fs} is a measure of the average friction stress over the entire test surface and is relatively insensitive to localized extrema. On the other hand, T_o is a function of the friction stress over a very thin annulus and, therefore, is more strongly influenced by localized fluctuations in the friction stress. Thus, departure of T_o from its value calculated from T_{fs} is a measure of the minimum friction stress occurring in the outermost annulus of the test surface. Therefore, the difference $T_{fs} - T_o$ is a measure of the range in friction stress on the test surface. This type of measure was also noted for plane strain joint deformation [*Olsson*, 1984].

T_o is a measure of the shear stress at the onset of sliding rather than the steady-state sliding value computed from T_{fs}. It should be noted that the coefficient of friction, μ, calculated from T_{fs} corresponds to the conventional value.

3.2 Compliances

It is important to isolate that part of the measured response that is due to the presence of the joint. There are several methods suitable for measuring the compliance of a joint:

1. Subtract the intact rock compliance from the total compliance to obtain C_{tt}^{p}. If it can be verified that the joint contributes negligible elastic contribution to the total deformation (*i.e.*, $C_{tt}^{e} = 0$), then it can be assumed that the compliance of the elastic unloading line on a plot of torque *versus* twist angle is the sum of the machine compliance and the intact rock compliance.

2. Measure the compliance of a sample of intact rock. Introduce a fracture into this sample and repeat the compliance measurement. Subtract the displacements found in the two tests; the result is displacement as a result of the compliance of the joint. This method automatically removes any contribution to displacement of intact rock and machine compliances.

3. Measure the total displacement of a specimen already containing a fracture over a gauge length that includes the joint. Also, measure the strain of the intact part of the sample. Then, compute the elastic contribution to the overall displacement using strain×gauge-length. Subtract the elastic component to get the component resulting from the joint alone.

4. Measure displacement across the joint as in Method 3, but use the modulus determined in separate experiments to compute intact rock deformation [*Rosso*, 1976]. This is a less accurate version of Method 3.

The compliance data reported below were obtained by the first method after verifying, by measuring slip directly, that the slip was plastic. This was demonstrated by *Olsson* [1987b]. The compliance of the rough joint was also determined by the inverse of Method 2; that is, after the tensile fracture was formed, the shear test was done (Figures 12 and 13). Then, the fracture was cleaned and pressed together with the opposite sides fitted together. When twisted such that response remained in the preslip, linear range (Figure 14), the combined compliance of the rock cylinder plus the machine was obtained. This method, though not recommended, gave results identical to Method 1.

4 DISCUSSION OF RESULTS

Table 1 lists all experiments along with the sample number and the principal objective of each test. The figures are organized to show shear compliance, C_{tt}^{p}, in Figures 1–20; a slip condition in Figure 21; normal compliance, C_{nn}, in Figures 22–25; the effects of large displacement, hereinafter referred to as "run-in" in Figures 26–32; the effects of normal stress and normal stress history in Figures 33–81; and the effects of slip velocity in Figures 82–89. Table 1 also notes whether the experiment was discussed in the previous report [*Olsson*, 1987b].

4.1 Shear Compliance, C_{tt}^p

Figures 1–21 show experiments that were run to measure C_{tt}^p. Each figure contains four plots: torque against angle showing the total test; for the loading phase only, shear stress against slip; compliance, C_{tt}^p, against shear stress; and a plot of the logarithm of shear stress against the logarithm of slip.

The onset of nonlinearity of the torque–angle relation on loading marks the beginning of slip. This has been shown to be, for practical purposes, identical to the establishment of fully slipping conditions [*Olsson*, 1987b]. Thus, Equation 11 was used to compute shear stress from torque. The slope of the linear portion of the first unloading line was used to compute the combined deformation of the machine and intact rock. This was subtracted from the measured angular displacement. Then, the circumference of the sample was used to calculate the maximum slip (referred to below as the slip) from the angle of rotation.

4.2 Slip Condition

For the current data set, the slip condition is adequately characterized by $\tau = \mu\sigma$. For some circumstances, μ shows some weak dependence on σ. Figure 21 shows the values of friction stress computed from Equations 10 and 11 for Sample 16C-CC/16B-BB tested in several different runs. The triangles represent the onset of slip and the circles represent the maximum observed friction. The solid line is a linear regression to the maximum friction values that gives $\mu = 0.609$, representative of the ordinarily stated coefficient. The other two lines were drawn by eye and indicate the upper and lower bounds of the friction coefficient, possibly more usable numbers.

4.3 Normal Compliance, C_{nn}

Figures 22–24 show the results of normal compliance tests on a mated laboratory-induced tensile fracture in Sample 16D. Data for the same fracture in the unmated condition is shown in Figure 25. A much more compliant response was observed for the unmated fracture.

4.4 Run-in

Run-in refers to the process of sliding the test surface until the stress becomes approximately constant. This usually took the form of successive torque-slip loops, with the accumulating gouge cleaned off the surfaces between loops. Typically, the friction increases with increasing total slip up to some definite value. Figures 26 and 27 show run-in data for a sample that had been ground only, not sandblasted. After about 16 mm of slip, friction achieves a steady value.

For a different sample, Figures 28–30 show that friction does not reach a steady value at all. Figure 31, for a sample that was ground before rather than after mounting to the endplates, shows the response for a surface that is probably not in uniform contact. In contrast, Figure 32 shows the response of a sample that was ground after mounting, which was the usual routine, and then lightly sandblasted to remove the sheen from the surface.

4.5 Normal Stress History

It is general knowledge that the friction stress is a strong function of the normal stress. However, it has recently been shown that friction stress is a functional of normal stress; that is, the friction stress can depend on the history of the normal stress. One difference between history independence and history dependence can be seen by considering the result of running a standard friction experiment with initially constant σ. After establishing steady sliding conditions with constant friction stress, σ is suddenly incremented. If τ_f remains exactly proportional to σ then, τ is a direct function of σ and does not depend on the history of σ. If, however, there is a transient change in τ_f, with a gradual approach to some new value, then τ_f depends on the history of σ.

The coefficient of friction, μ, is a sensitive indicator of the normal stress history effect and, therefore, all plots (Figures 33–81) of experiments on this effect are given as μ *versus* slip.

4.6 Slip Velocity

Figures 82–89 show the effects of changes in slip velocity. The data were analyzed and discussed by *Olsson* [1987b].

5 CONCLUSIONS

The analysis of the data indicates several conclusions that were stated by *Olsson* [1987b] and are reiterated here with some additions:

1. The coefficient of friction can vary from an initial value of about 0.3 to a steady-state value of about 0.8. This range can be found on an individual clean, smooth surface and appears to be related to initial conditions of surface preparation.

2. The elastic, preslip, shear stiffness of smooth and rough joints was found to be infinite when measured and calculated correctly.

3. All displacement attributable to slippage on the joint is plastic, that is, nonrecoverable.

4. The shear compliance varies smoothly from zero at the onset of slip to infinity when sliding is established. There is an approximately linear relation between log τ_f and log δ_t.

5. The normal joint stiffness is consistent with results in the literature in that it is a continuously increasing function of normal stress. The normal closure displacement is composed of elastic (recoverable), plastic (non-recoverable), and frictional (recoverable but hysteretic) components.

6. Shear strength decreases by about 5% for each decade increase in slip velocity.

7. The effect of a sudden change in slip velocity can be interpreted in terms of hereditary integral or internal state variable descriptions.

8. There may exist a critical velocity. Below the critical velocity, a sudden increase in velocity causes an instantaneous increase in strength, which then decays gradually to a new, lower value. Above the critical velocity, there is no instantaneous increase in strength following a jump in velocity—just a smooth decrease.

9. The strength of the joint may increase with time of stationary contact.

10. Transient behavior in μ is observed after sudden changes in σ; that is, the coefficient of friction depends on the history of normal stress.

11. The stress-path to the slip condition has a measurable effect on the observed strength, thus indicating caution in the application of data from triaxial tests run at constant confining pressure.

12. True slip-weakening for initially smooth surfaces may have been found in Topopah Spring tuff. This response is usually masked by inhomogeneous resistive stresses.

13. For the low normal stresses used in this study, the torque-twist curve appears to be a direct measure of the shear compliance of a joint; that is, there is no significant contribution from the radial growth of the slip zone. Thus, the rotary shear results should be directly comparable to those from other tests, such as direct shear and triaxial, insofar as these data are collected from similar stress and velocity histories.

6 REFERENCES

Chen, E. P., Two-dimensional continuum model for jointed media with orthogonal sets of joints, in 27^{th} U.S. Symp. on Rock Mech., *Rock Mechanics: Key to Energy Production*, Univ. of Alabama, pp. 862-867, 1986.

Goodman, R. E., and J. Dubois, Duplication of dilatancy in analysis of jointed rocks, *J. Soil Mech. and Found. Div.*, Am. Soc. Civil Engrs., Vol. 4, pp. 399–422, 1972.

Holcomb, D. J., and A. K. Jones, Data acquisition for the rock mechanics lab, *SAND83–0646*, Sandia National Laboratories, Albuquerque, NM, August 1983.

Olsson, W. A., A dislocation model of the stress history dependence of frictional slip, *J. Geophys. Res.*, Vol. 89, pp. 9271–9280, October 1984.

Olsson, W. A., The effects of changes in normal stress on rock friction, in *Constitutive Laws for Engineering Materials, Theory and Applications*, C. S. Desai, E. Krempl, P. D. Kiousis, and T. Kundu, eds. Elsevier, NY, pp. 1059–1066, 1987a.

Olsson, W. A., Rock joint compliance studies, *SAND86–0177*, Sandia National Laboratories, Albuquerque, NM, April 1987b.

Olsson, W. A., The effects of normal stress history on rock friction, in 29^{th} U.S. Symp. on Rock Mechanics, *Key Questions in Rock Mechanics*, A.A. Balkema, Rotterdam, 1988.

Plesha, M. E., Constitutive modeling of rock joints with dilation, in 26^{th} *U. S. Symp. on Rock Mechanics*, E. Ashworth, ed., Balkema, Boston, MA, 1985.

Rice, J. R., On the stability of dilatant hardening for saturated rock masses, *J. Geophys. Res.*, Vol. 80, pp. 1531–1536, April 1975.

Rosso, S., Comparison of joint stiffness measurements in direct shear, triaxial compression, and *in situ*, *Int. J. Rock Mech. Min Sci. & Geomech. Abstr.*, Vol., 13, pp. 167–172, 1976.

Rudnicki, J. W., and J. R. Rice, Conditions for the localization of deformation in pressure-sensitive dilatant materials, *J. Mech. Phys. Solids*, Vol., 23, pp. 371–394, 1975.

Smith, J. O., and O. M. Sidebottom, *Elementary Mechanics of Deformable Bodies*, Chap. 9, Macmillan, Toronto, Canada, 1969.

Sun, Z., C. Gerrard, and O. Stephansson, Rock joint compliance tests for compression and shear loads, *Int. J. Rock Mech. Min. Sci. & Geomech. Abstr.*, Vol. 22, pp. 197–213, 1985.

Timoshenko, S. P., and J. N. Goodier, *Theory of Elasticity*, Art. 101, Third Edition, McGraw-Hill, New York, NY, 1970.

Thomas, R. K., A continuum description for jointed media, *SAND81-2615*, Sandia National Laboratories, Albuquerque, NM, April 1982.

Table 1. Experimental conditions.

TEST ID	SAMPLE ID	TEST TYPE	NOMINAL σ (MPA)	SAND86-0177	COMMENTS
RFT001	16B-AA/16B-CC	COMPLIANCE, C_{tt}	5	-	GROUND, SANDBLASTED
RFT002	15C-CC/16C-CC	"	5	-	GROUND, SANDBLASTED
RFT003	"	"	5	-	
RFT004	16B-BB/16C-CC	"	5	-	GROUND, SANDBLASTED
RFT005	"	"	5	-	
RFT006	"	"	5	-	BAD DISPLACEMENT DATA
RFT007	"	"	5	-	
RFT008	"	"	2	-	
RFT009	"	"	4	-	
RFT010	"	"	6	-	
RFT011	"	"	4	-	
RFT012	"	"	2	-	
NST005	16D	COMPLIANCE, C_{nn}	0–5	-	MATED TENSILE FRACTURE
NST006	"	"	0–3	-	"
NST007	"	"	0–9	√	"
NST008	"	"	0–6	√	UNMATED TENSILE FRACTURE
RFT013	"	COMPLIANCE, C_{tt}	2	√	"
RFT014	"	"	2	-	"
RFT015	"	"	2	-	DATA LOST
RFT016	"	"	2	-	MATED TENSILE FRACTURE
RFT017	16B-BB/16C-CC	"	2	-	GROUND, SANDBLASTED
RFT018	"	"	4	-	
RFT019	"	"	6	-	
RFT020	"	"	4	-	
RFT021	"	"	2	-	
RFT022	"	"	6	-	
RFT023	"	STRESS HISTORY	2,4,6,4,2	-	
RFT024	"	"	4,6	-	
RFT025	"	"	4,6,4	-	
RFT026	"	"	4,6	√	
RFT027	"	"	6,4,6	-	
RFT028	"	SLIDING VELOCITY	6	√	
RFT029	"	STRESS HISTORY	3,5,3,5	-	TORQUE CYCLED
RFT030	"	"	3	√	TORQUE CYCLED

Table 1. Experimental conditions (continued).

TEST ID	SAMPLE ID	TEST TYPE	NOMINAL σ (MPA)	SAND86-0177	COMMENTS
RFT031	16B-BB/16C-CC	STRESS HISTORY	3,4.5	-	TORQUE CYCLED
RFT032	"	"	DUAL RAMP	-	
RFT033	"	"	2.93,3.31	-	σ STEPPED
RFT034	"	COMPLIANCE, C_{tt}	3.8	-	
RFT035	"	STRESS HISTORY	3.2,4.8,3.6	-	
RFT036	"	"	3.1,3.5	-	σ STEPPED
RFT037	"	"	3.95,4.1	-	σ STEPPED
RFT038	"	SLIDING VELOCITY	5	-	
RFT039	"	STRESS HISTORY	5, 5.5	-	
RFT040	"	"	4,4.5	-	ALTERNATING σ STEPS
RFT041	"	"	DUAL RAMP	-	
RFT042	"	"	"	-	
RFT043	"	SLIDING VELOCITY	5	√	
RFT044	"	STRESS HISTORY	3.9, 4.7	-	σ STEPPED
RFT045	"	"	DUAL RAMP	-	
RFT046	"	"	"	√	
RFT047	"	"	"	√	
RFT048	"	"	"	-	
RFT049	"	"	"	-	
RFT050	"	"	"	-	
RFT051	"	"	"	-	16B-BB CRACKED
RFT052	16B-AA/16C-CC	"	"	-	GROUND
RFT053	"	"	"	-	
RFT054	"	SLIDING VELOCITY	5	-	UNSTEADY LOAD
RFT055	"	STRESS HISTORY	5, 5.5	-	σ STEPPED
RFT056	"	"	1,2,3,4,5,6	√	σ STEPPED
RFT057	"	"	5	-	σ STEPPED, UNSTABLE
RFT058	"	RUN-IN	5	√	
RFT059	"	"	2,4,6,4	√	
RFT060	"	STRESS HISTORY	1,2,3,2,1	-	σ STEPPED

Table 1. Experimental conditions (concluded).

TEST ID	SAMPLE ID	TEST TYPE	NOMINAL σ (MPA)	SAND86-0177	COMMENTS
RFT061	16B-AA/16C-CC	STRESS HISTORY	2,4,6,5,4,3,2,1	-	σ STEPPED
RFT062	"	"	2,3,4,5,6,5,4,3,2,1	√	σ STEPPED
RFT063	"	"	DUAL RAMP	√	
RFT064	"	"	3.4, 4	√	σ STEPPED
RFT065	"	"	3.4,4	√	σ STEPPED
RFT066	16C-AA/16C-AA1		1,2	-	16C-AA CUT INTO TWO, GROUND
RFT067	"	RUN-IN	4	-	
RFT068	"	"	4	-	
RFT069	"	"	2,4,5	-	ONE HALF BROKE
RFT070	16C-AA2/16B-AA	RUN-IN	4	-	NOT GROUND AFTER MOUNTING
RFT071	"	STRESS HISTORY	3.8	-	"
RFT072	16C-AA2/16C-CC	RUN-IN	4.5	-	GROUND, SANDBLASTED
RFT073	"	STRESS HISTORY	1,2,3,4,5,6,5,4,3,2,1	-	σ STEPPED
RFT074	"	"	1.5,2.6	-	σ STEPPED
RFT075	"	"	3.4, 4.5	-	"
RFT076	"	"	1.5, 2.5	-	"
RFT077	"	"	1.4, 2.4	√	"
RFT078	"	"	DUAL RAMP	√	"
RFT079	"	"	DUAL RAMP	√	"
RFT080	16C-AA/16C-CC	"	3.5, 4.5	-	σ STEPPED, GROUND , SANDBLASTED
RFT081	"	"	3.3	-	UNSTABLE LOAD
RFT082	"	"	3.3, 4.4	-	σ STEPPED, 16C-CC BROKE
RFT083	16C-AA/16C-AA	SLIDING VELOCITY	1.5	-	σ STEPPED
RFT084	"	"	5	-	
RFT085	"	"	5	-	UNSTABLE
RFT086	16C-AA/16C-BB	"	5	-	UNSTABLE
RFT087	"	"	5	-	DATA LOST
RFT088	"	"	?	-	DATA LOST

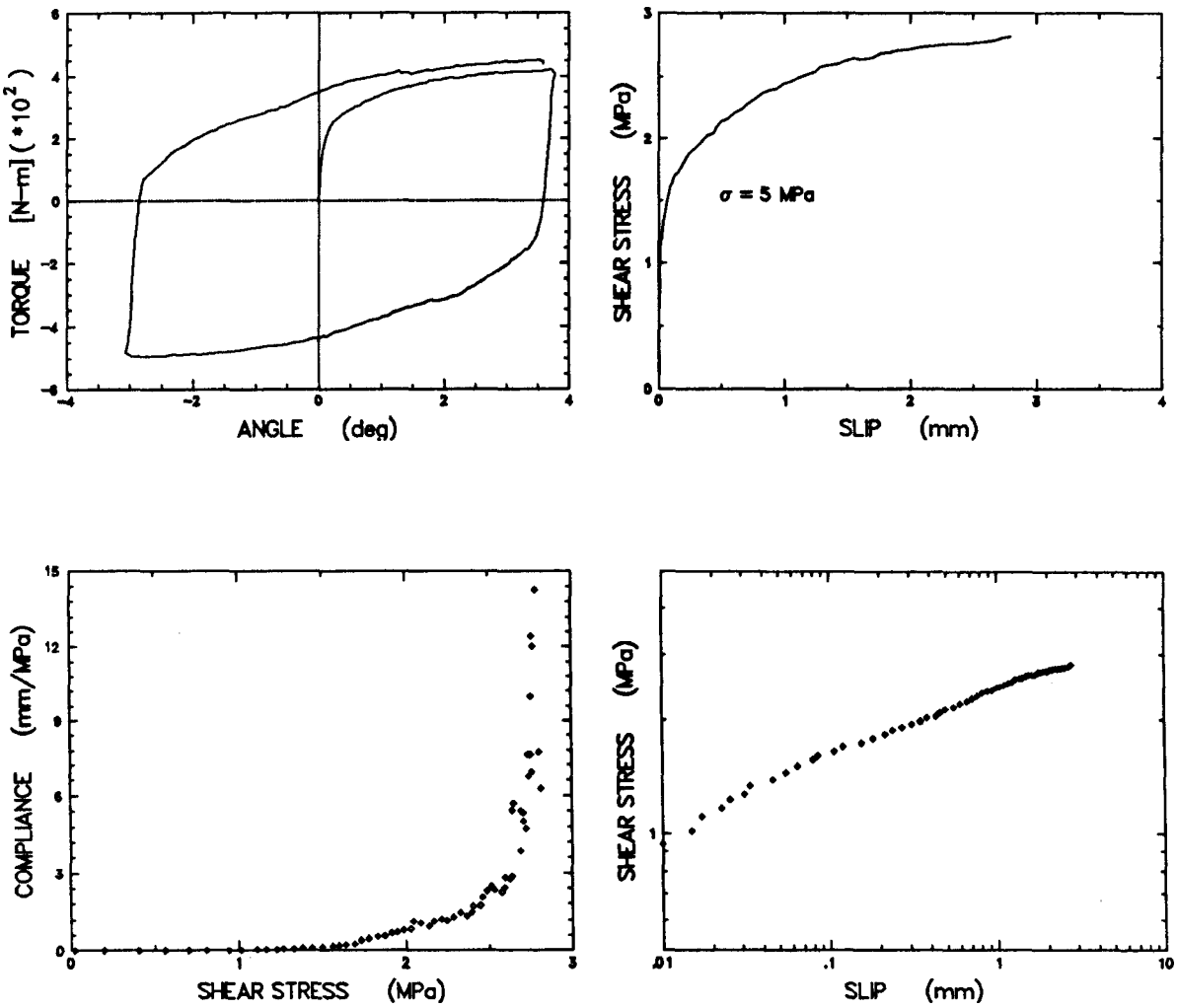

Figure 1: Experiment RFT001, shear compliance test.

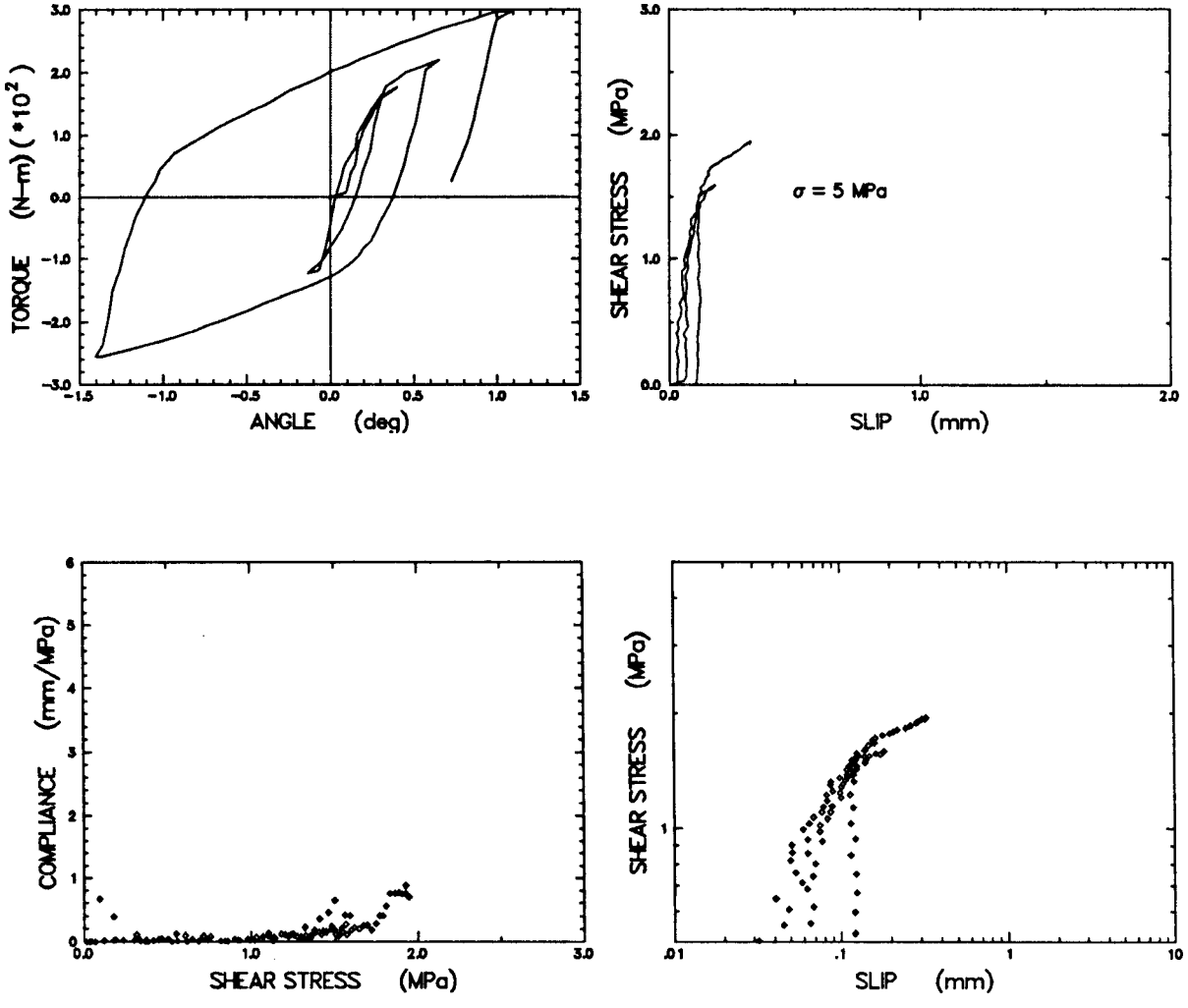

Figure 2: Experiment RFT002, shear compliance test.

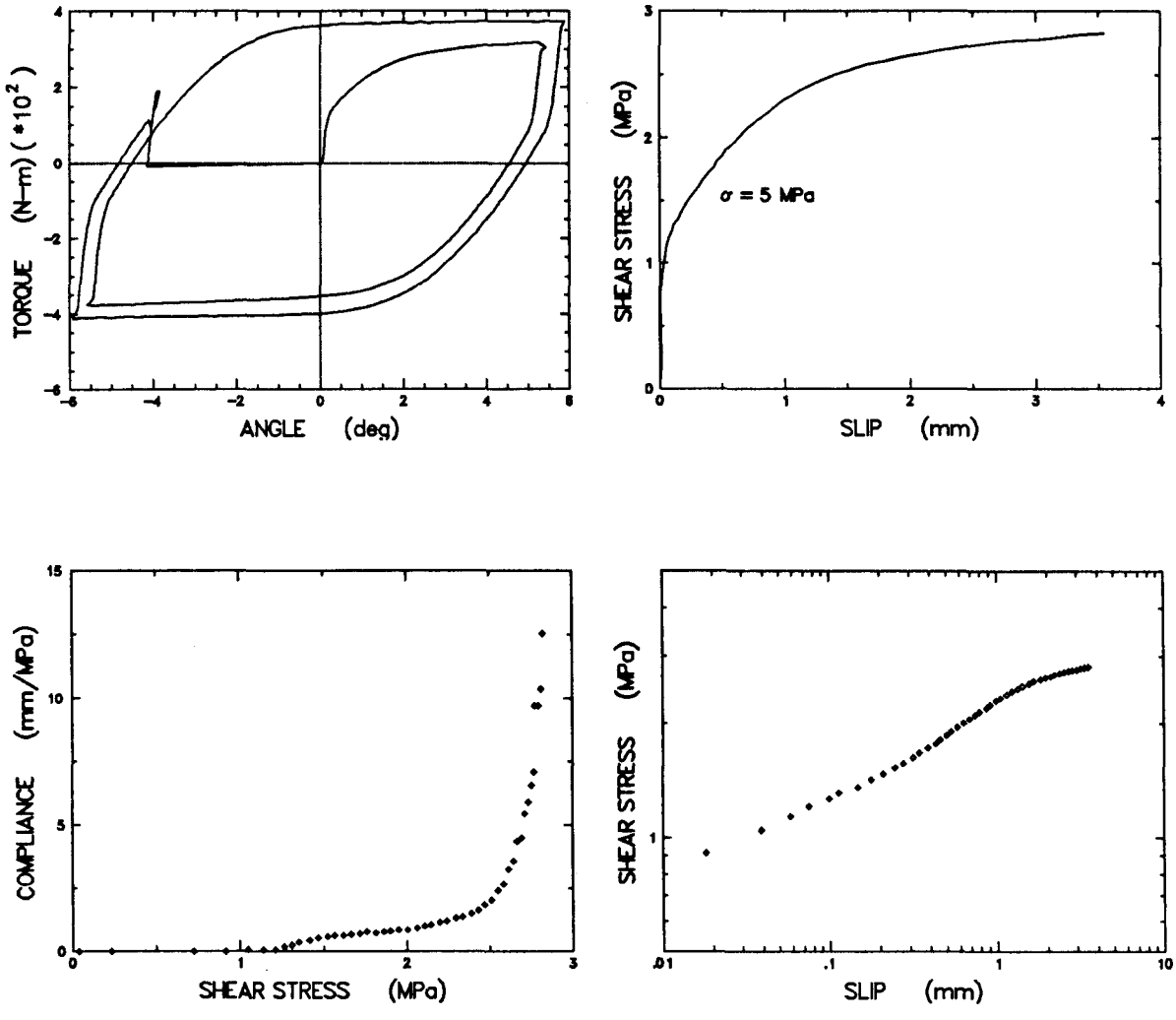

Figure 3: Experiment RFT003, shear compliance test.

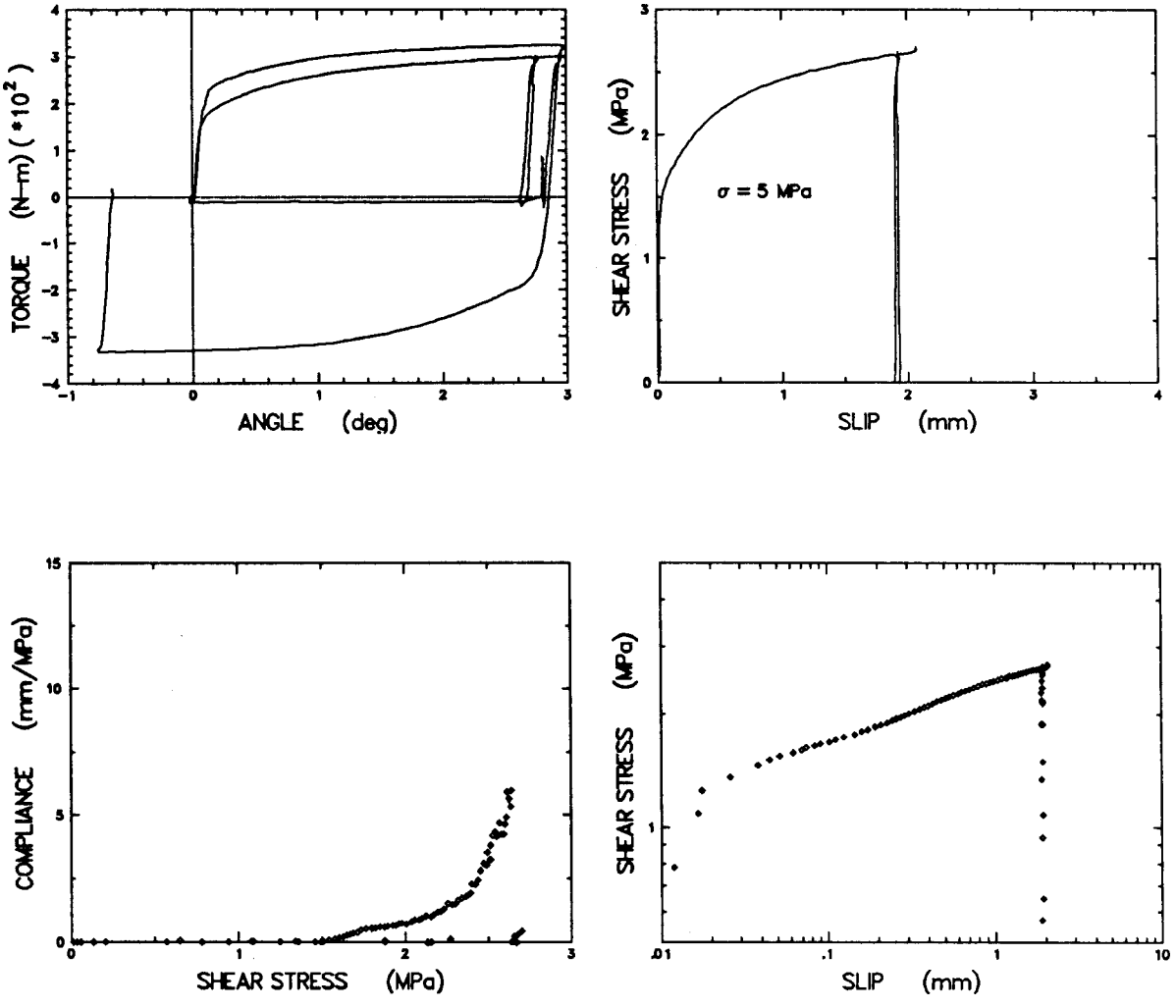

Figure 4: Experiment RFT004, shear compliance test.

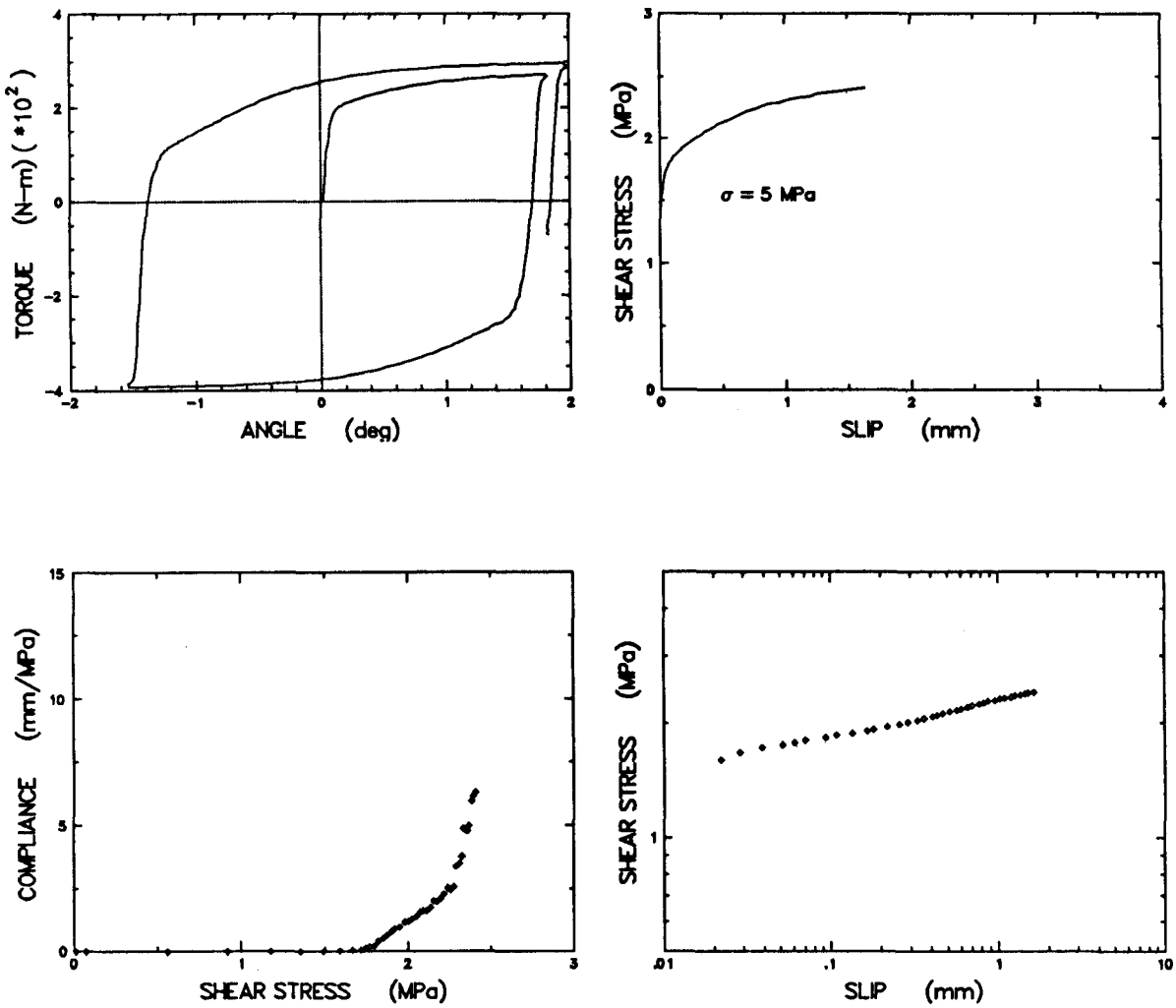

Figure 5: Experiment RFT005, shear compliance test.

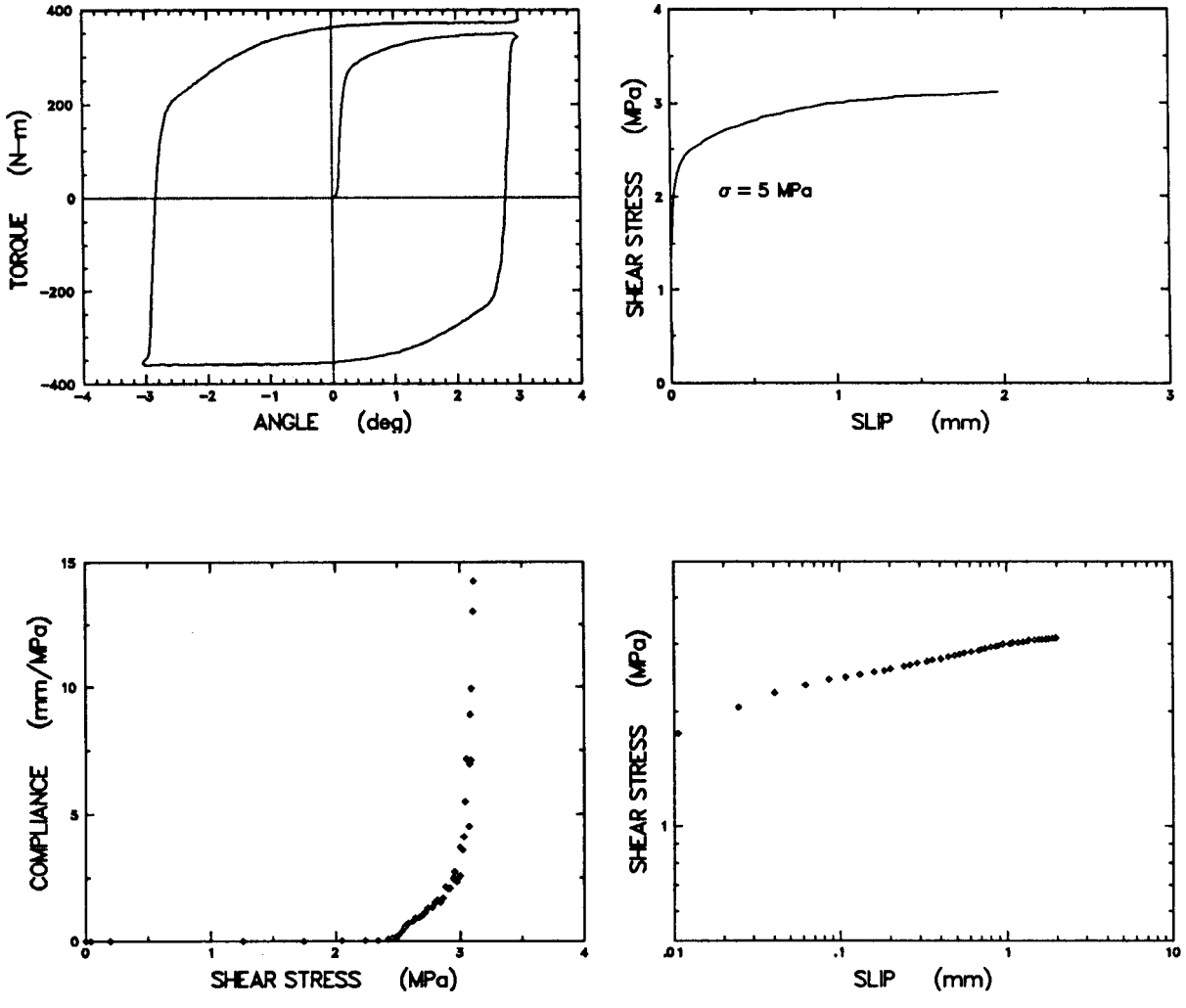

Figure 6: Experiment RFT007, shear compliance test.

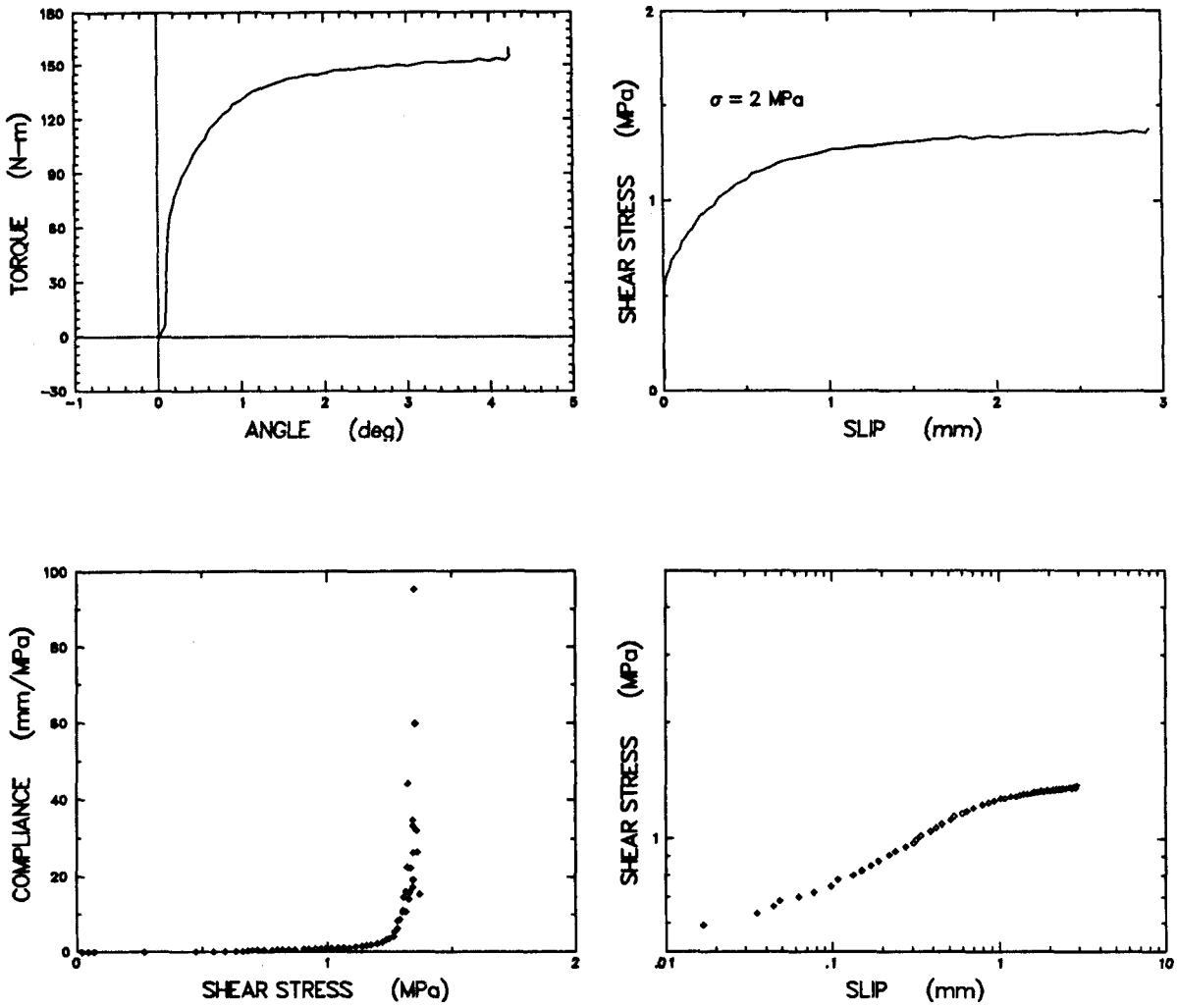

Figure 7: Experiment RFT008, shear compliance test.

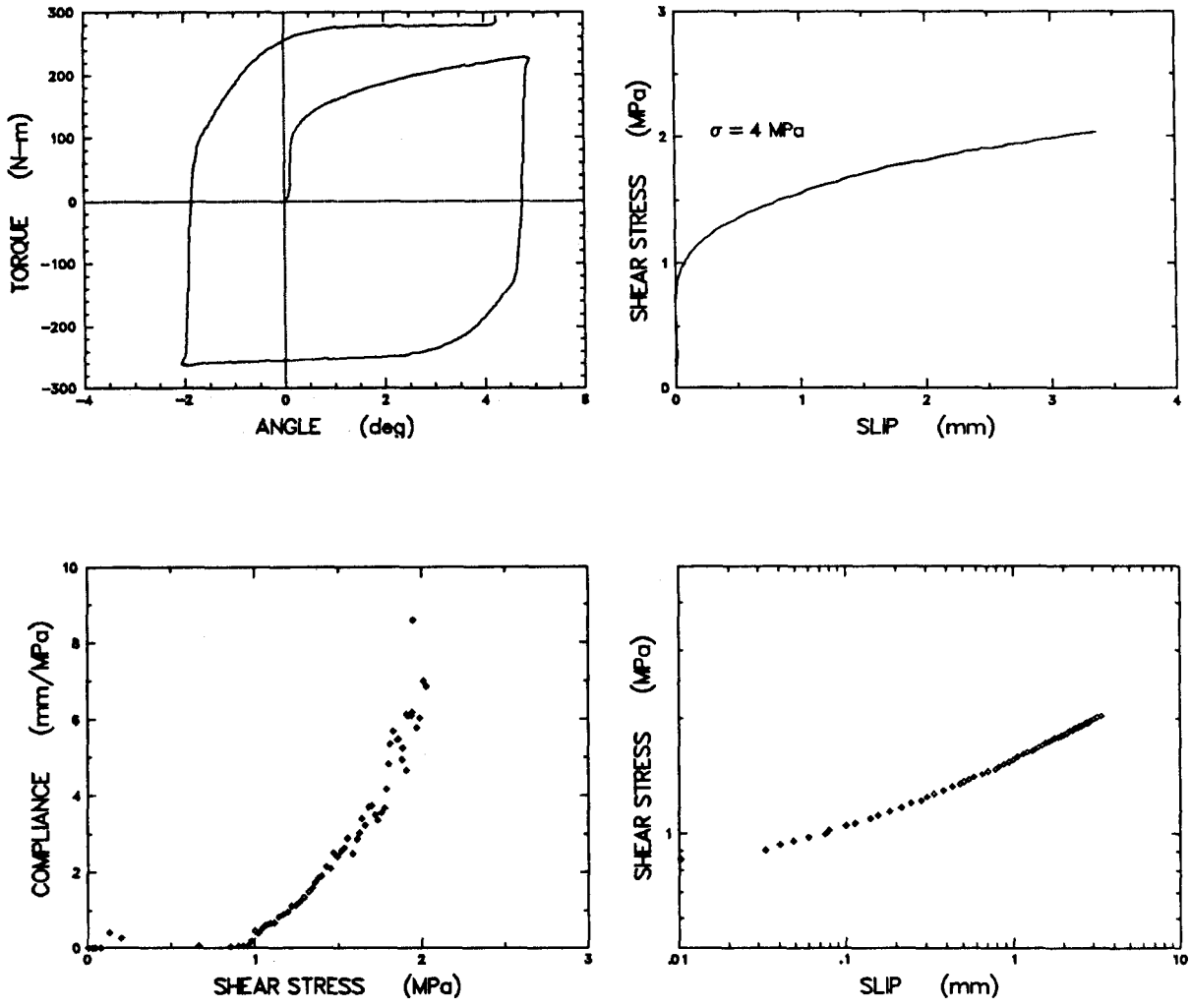

Figure 8: Experiment RFT009, shear compliance test.

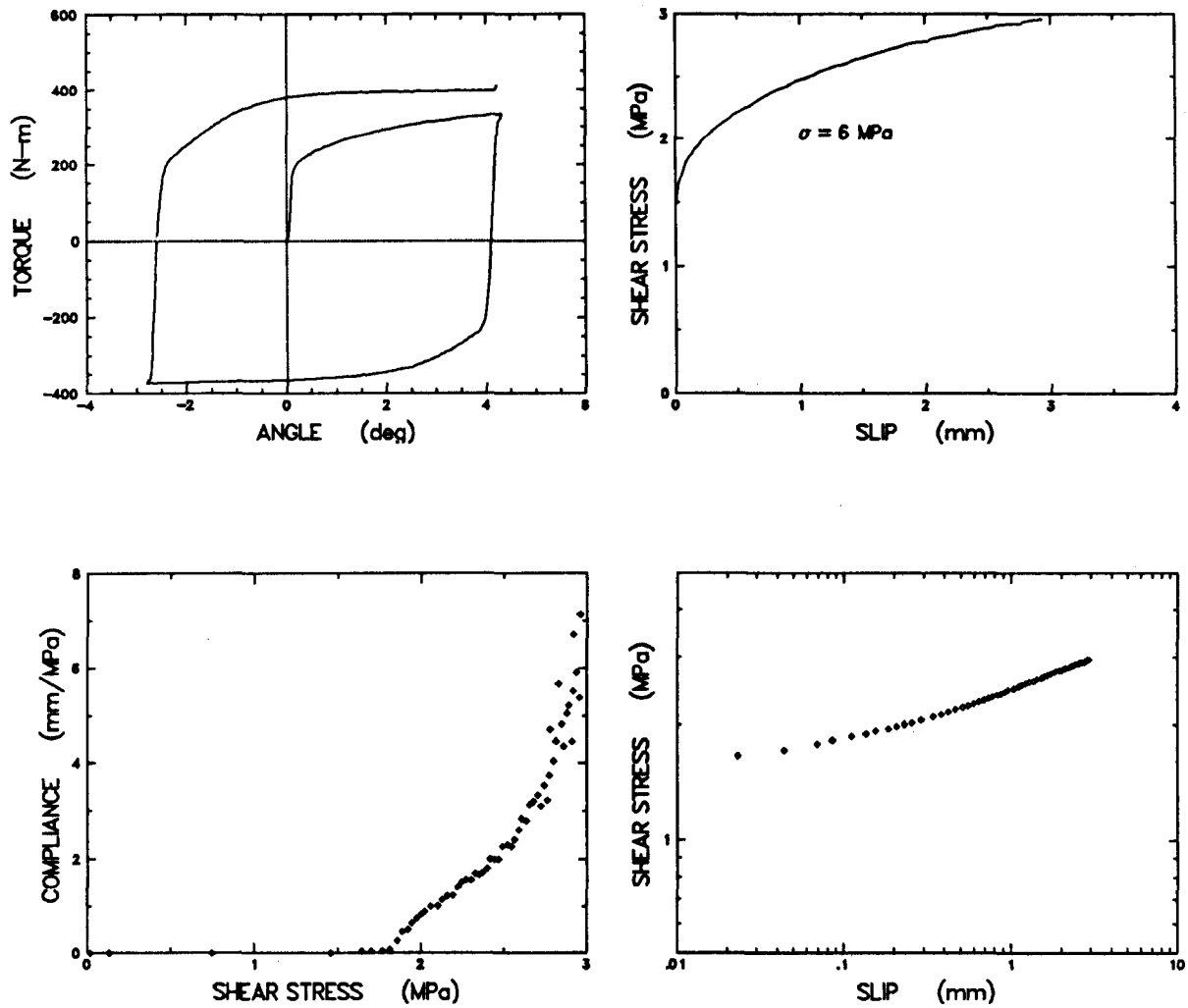

Figure 9: Experiment RFT010, shear compliance test.

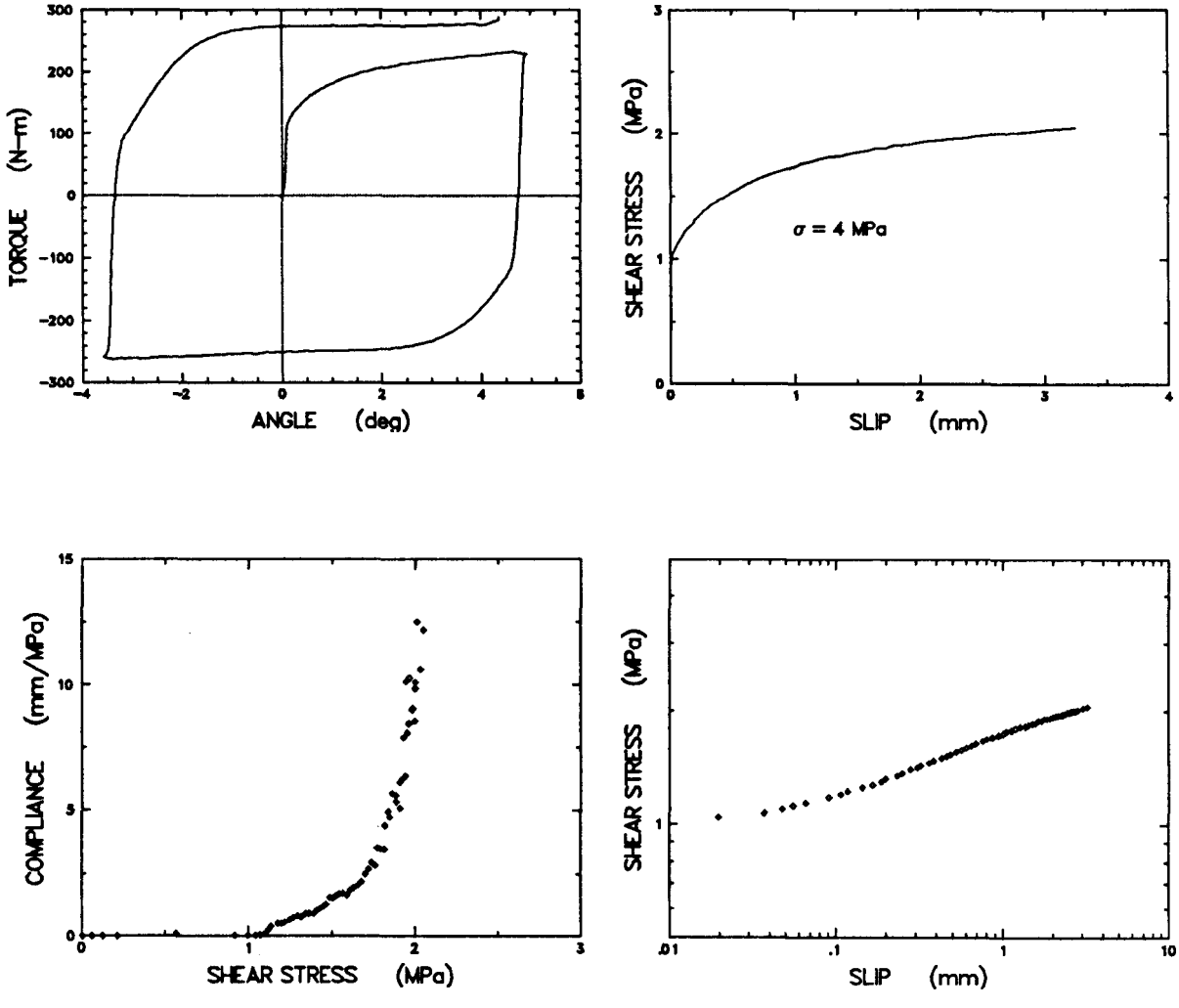

Figure 10: Experiment RFT011, shear compliance test.

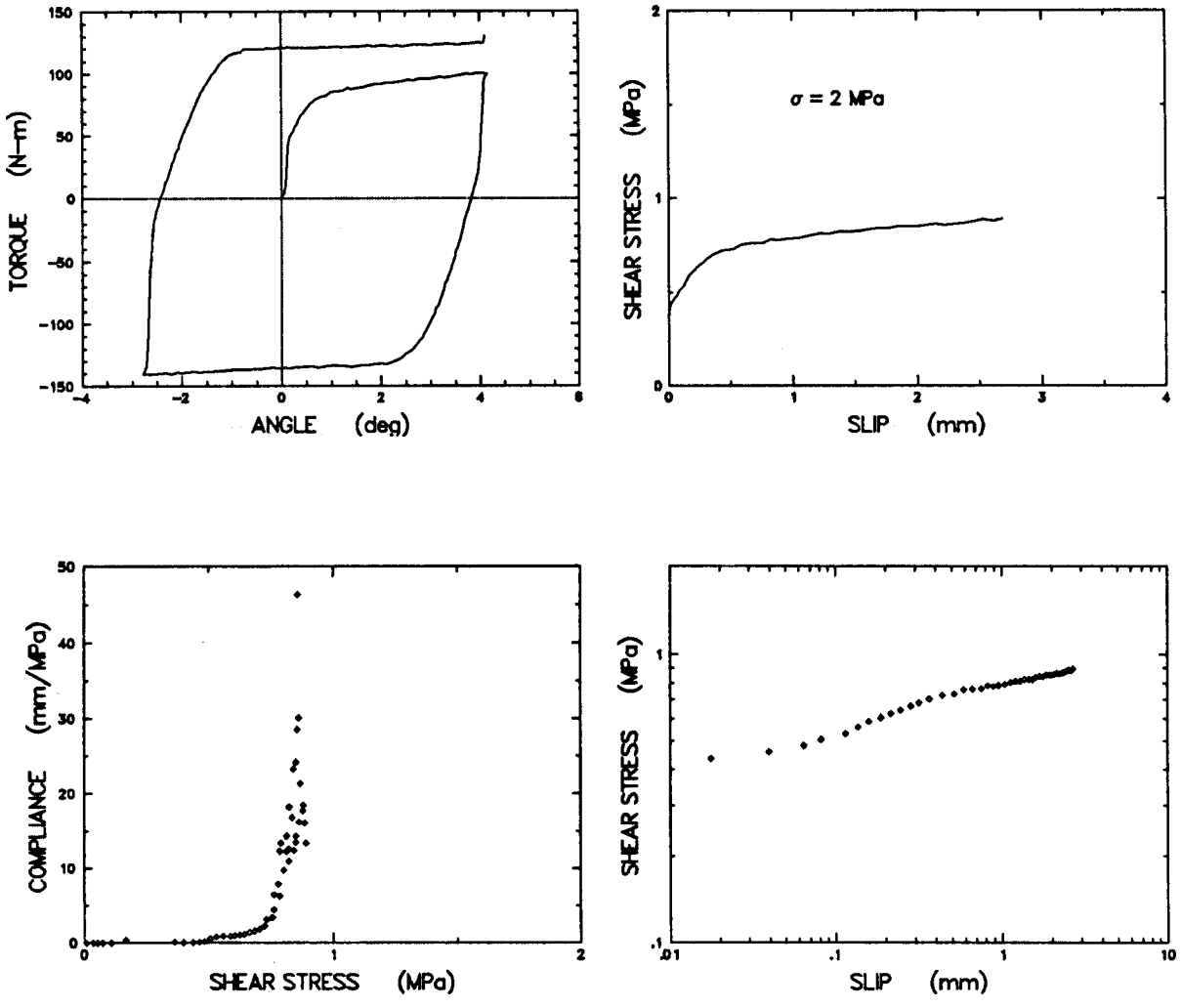

Figure 11: Experiment RFT012, shear compliance test.

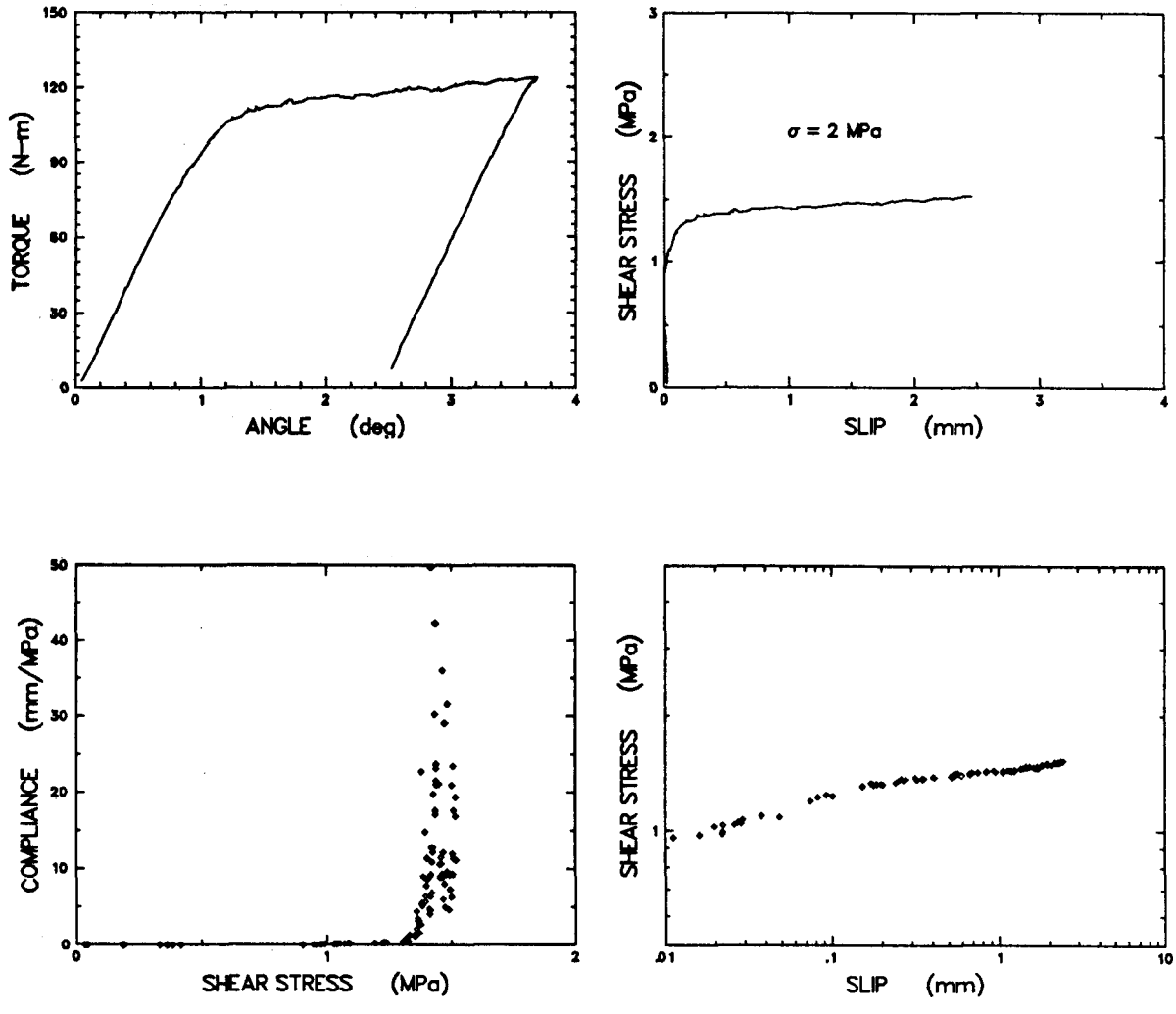

Figure 12: Experiment RFT013, shear compliance test.

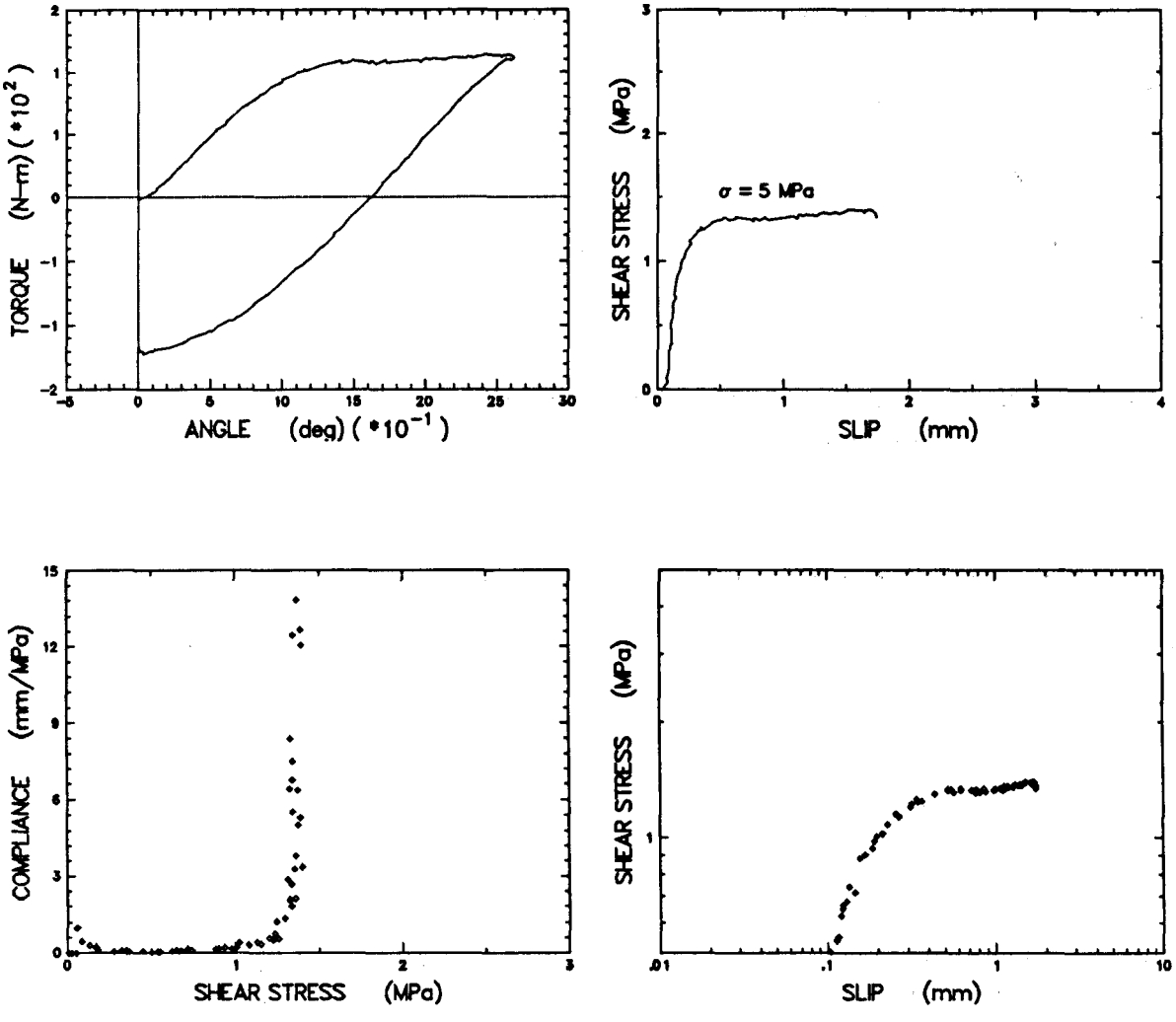

Figure 13: Experiment RFT014, shear compliance test.

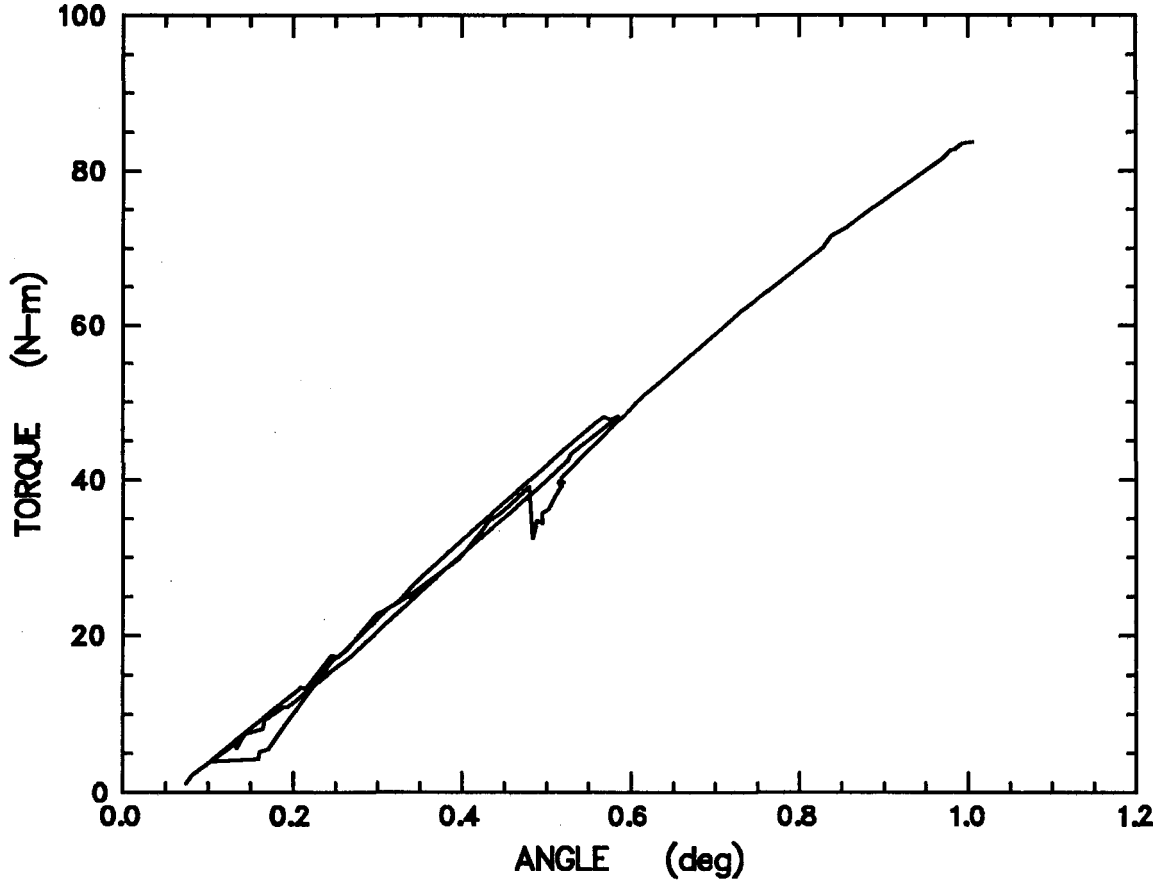

Figure 14: Experiment RFT016, rough surface, mated, shear compliance test.

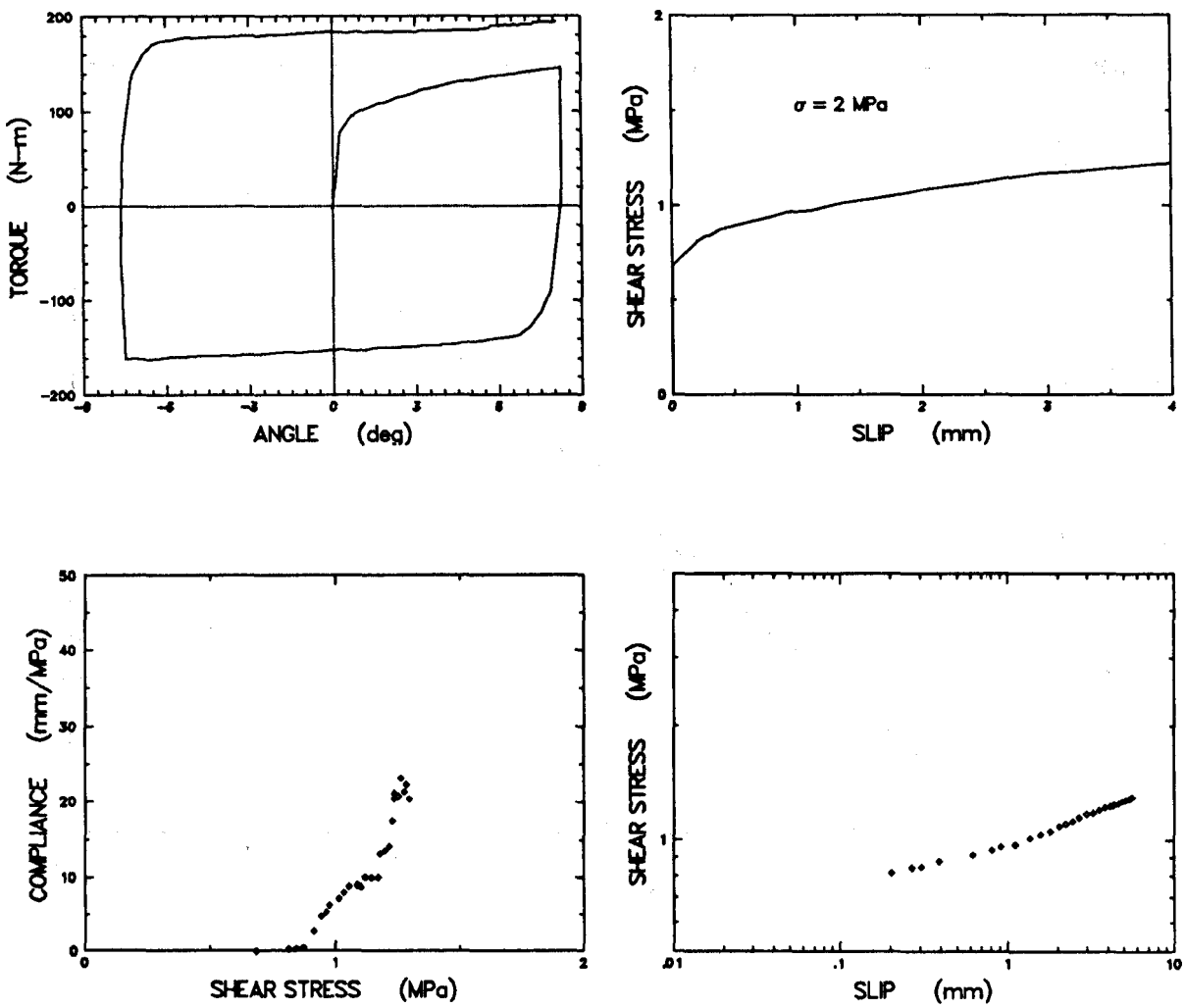

Figure 15: Experiment RFT017, shear compliance test.

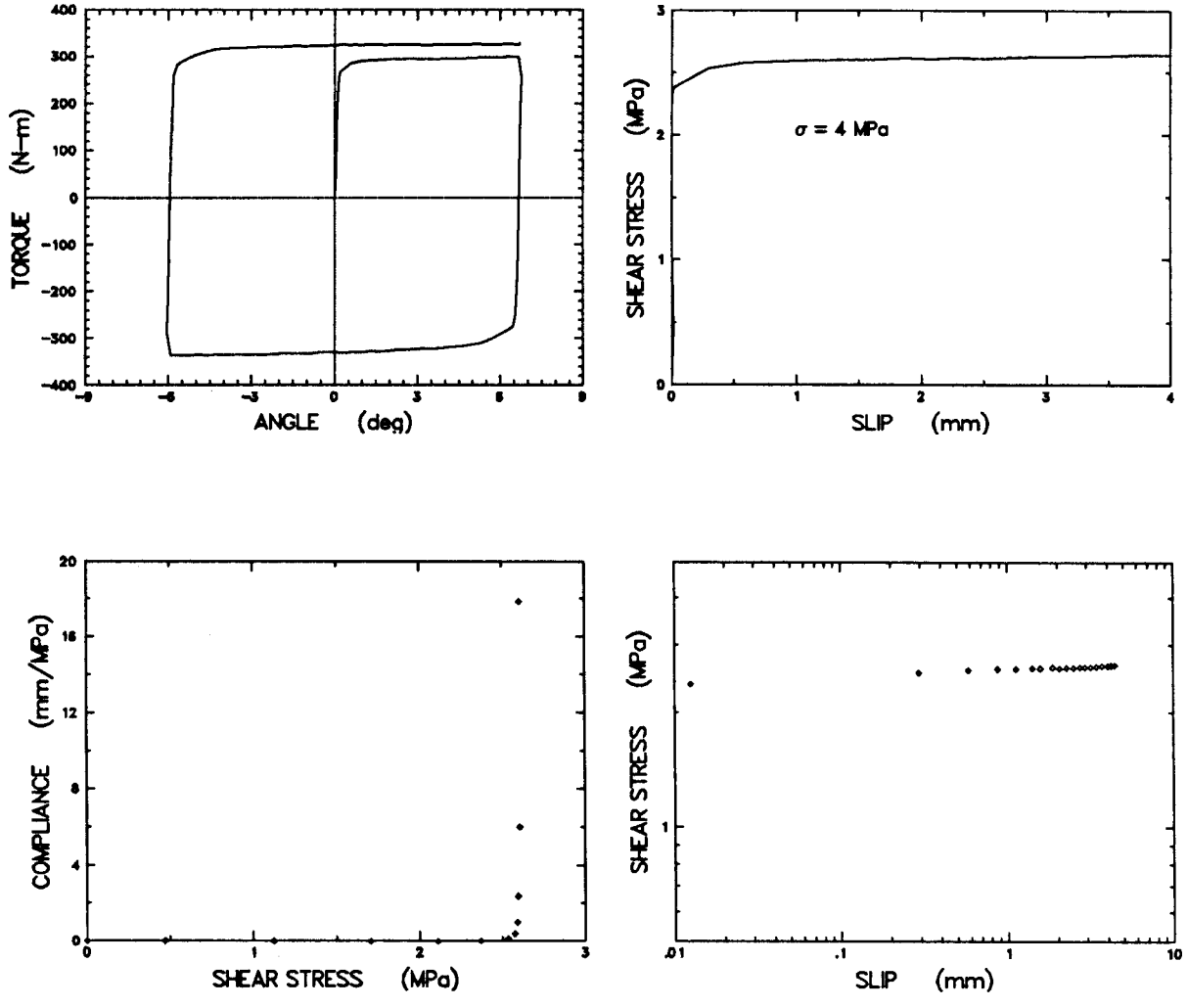

Figure 16: Experment RFT018, shear compliance test.

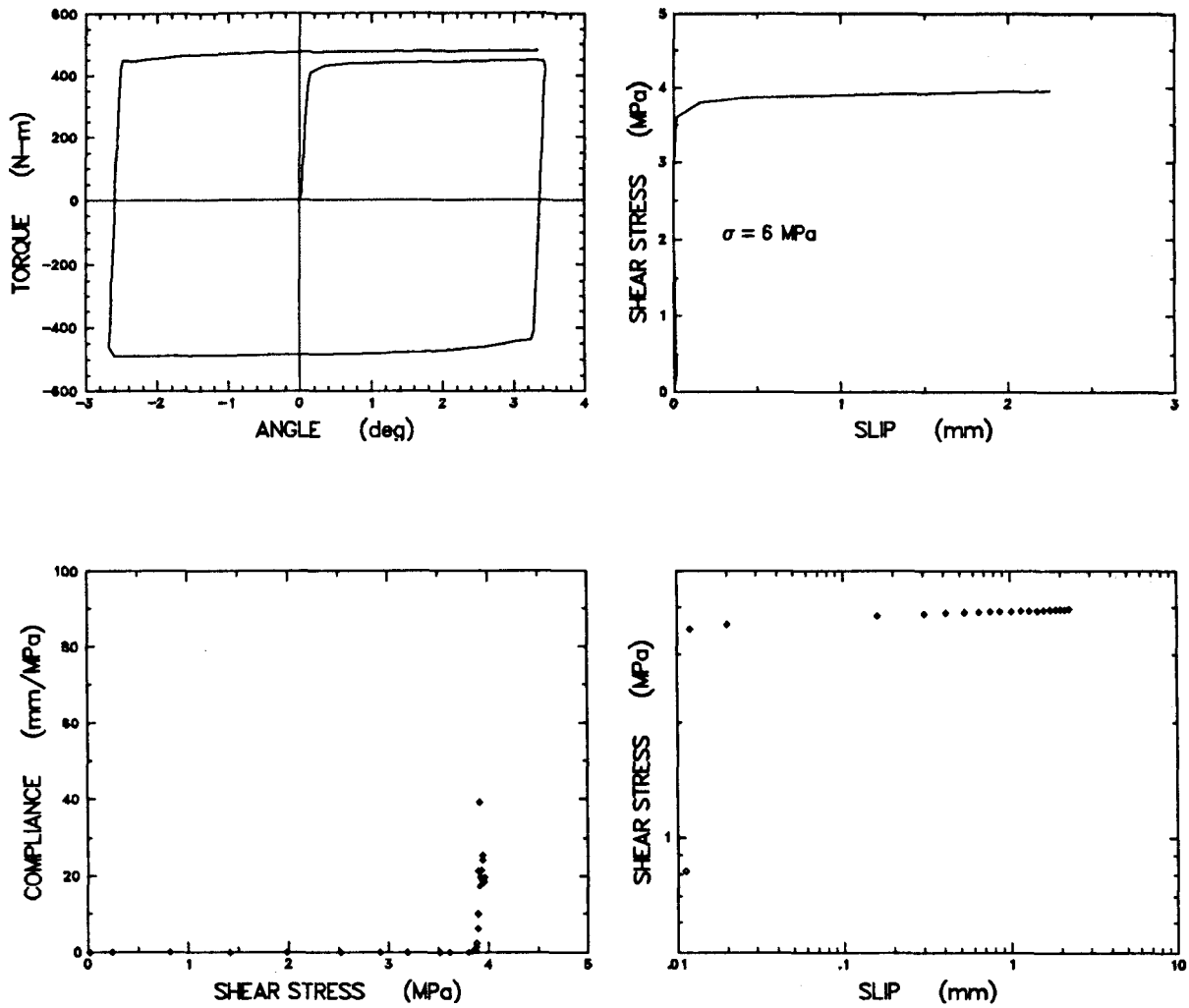

Figure 17: Experiment RFT019, shear compliance test.

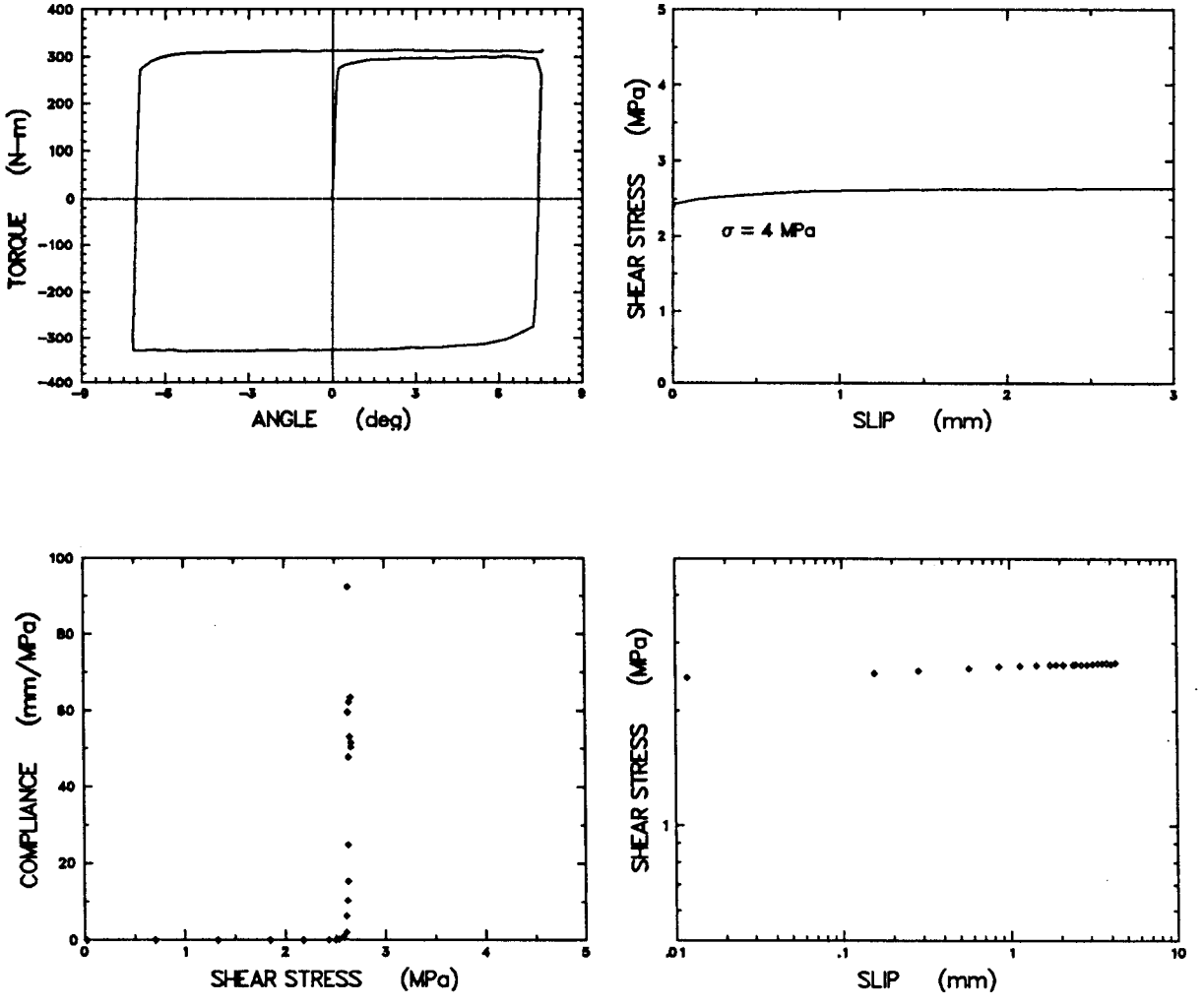

Figure 18: Experiment RFT020, shear compliance test.

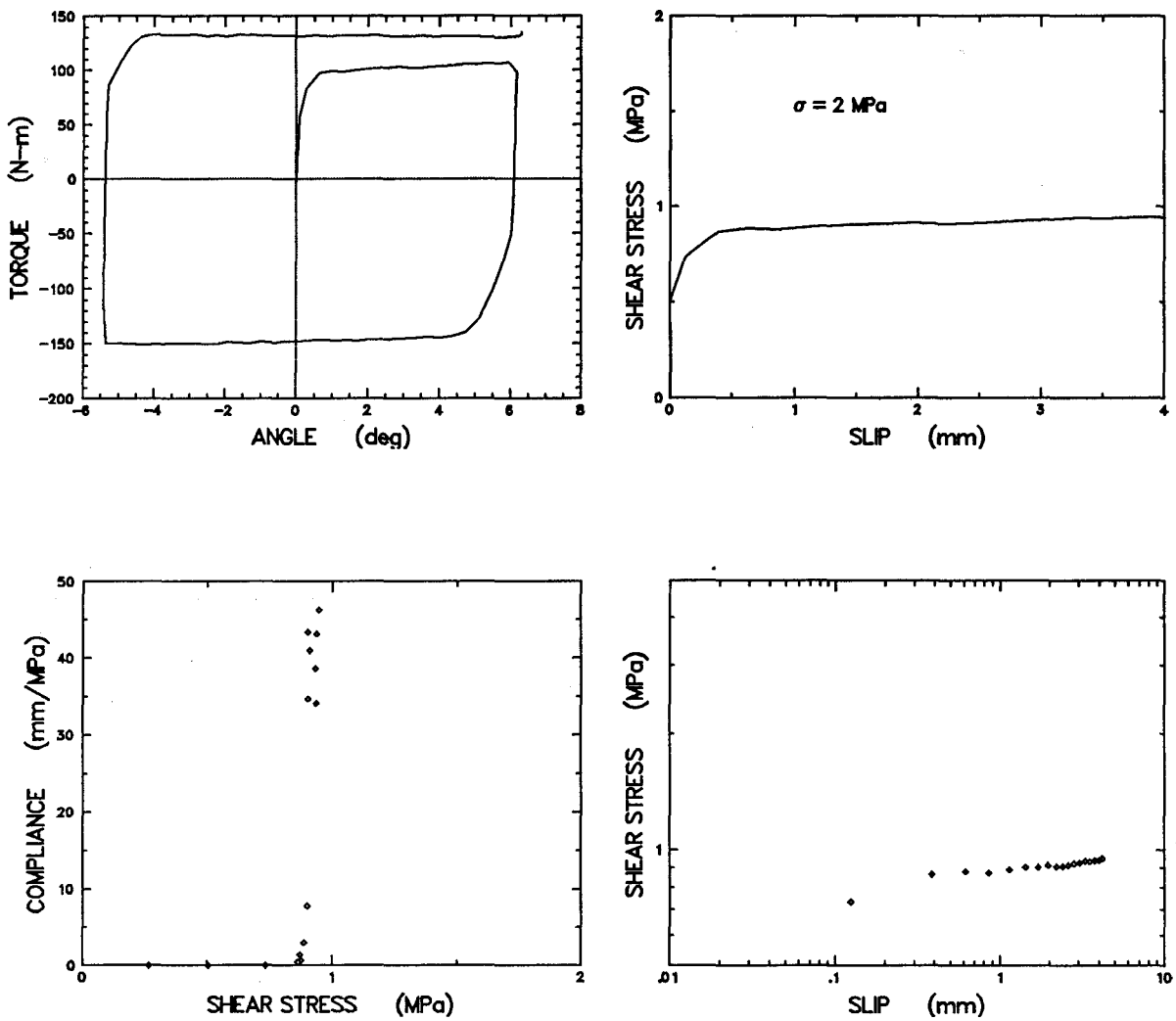

Figure 19: Experiment RFT021, shear compliance test.

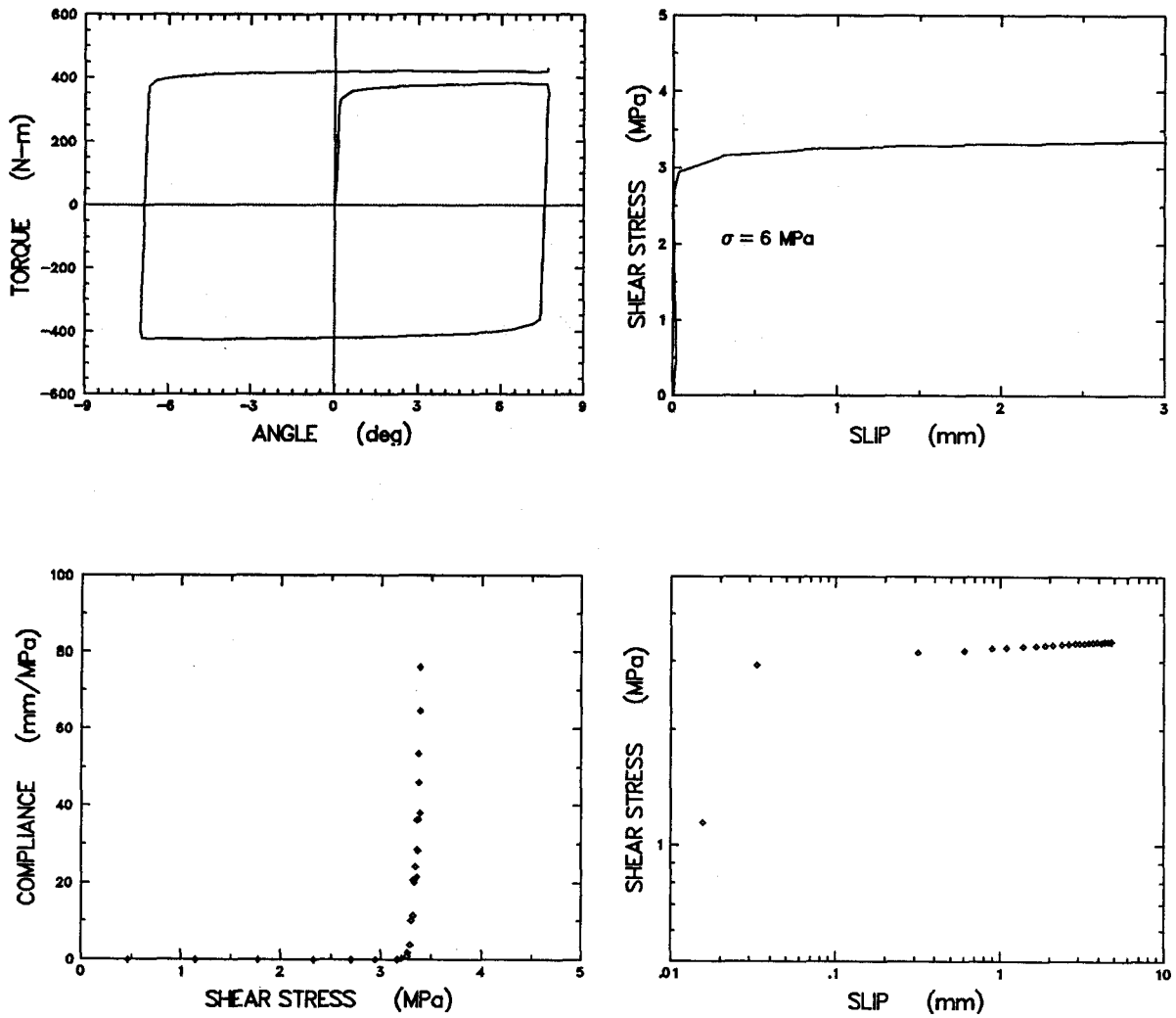

Figure 20: Experiment RFT022, shear compliance test.

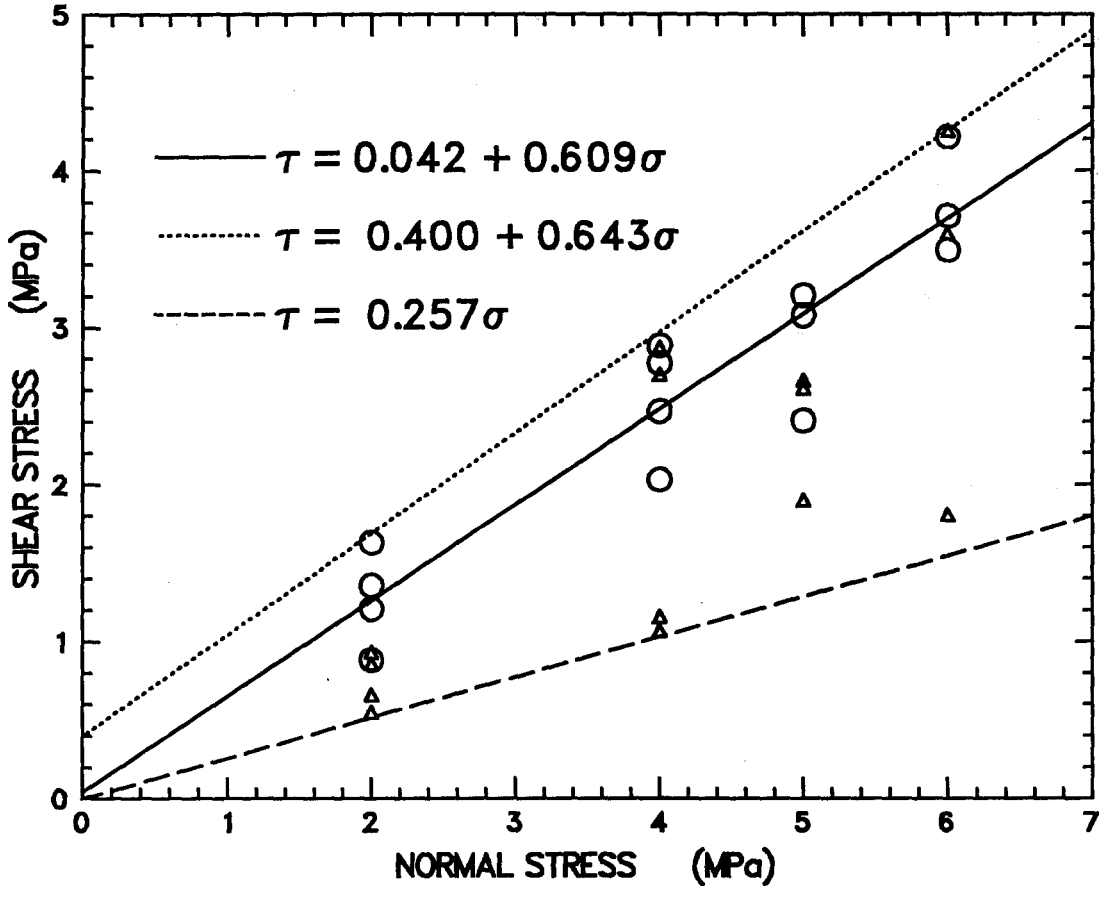

Figure 21: Slip condition for Sample 16C-CC/16B-BB.

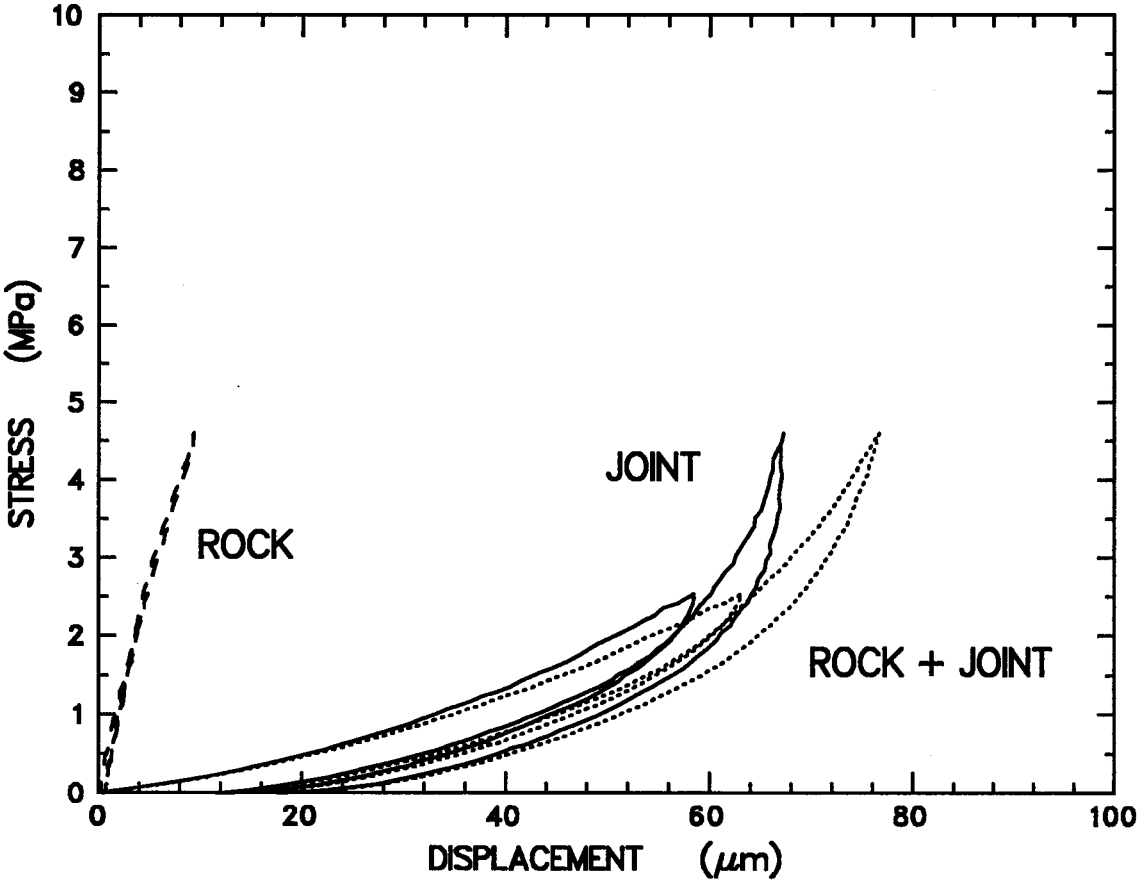

Figure 22: Experiment NST005, normal closure test on mated, rough joint.

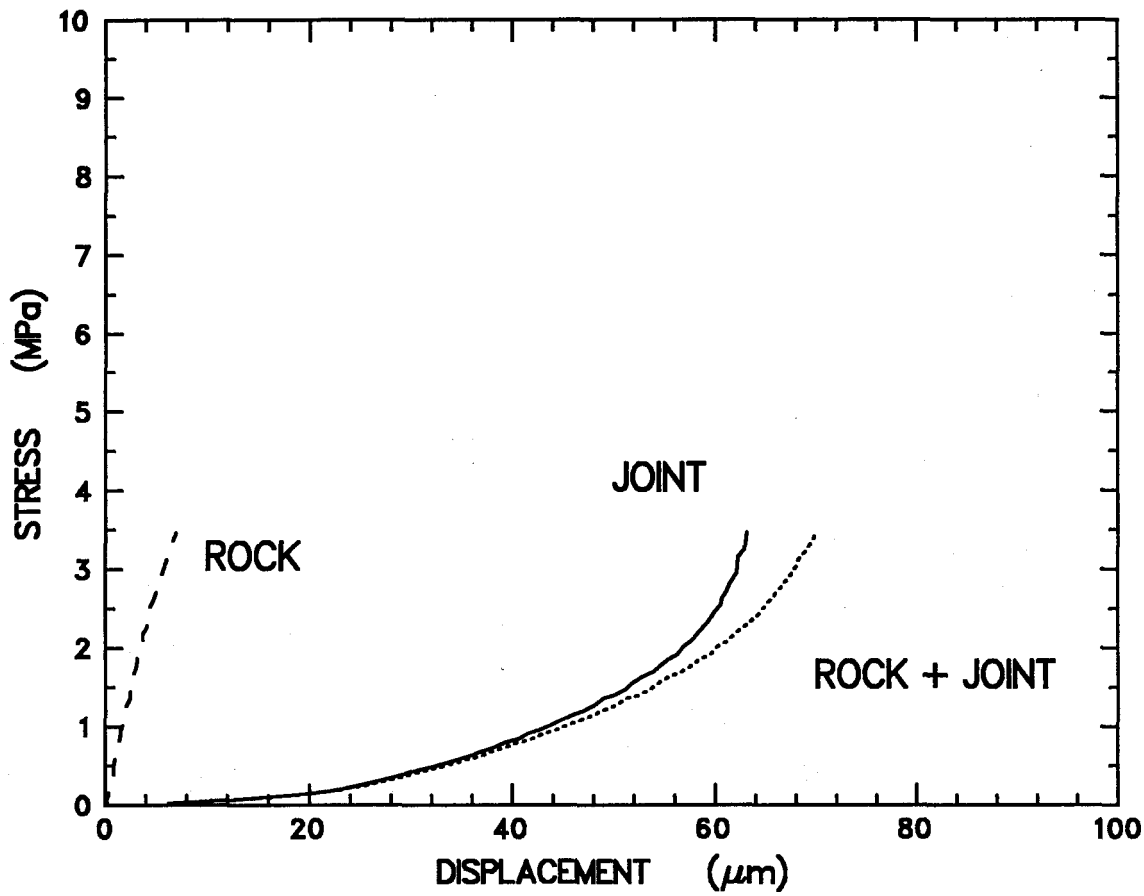

Figure 23: Experiment NST006, normal closure test on mated, rough joint.

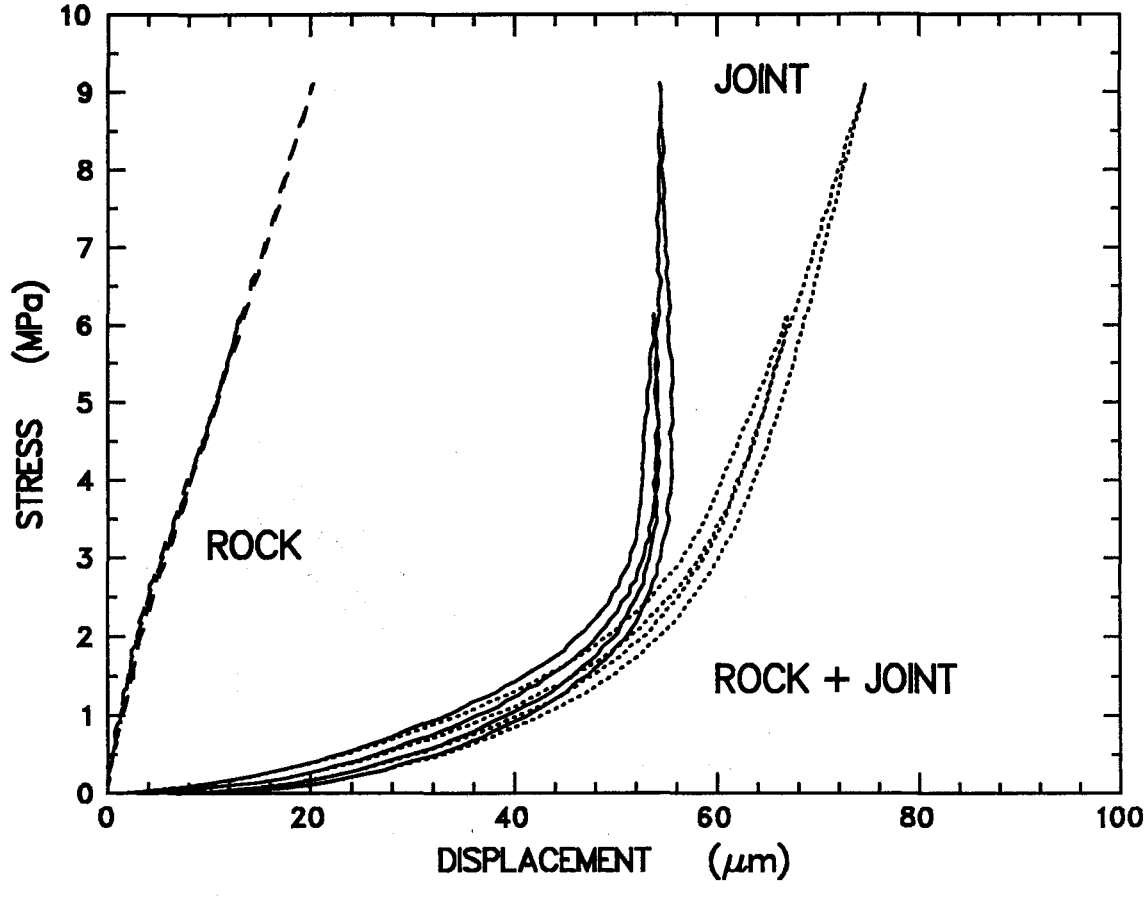

Figure 24: Experiment NST007, normal closure test on mated, rough joint.

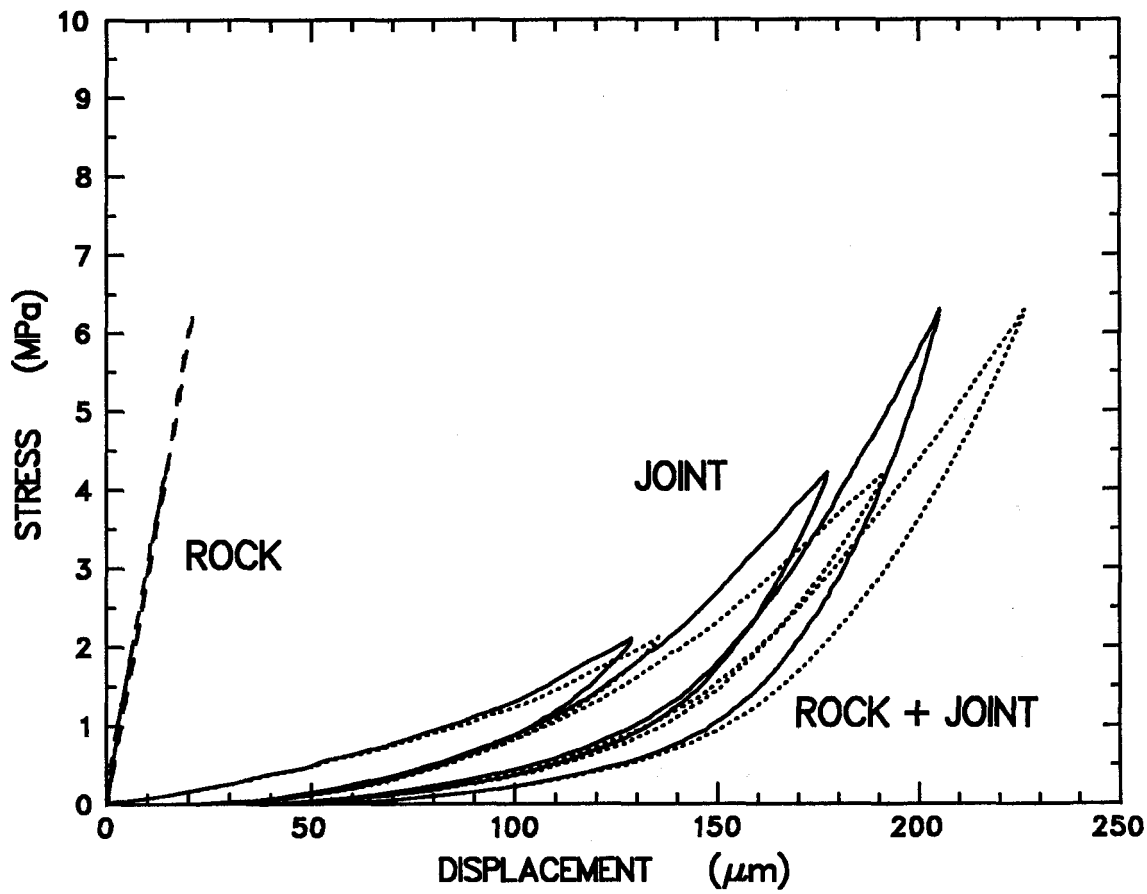

Figure 25: Experiment NST008, normal closure test on unmated, rough joint.

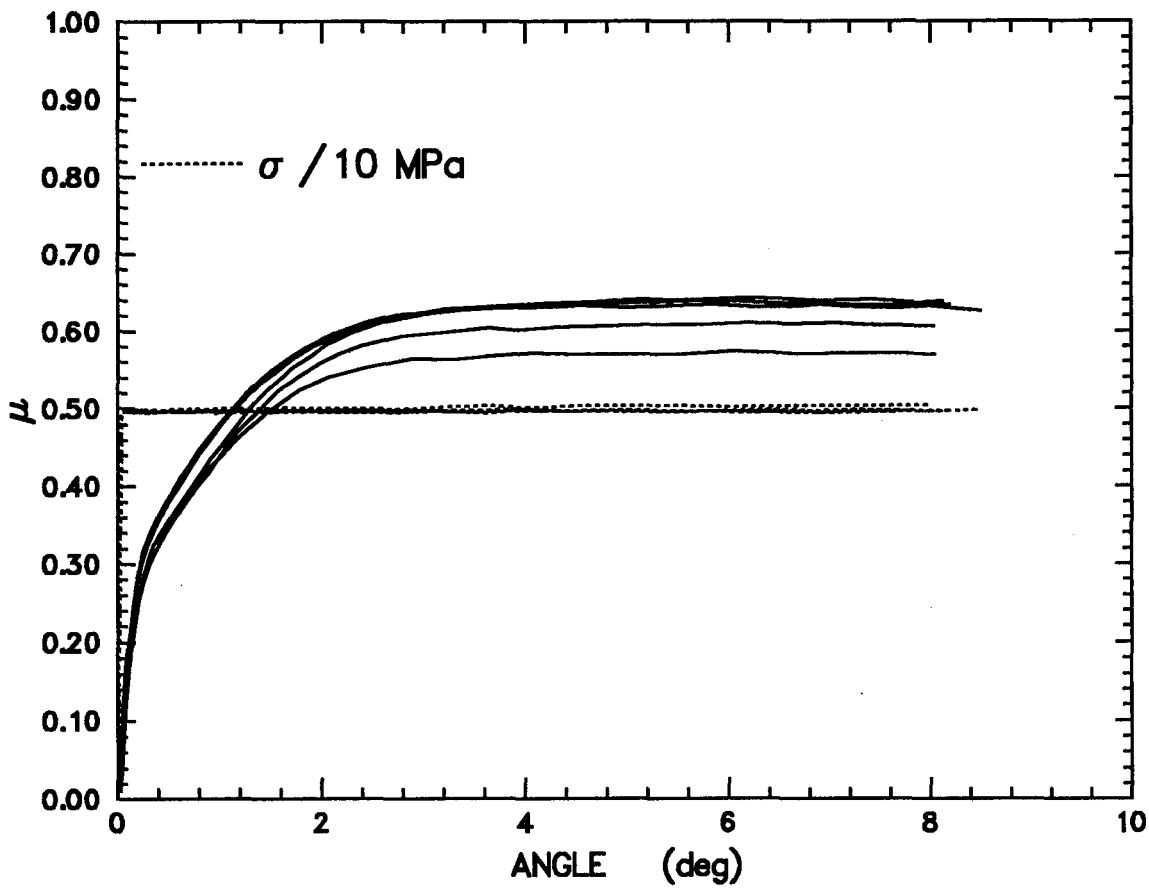

Figure 26: Experiment RFT058, run-in test.

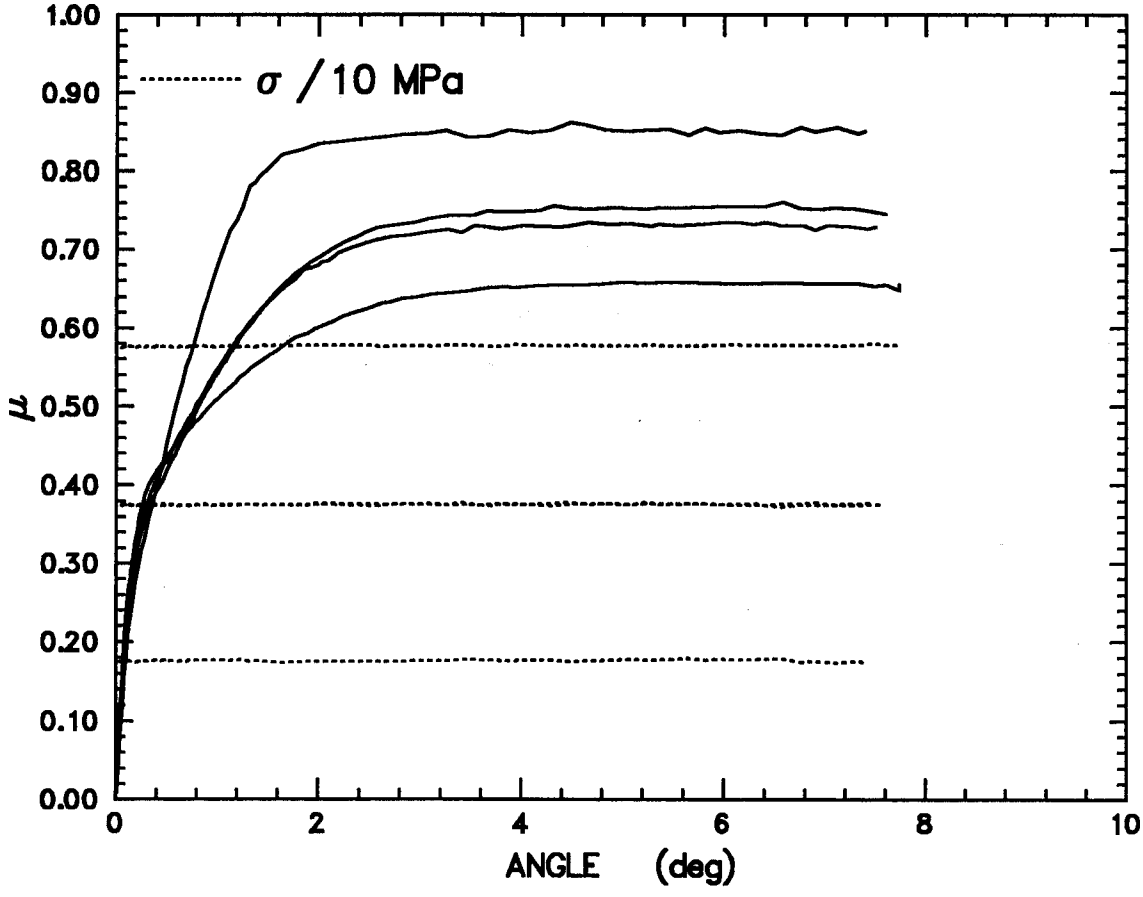

Figure 27: Experiment RFT059, run-in test.

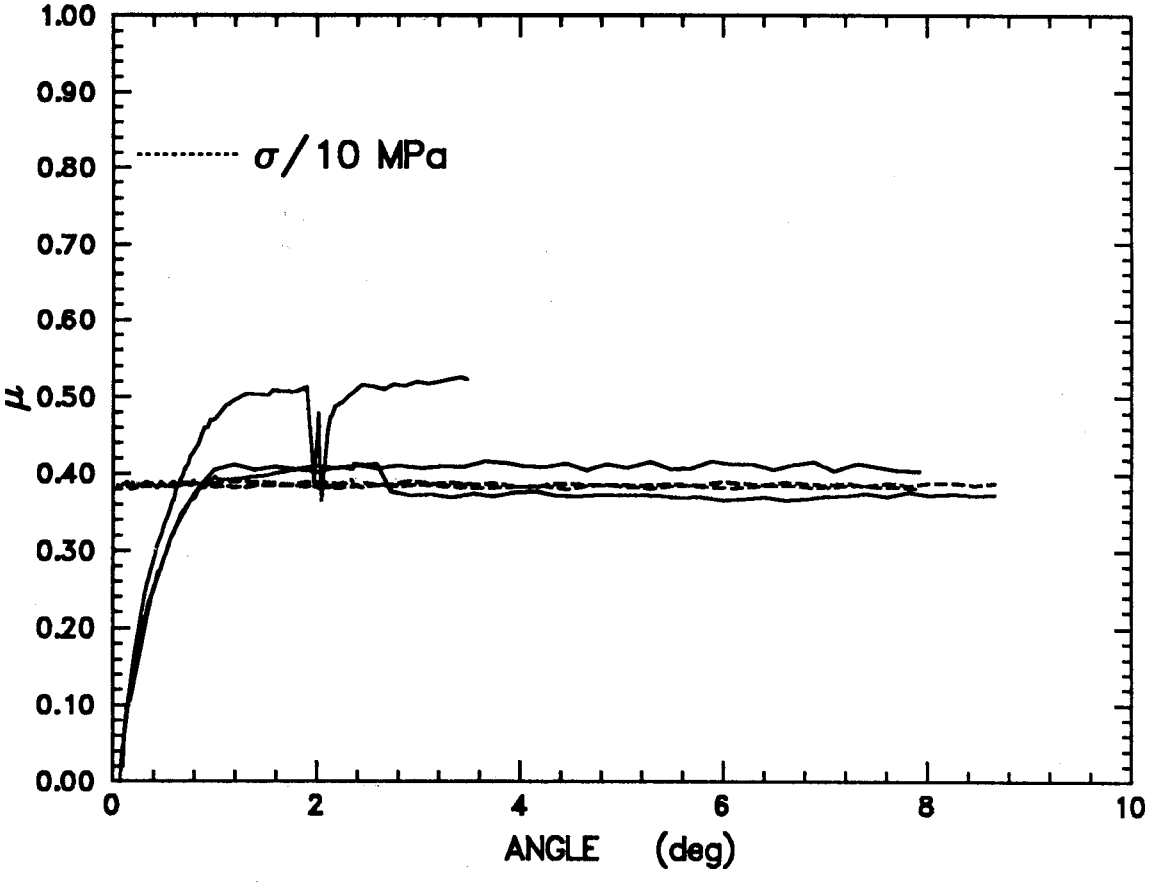

Figure 28: Experiment RFT067, run-in test.

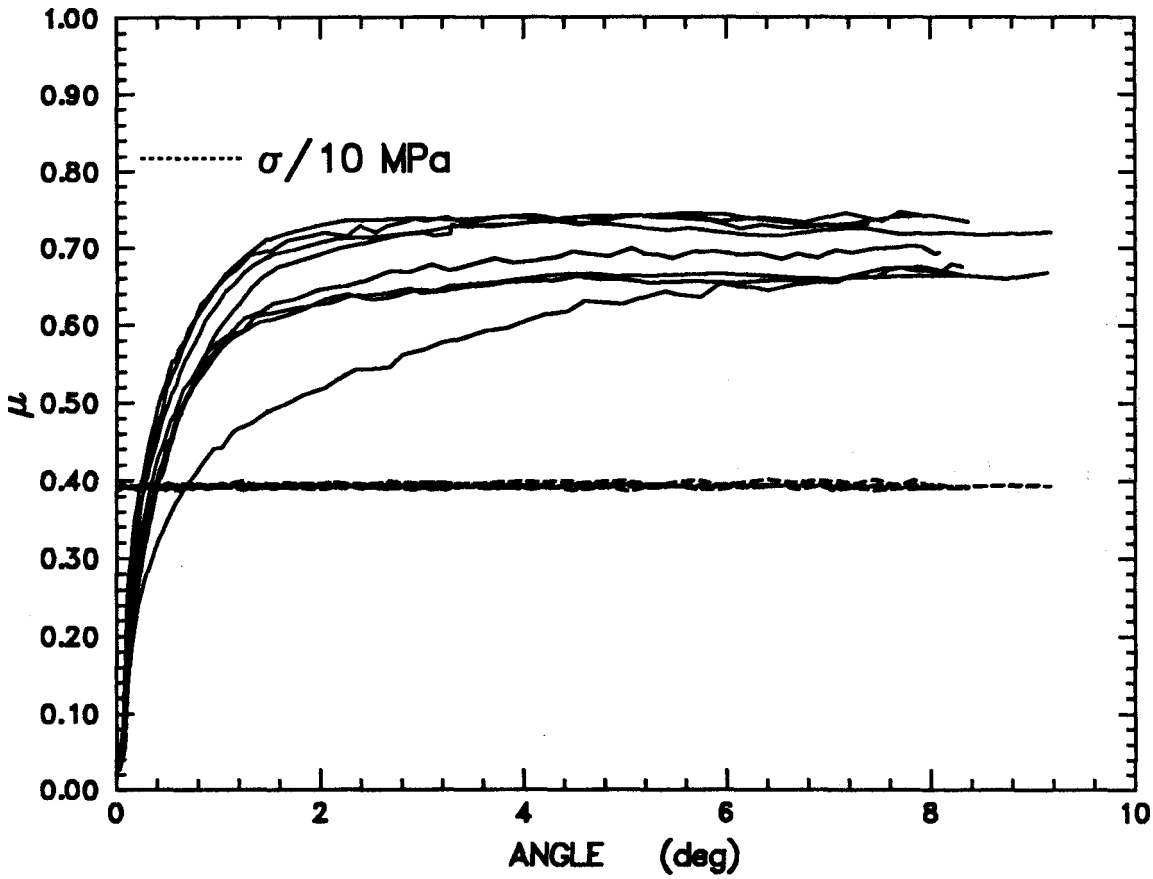

Figure 29: Experiment RFT068, run-in test.

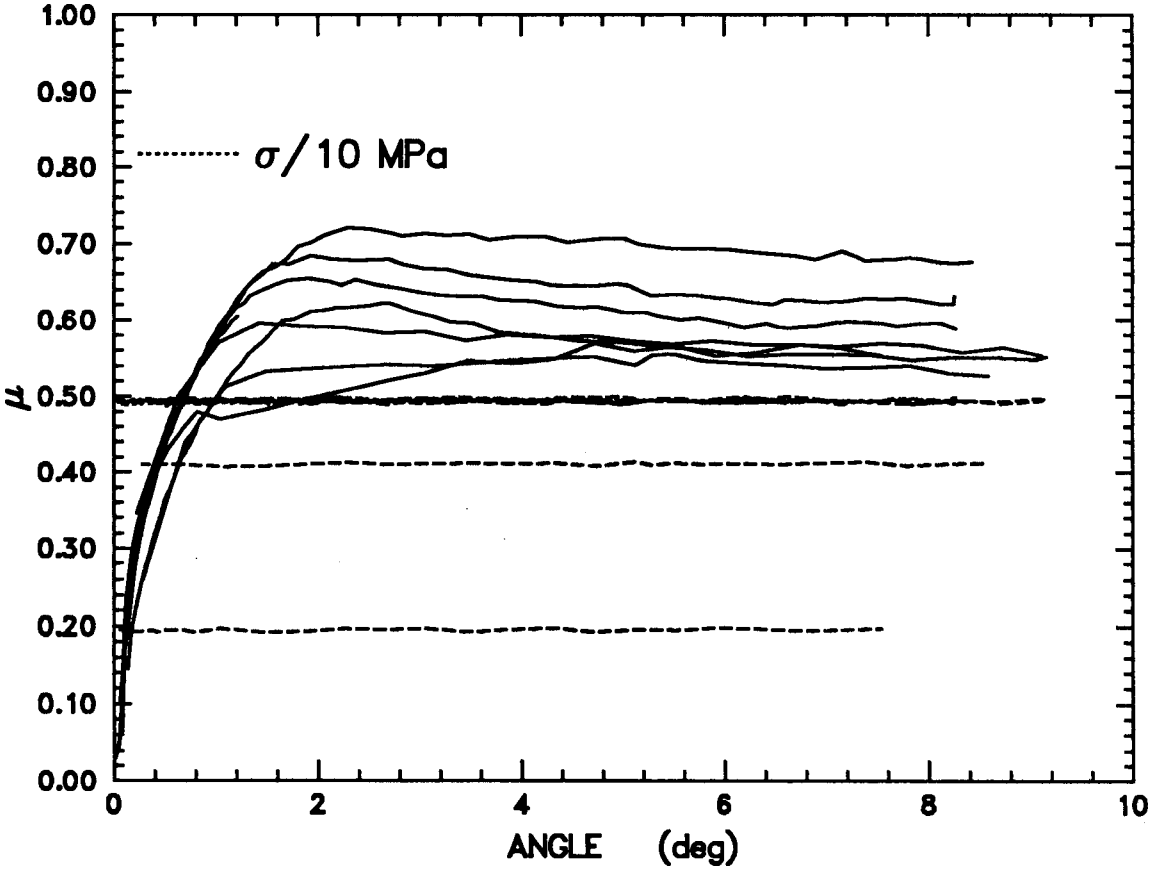

Figure 30: Experiment RFT069, run-in test.

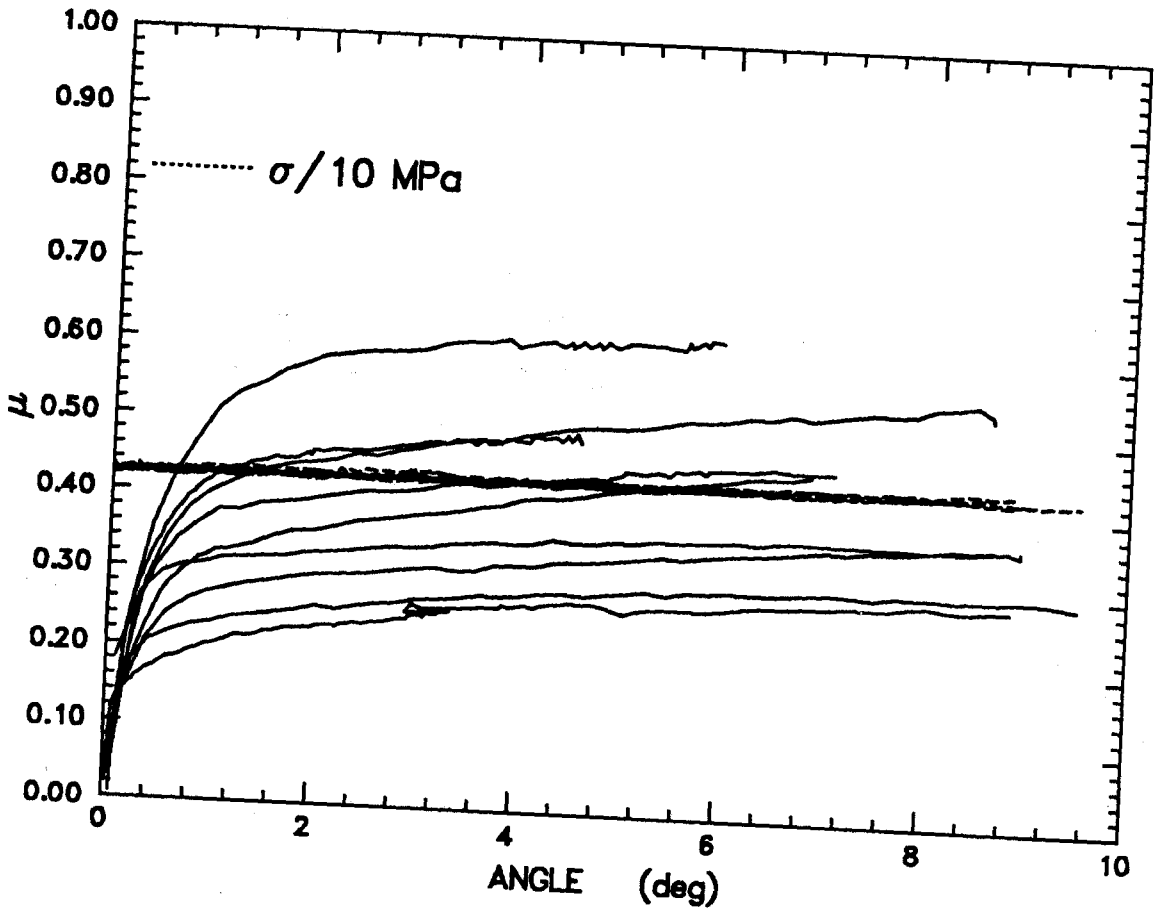

Figure 31: Experiment RFT070, run-in test.

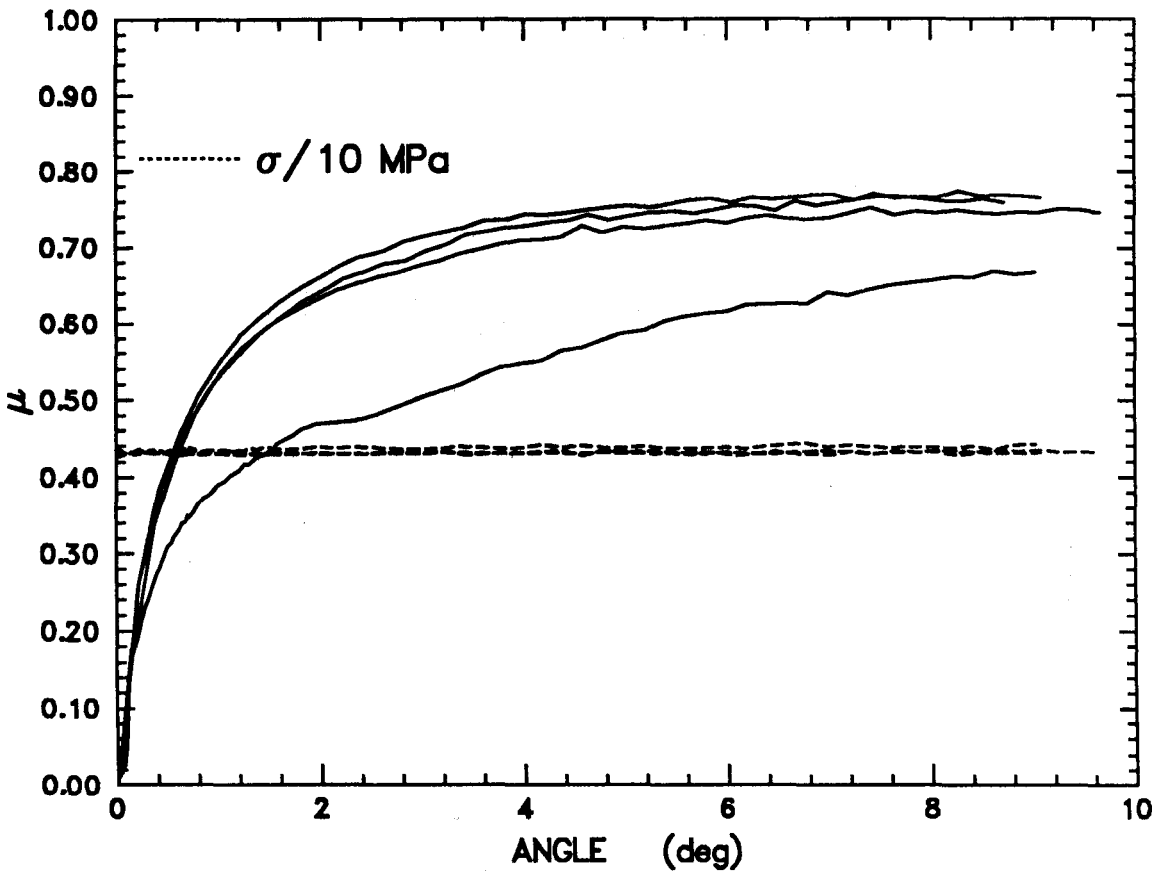

Figure 32: Experiment RFT072, run-in test.

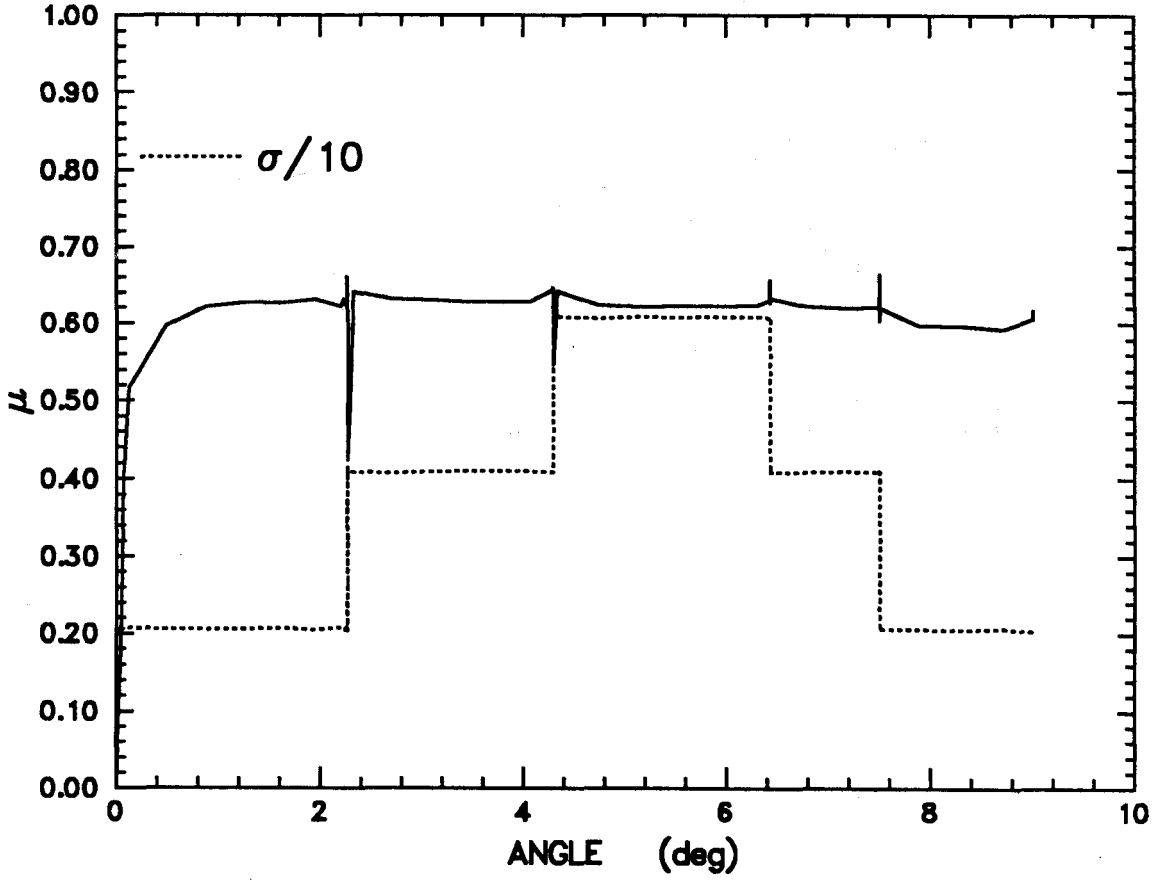

Figure 33: Experiment RFT023, normal stress-history test.

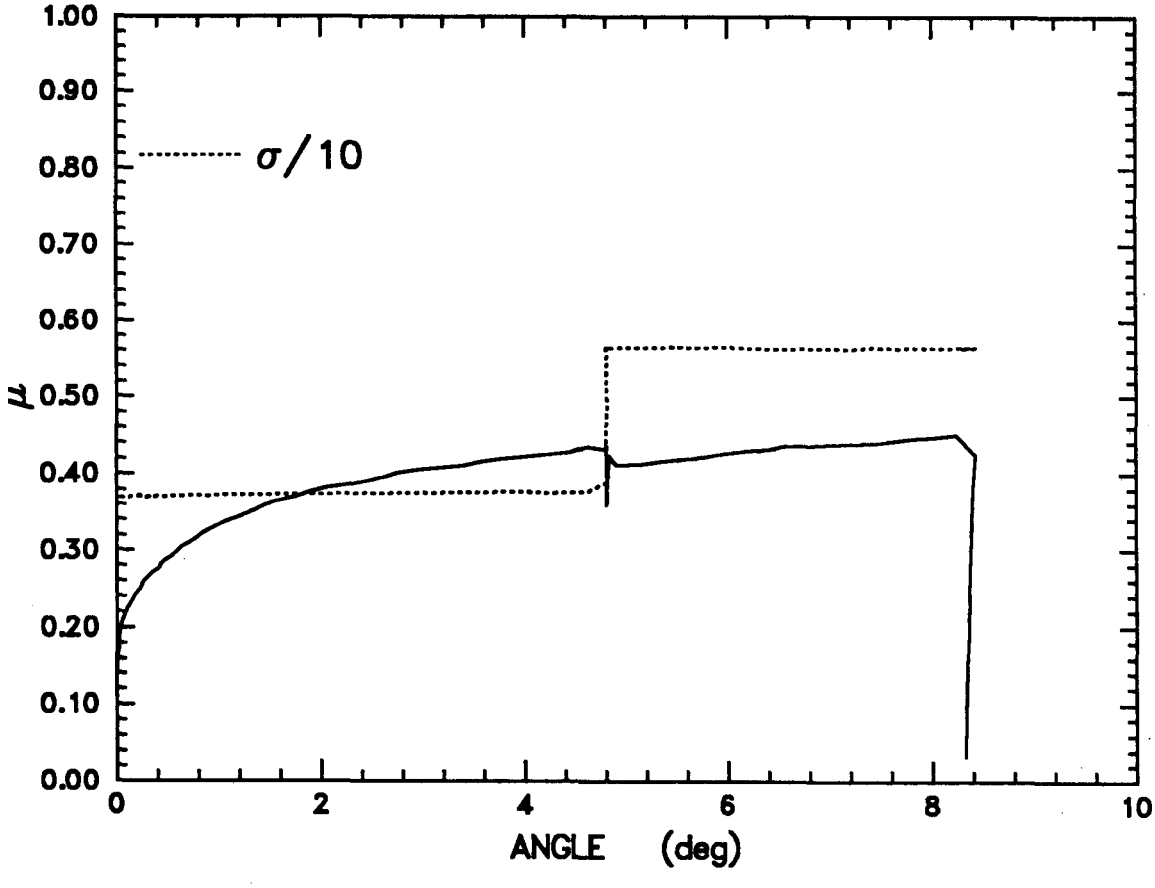

Figure 34: Experiment RFT024, normal stress-history test.

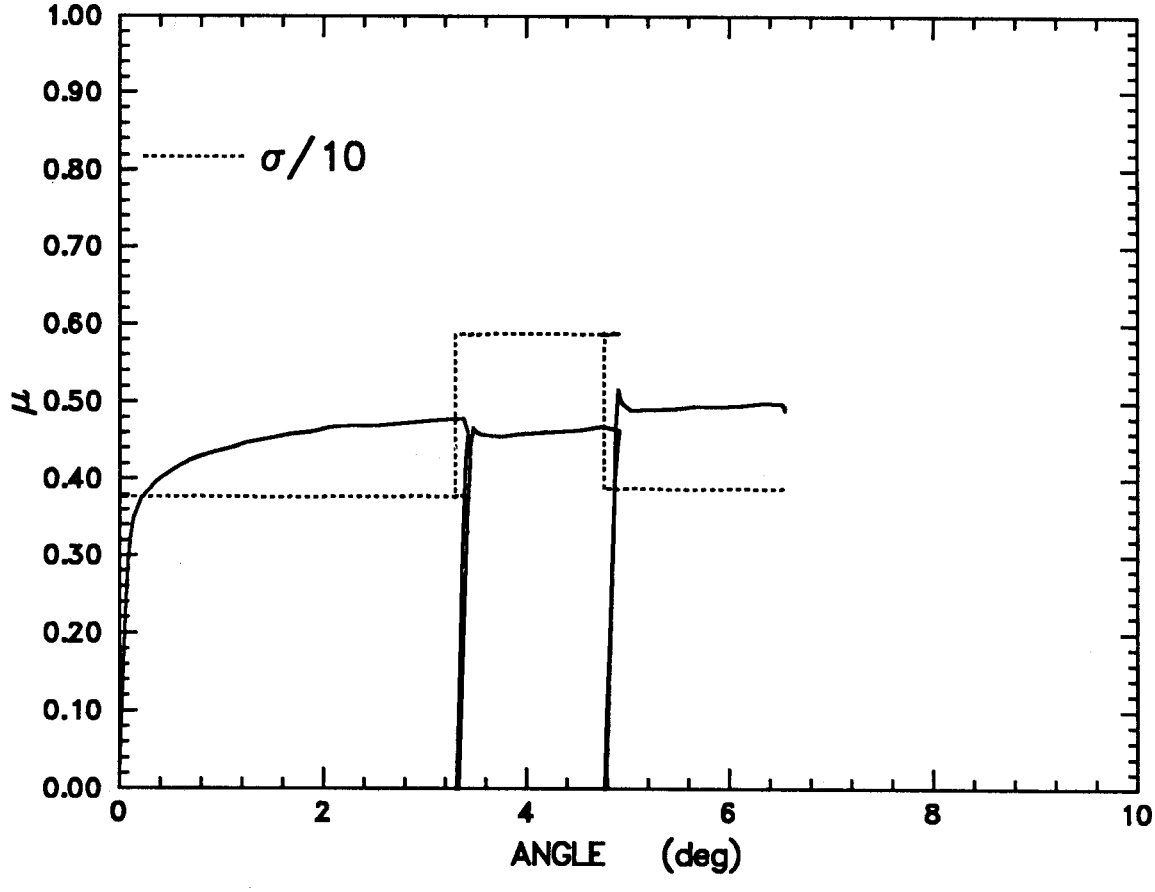

Figure 35: Experiment RFT025, normal stress-history test.

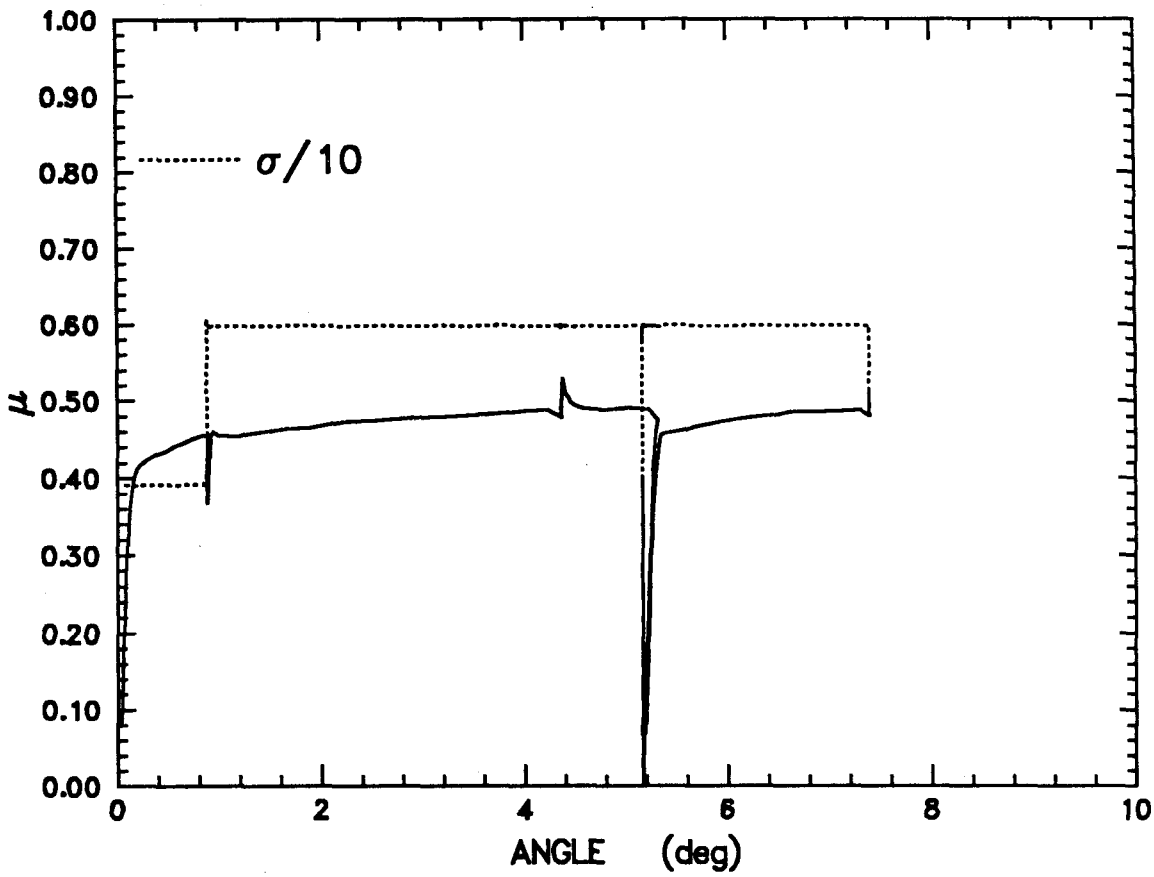

Figure 36: Experiment RFT026, normal stress-history test.

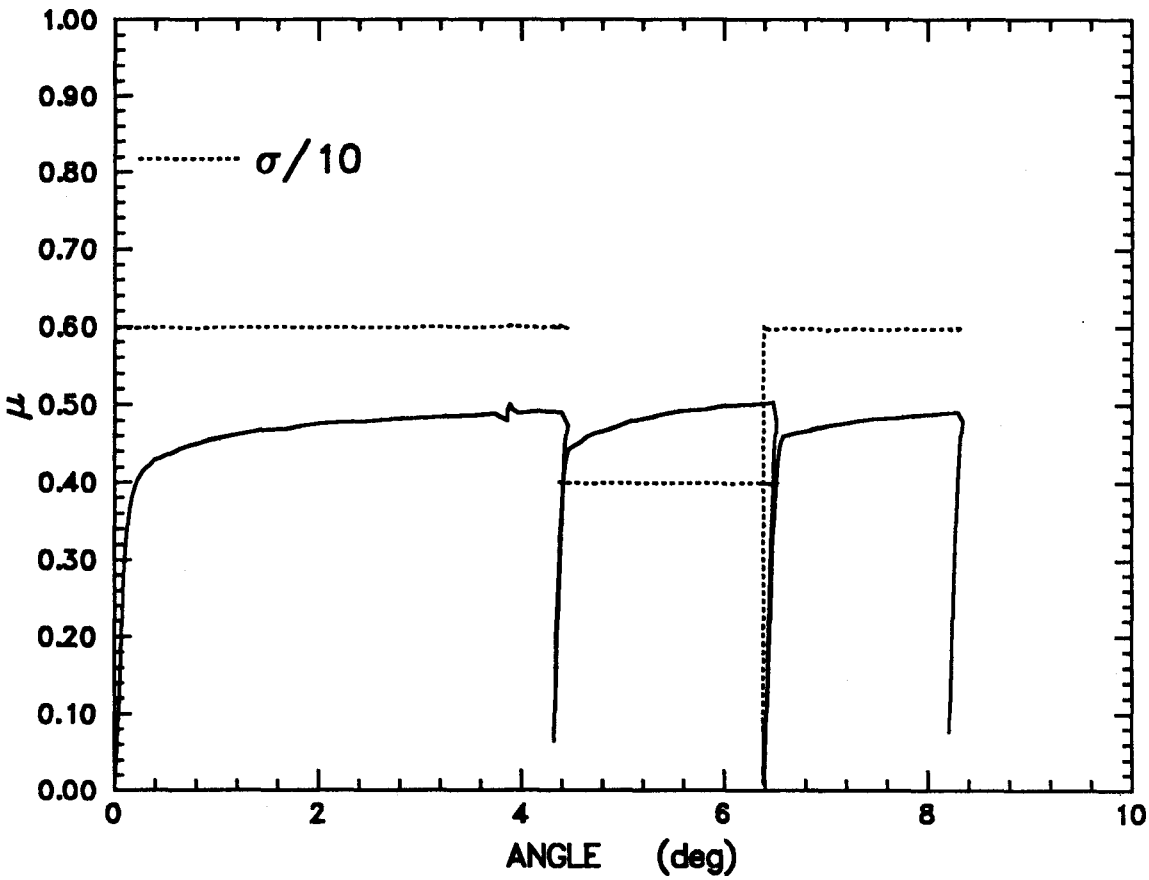

Figure 37: Experiment RFT027, normal stress-history test.

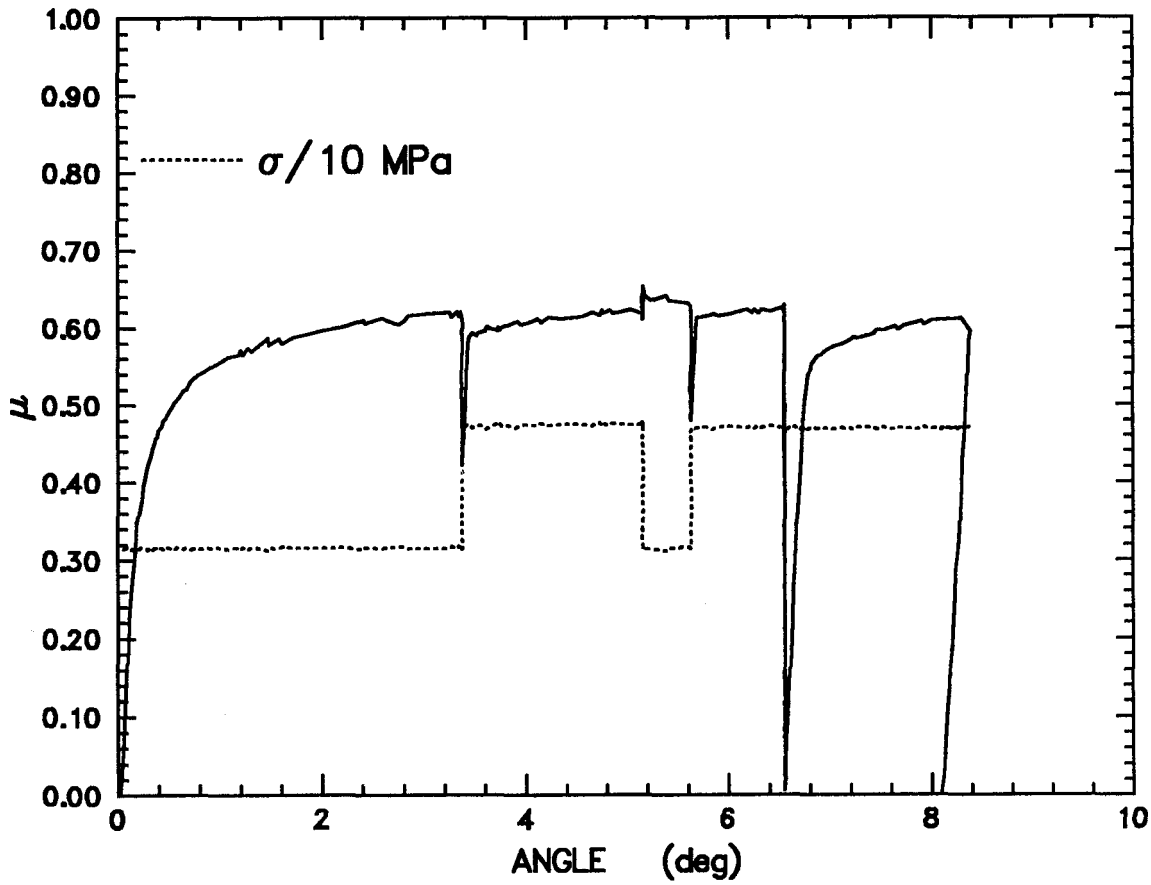

Figure 38: Experiment RFT029, normal stress-history test.

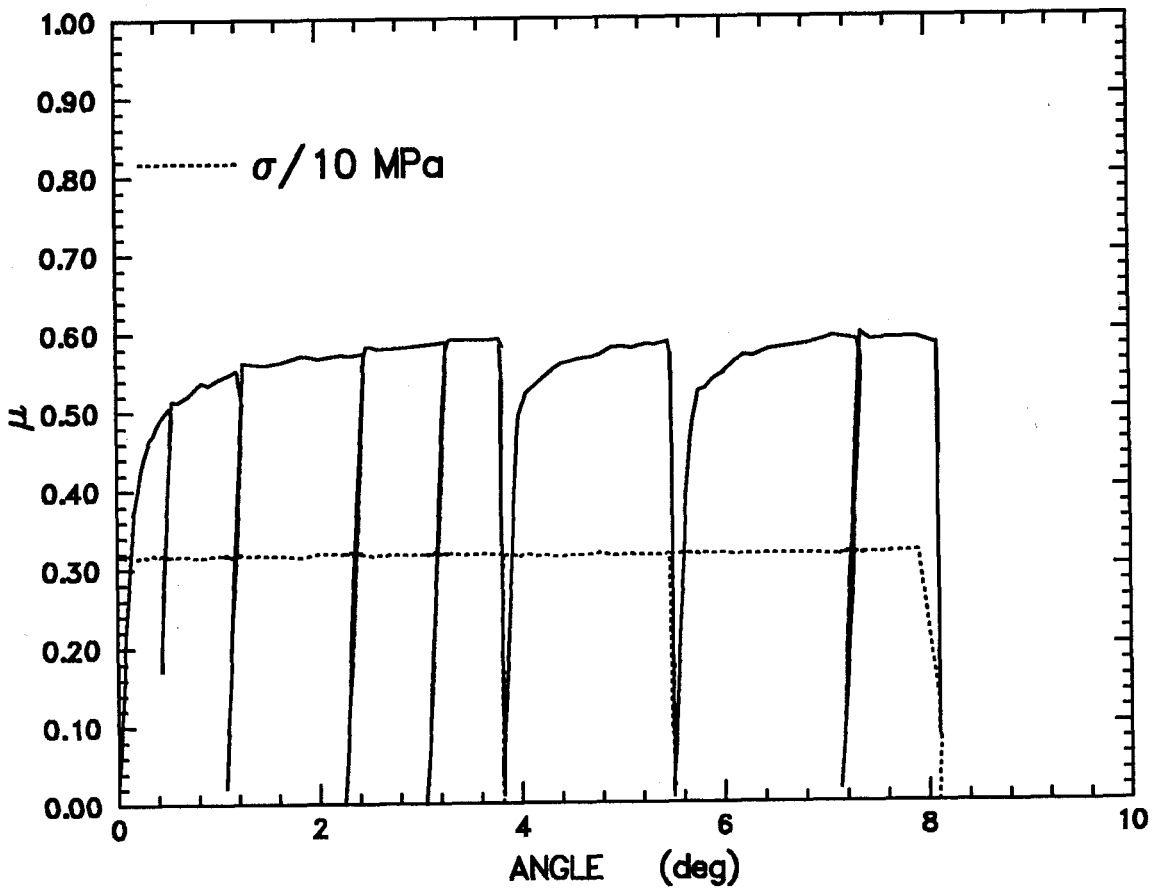

Figure 39: Experiment RFT030, normal stress-history test.

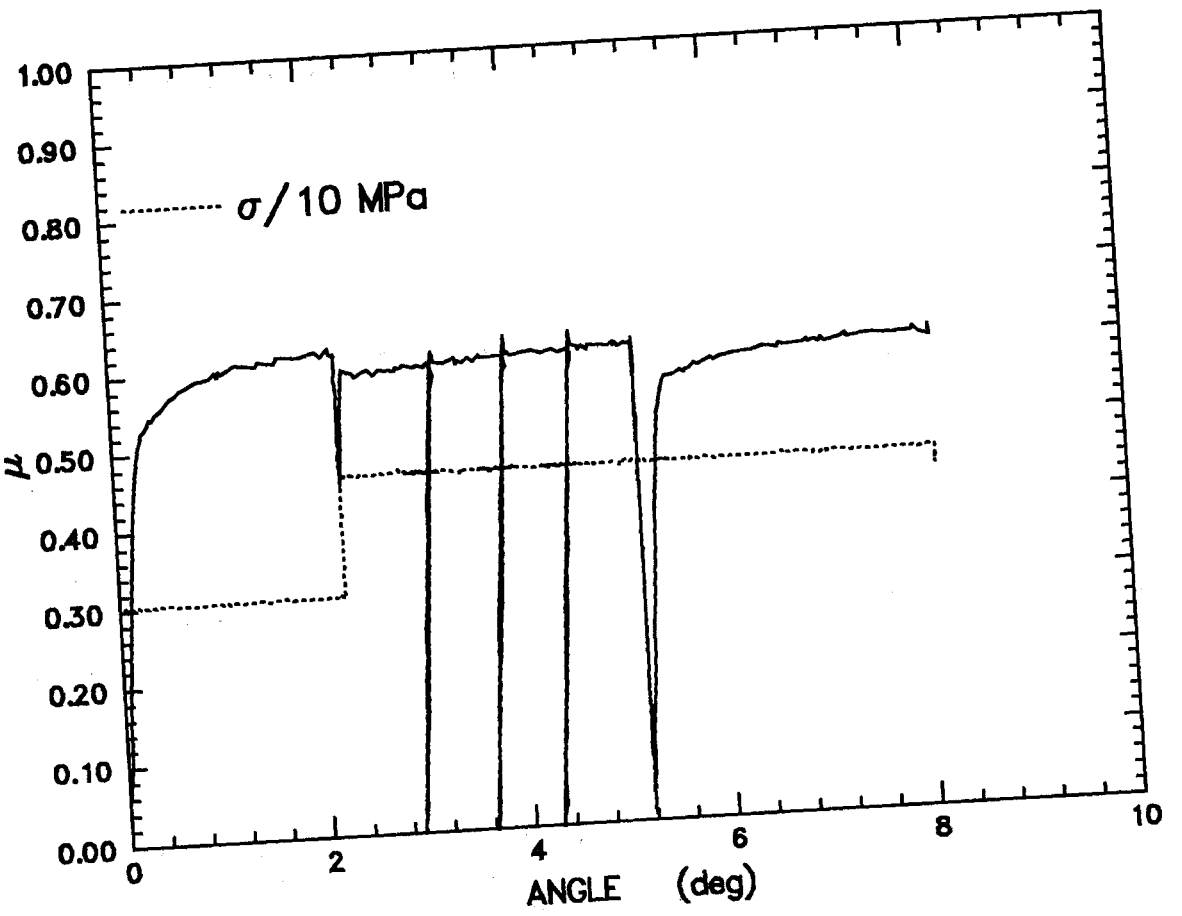

Figure 40: Experiment RFT031, normal stress-history test.

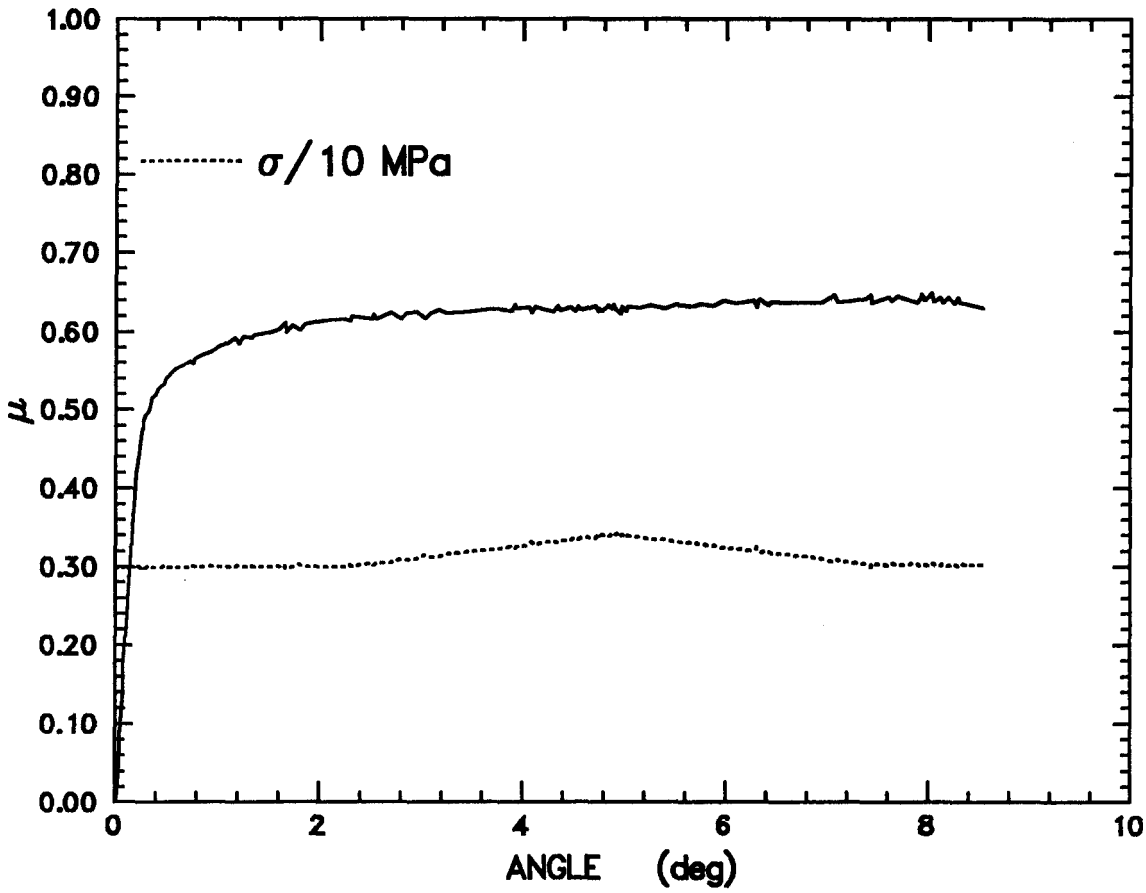

Figure 41: Experiment RFT032, normal stress-history test.

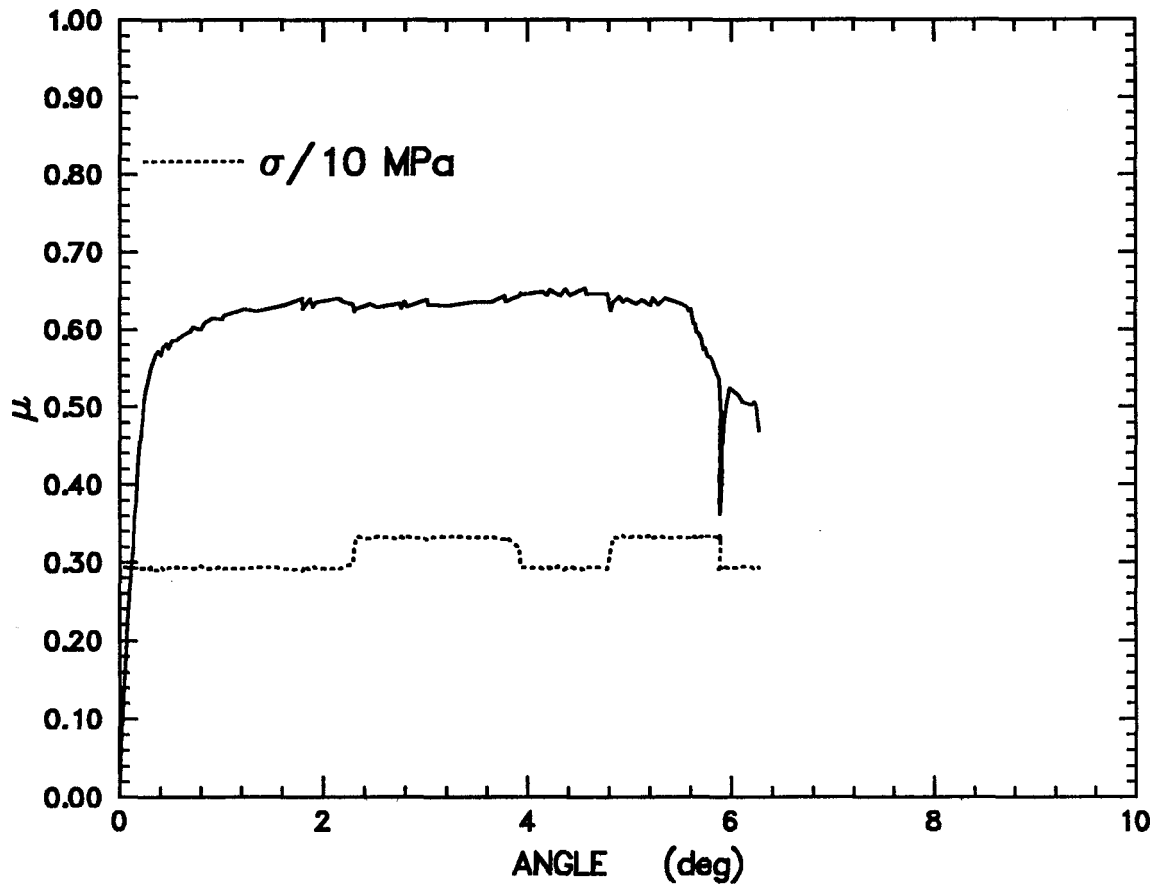

Figure 42: Experiment RFT033, normal stress-history test.

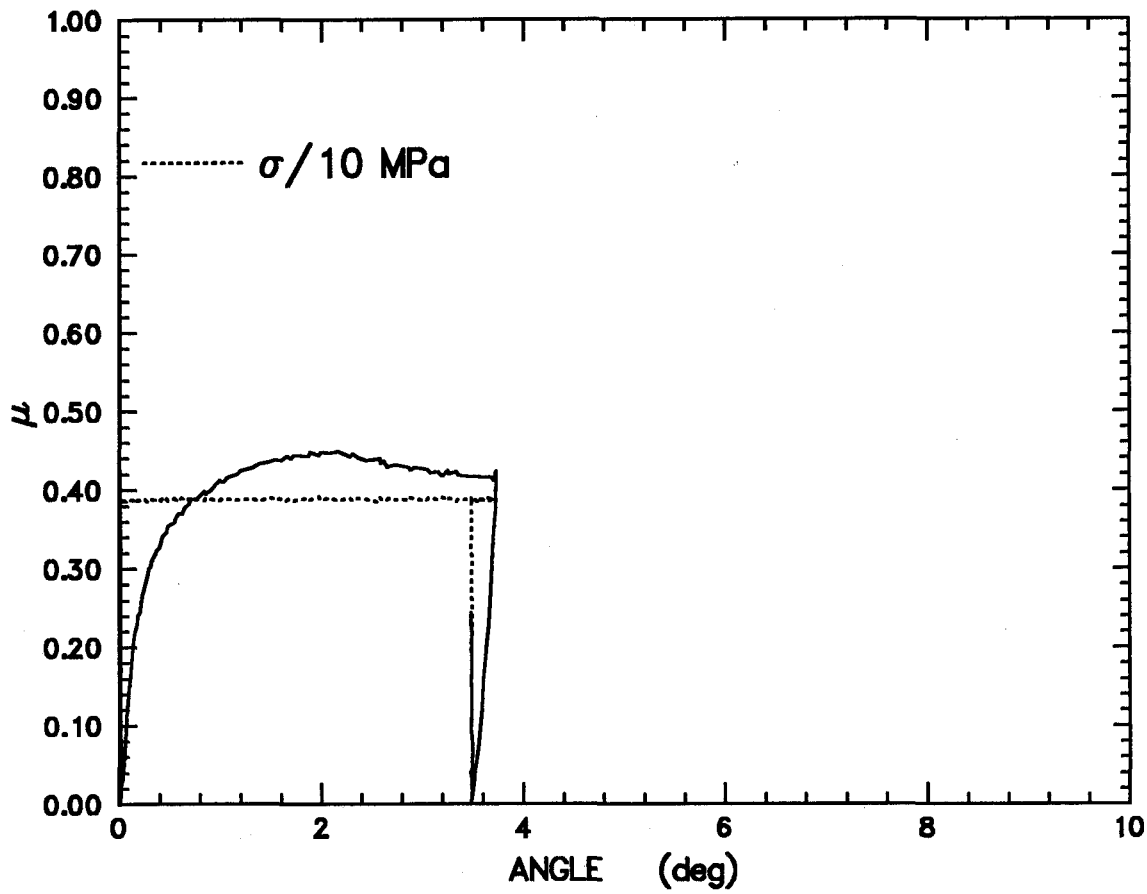

Figure 43: Experiment RFT034, normal stress-history test.

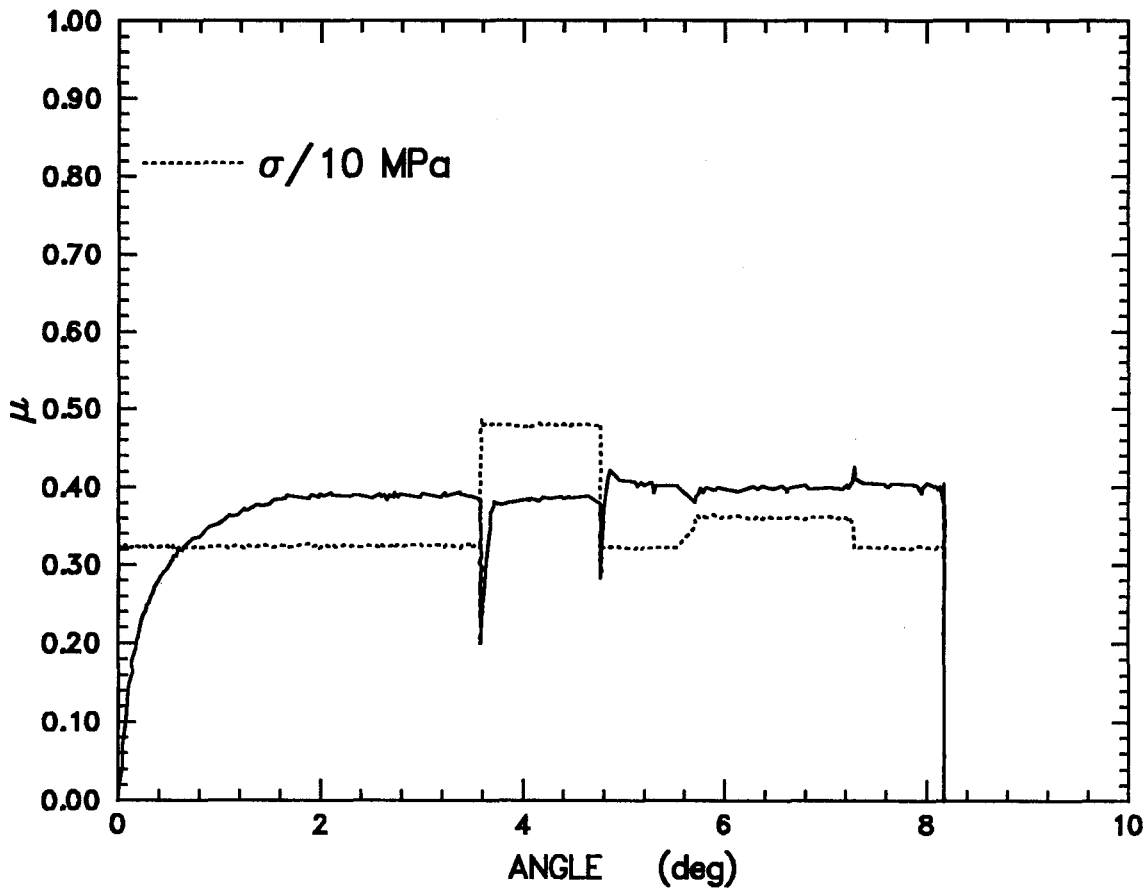

Figure 44: Experiment RFT035, normal stress-history test.

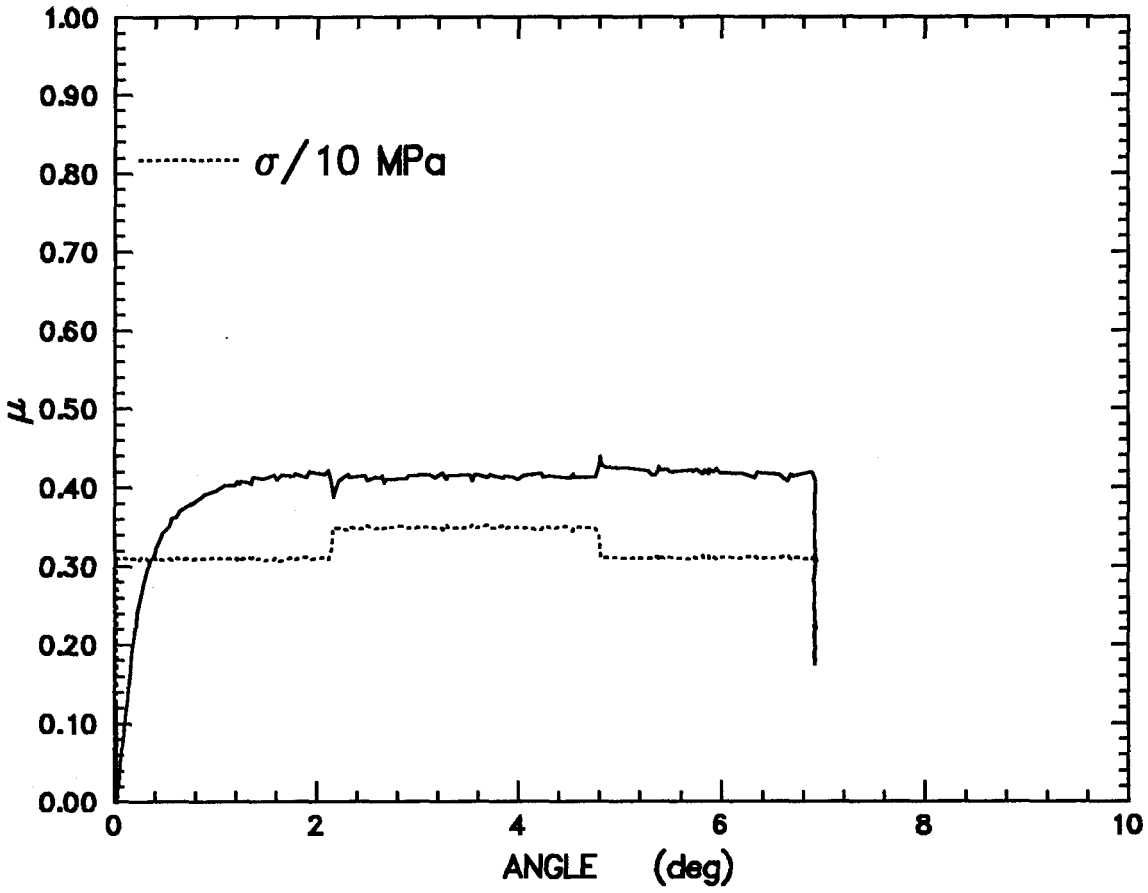

Figure 45: Experiment RFT036, normal stress-history test.

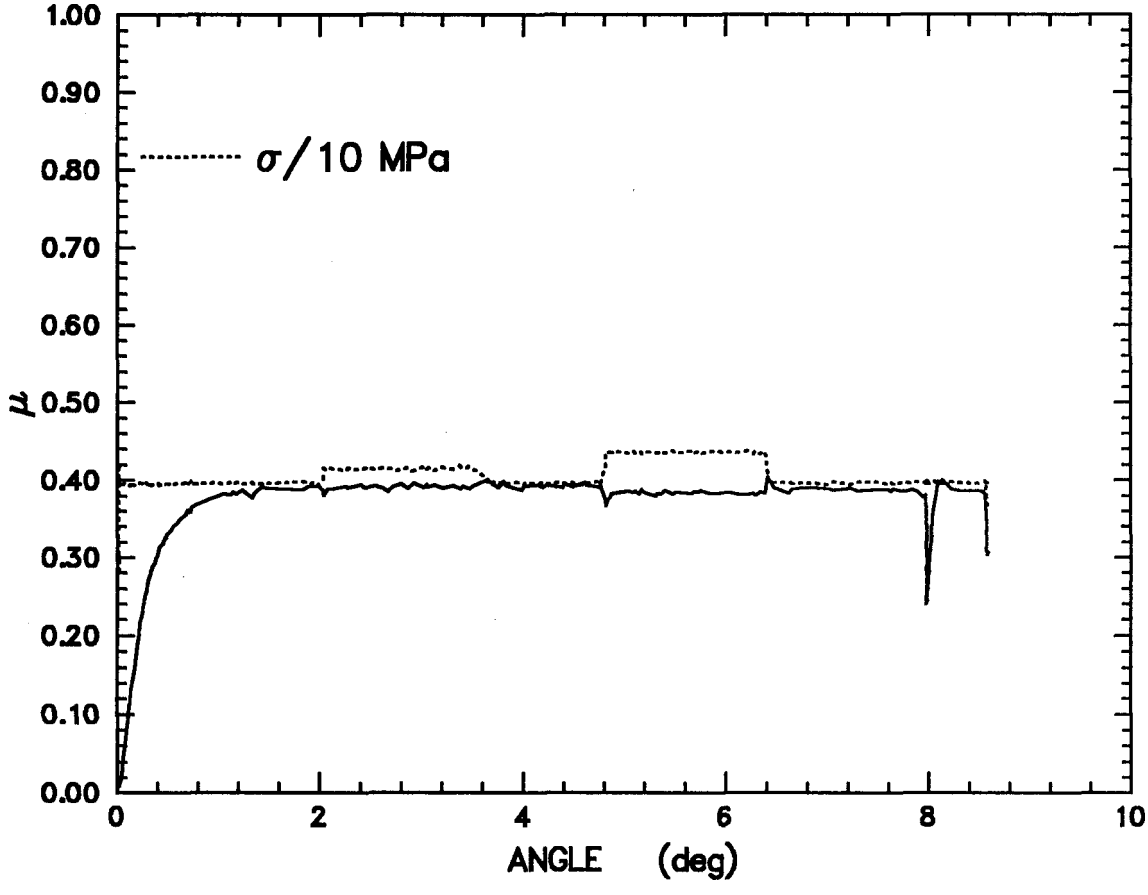

Figure 46: Experiment RFT037, normal stress-history test.

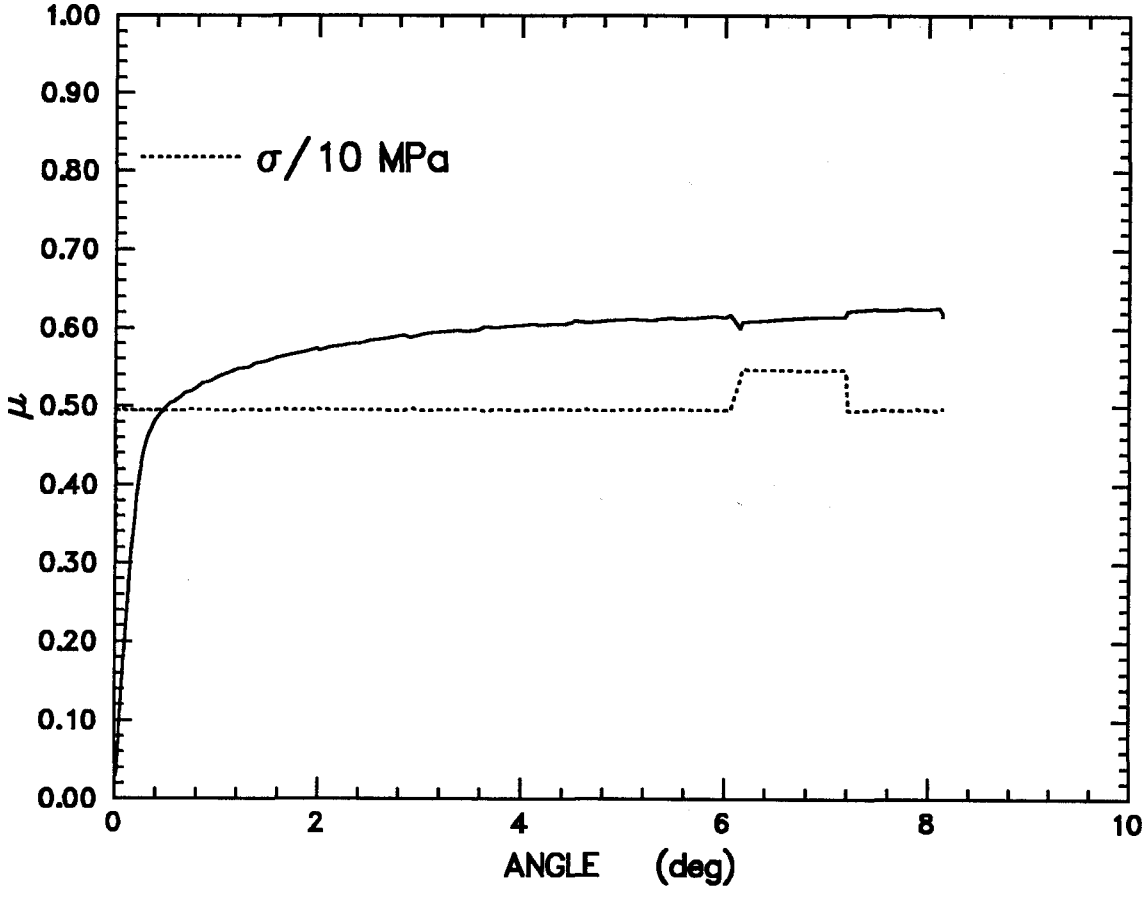

Figure 47: Experiment RFT039 normal stress-history test.

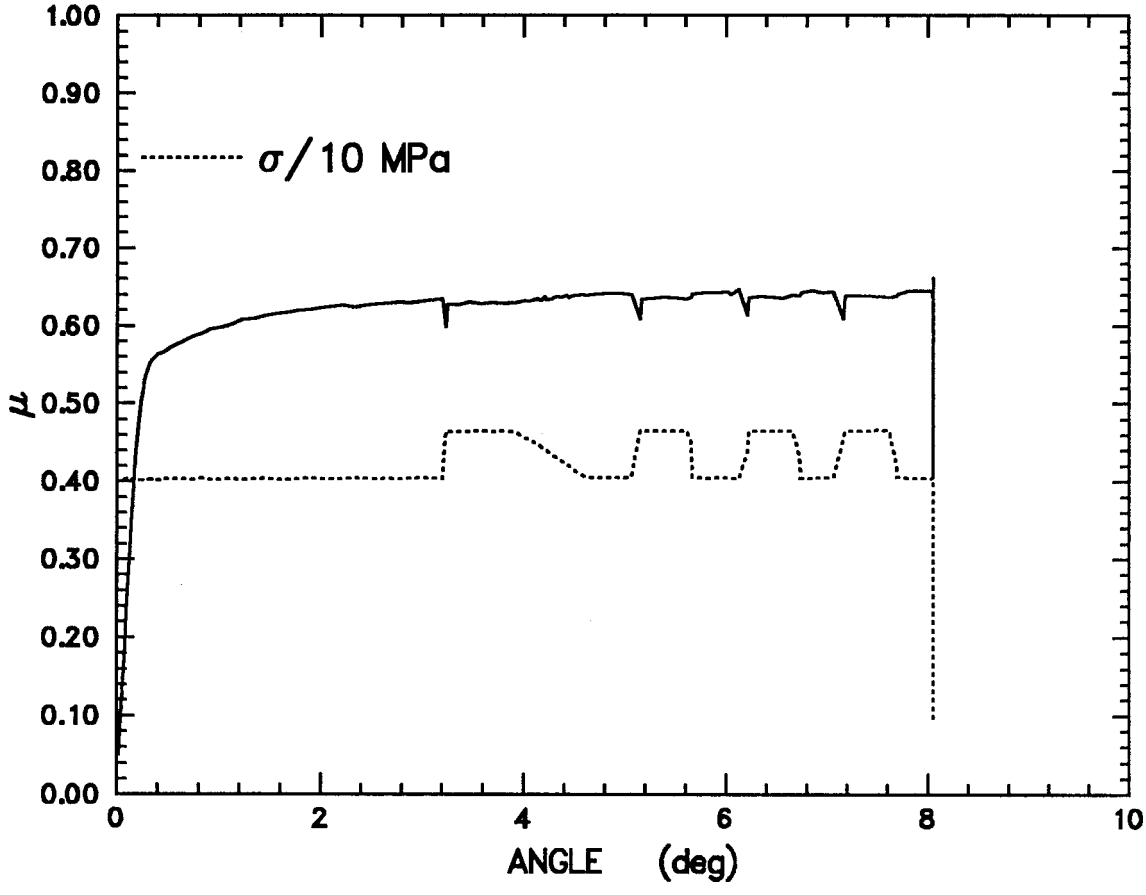

Figure 48: Experiment RFT040, normal stress-history test.

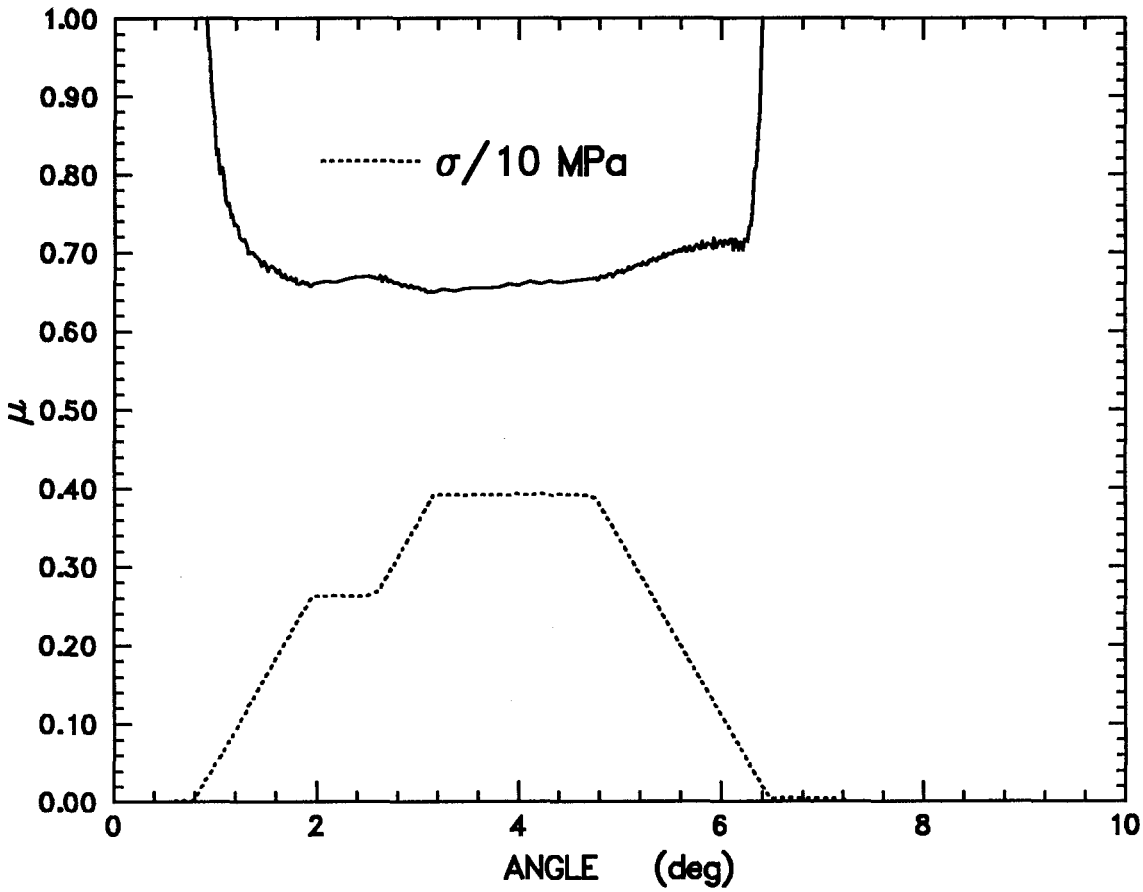

Figure 49: Experiment RFT041, normal stress-history test.

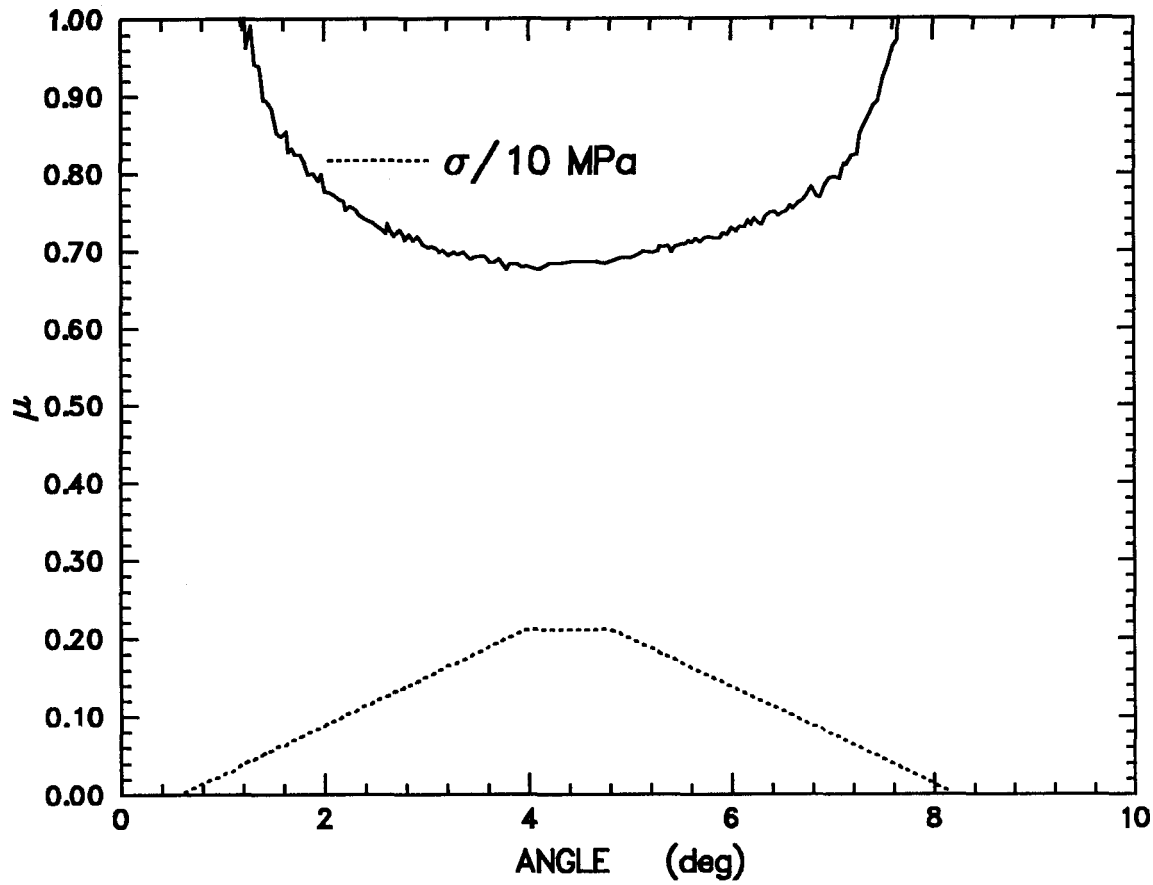

Figure 50: Experiment RFT042, normal stress-history test.

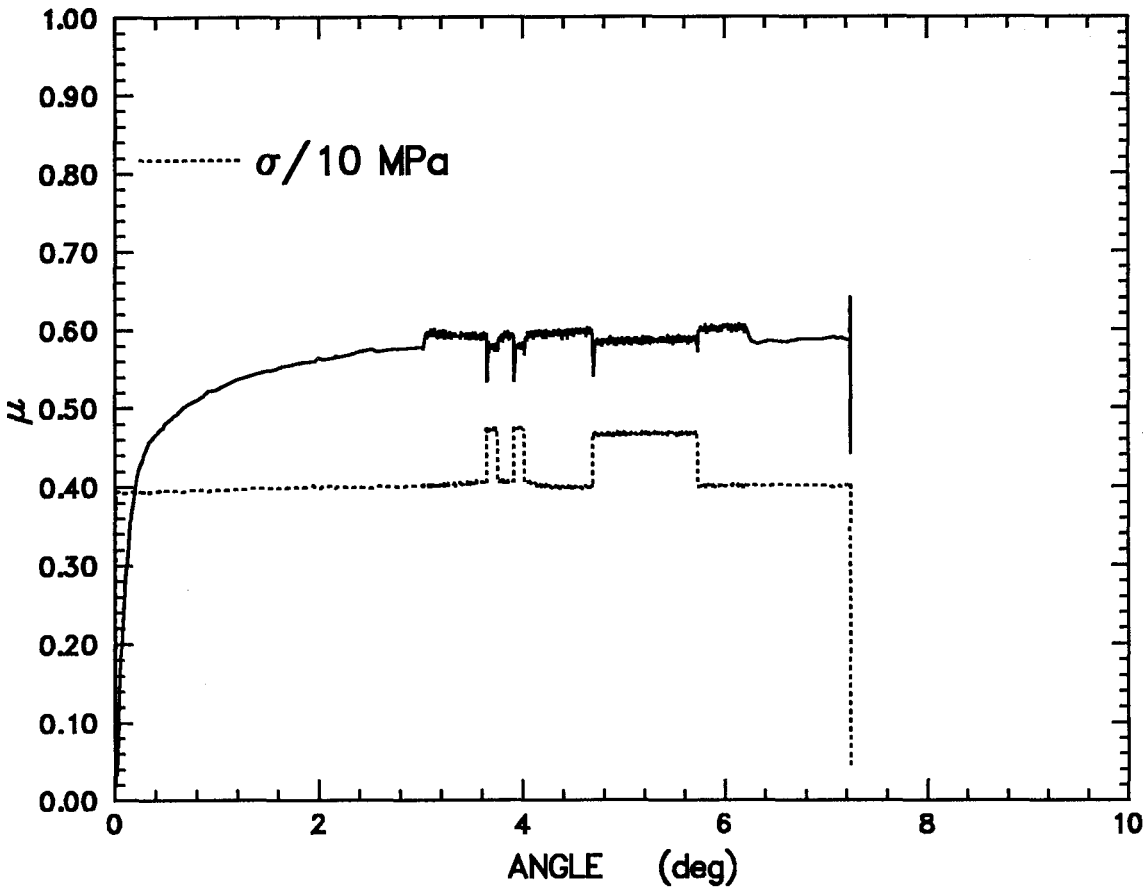

Figure 51: Experiment RFT044, normal stress-history test.

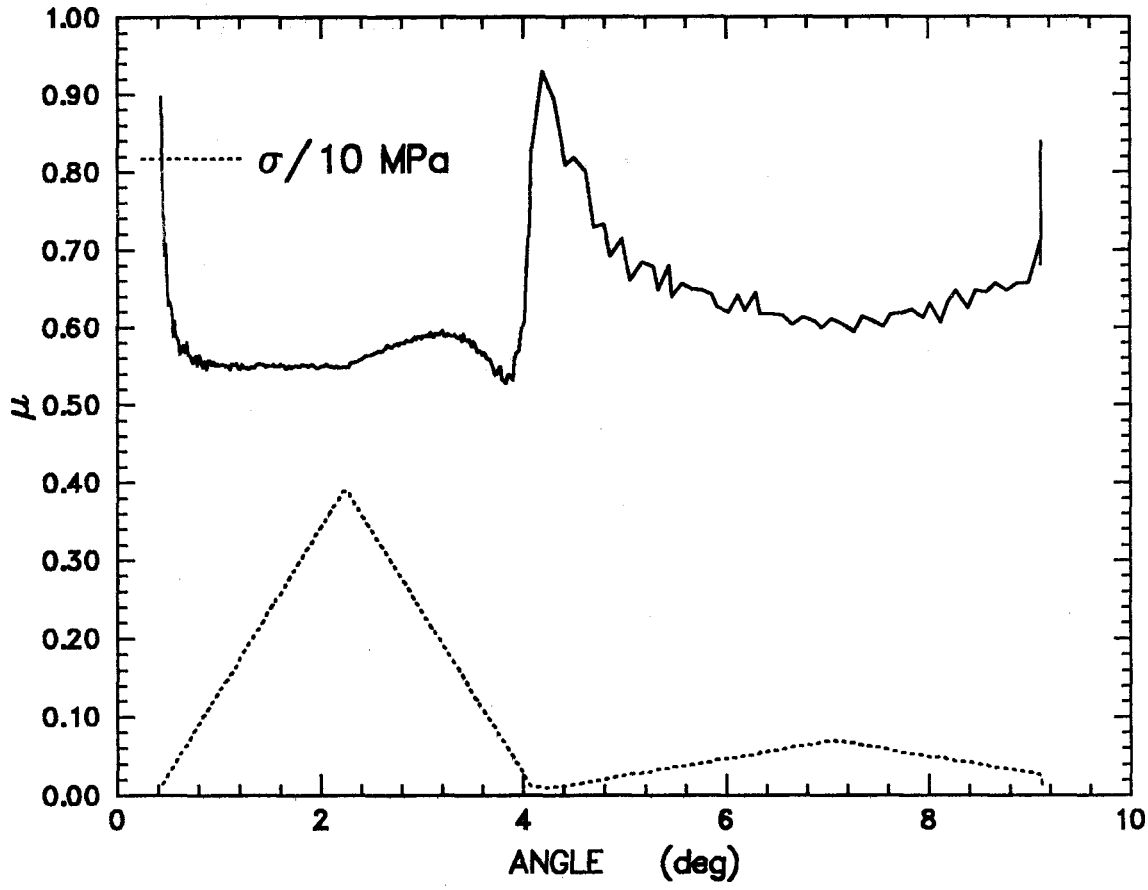

Figure 52: Experiment RFT045, normal stress-history test.

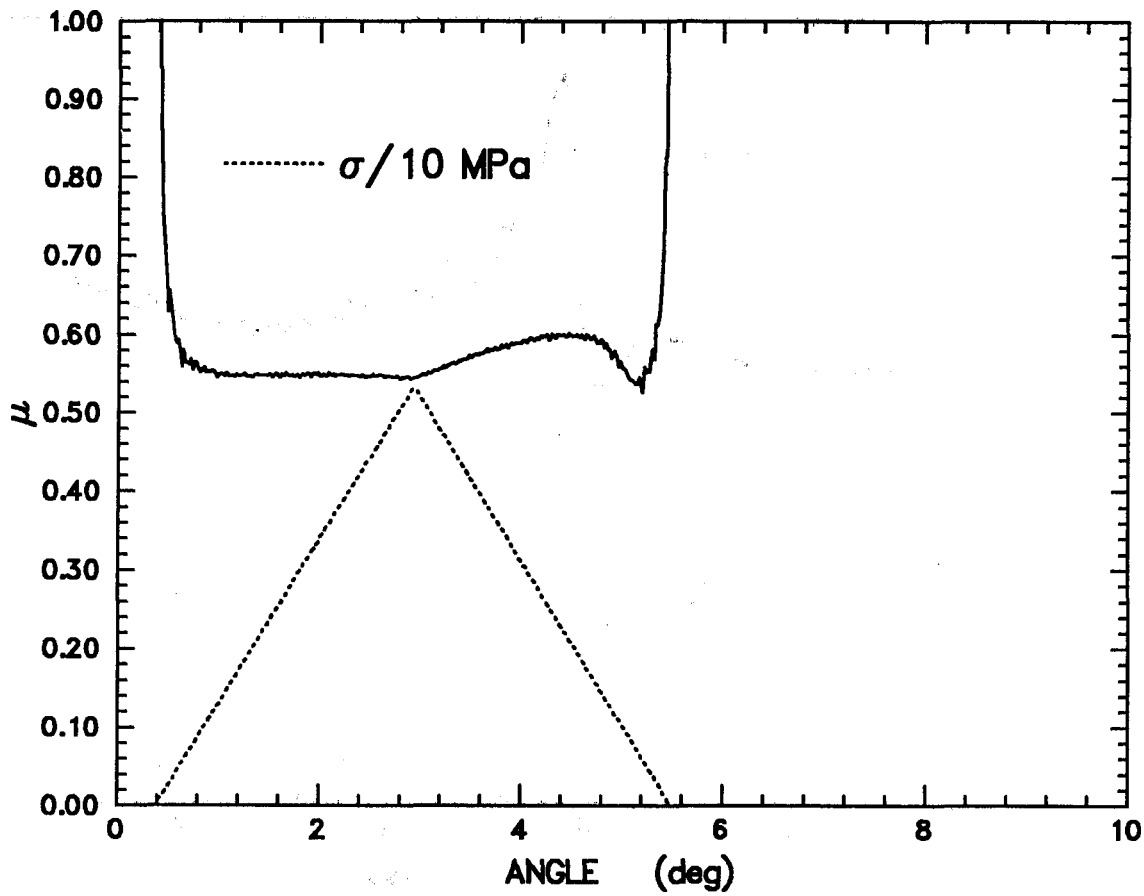

Figure 53: Experiment RFT046, normal stress-history test.

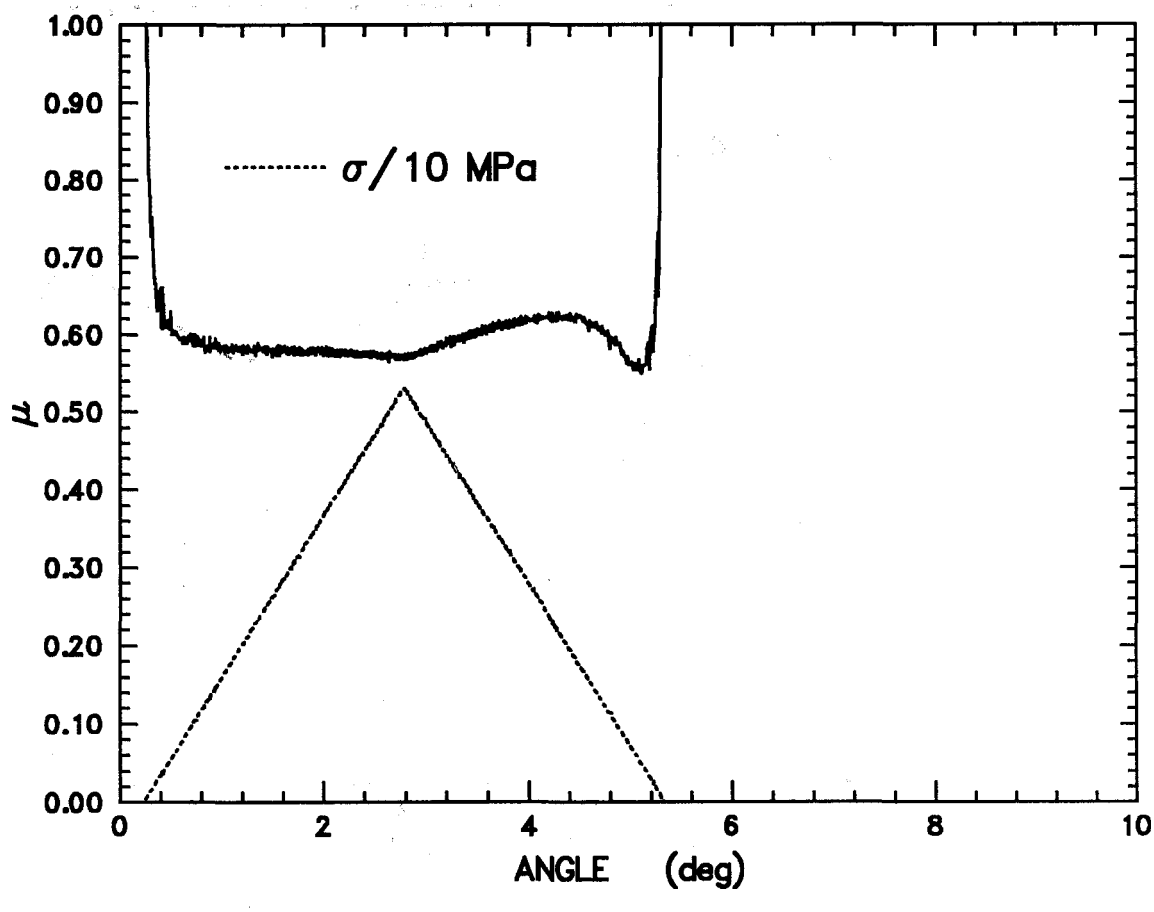

Figure 54: Experiment RFT047, normal stress-history test.

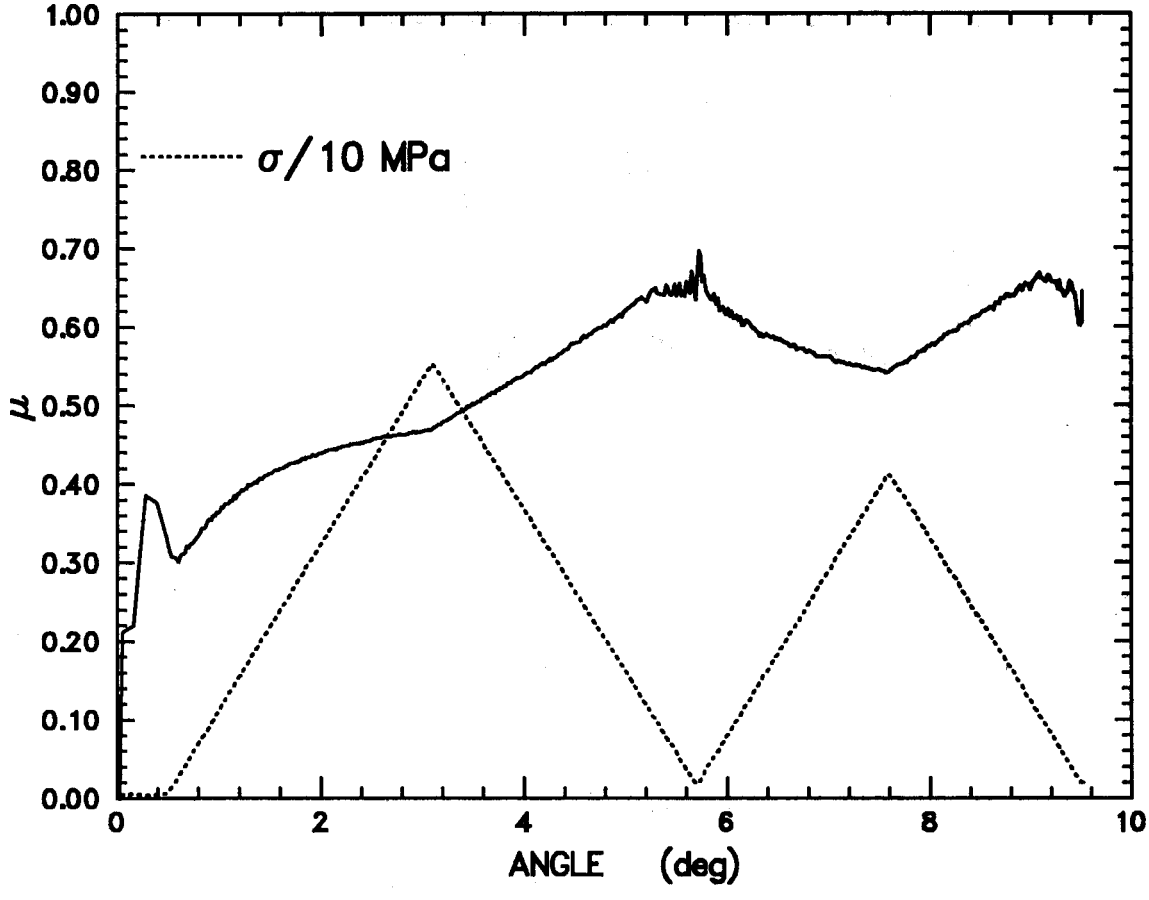

Figure 55: Experiment RFT048, normal stress-history test.

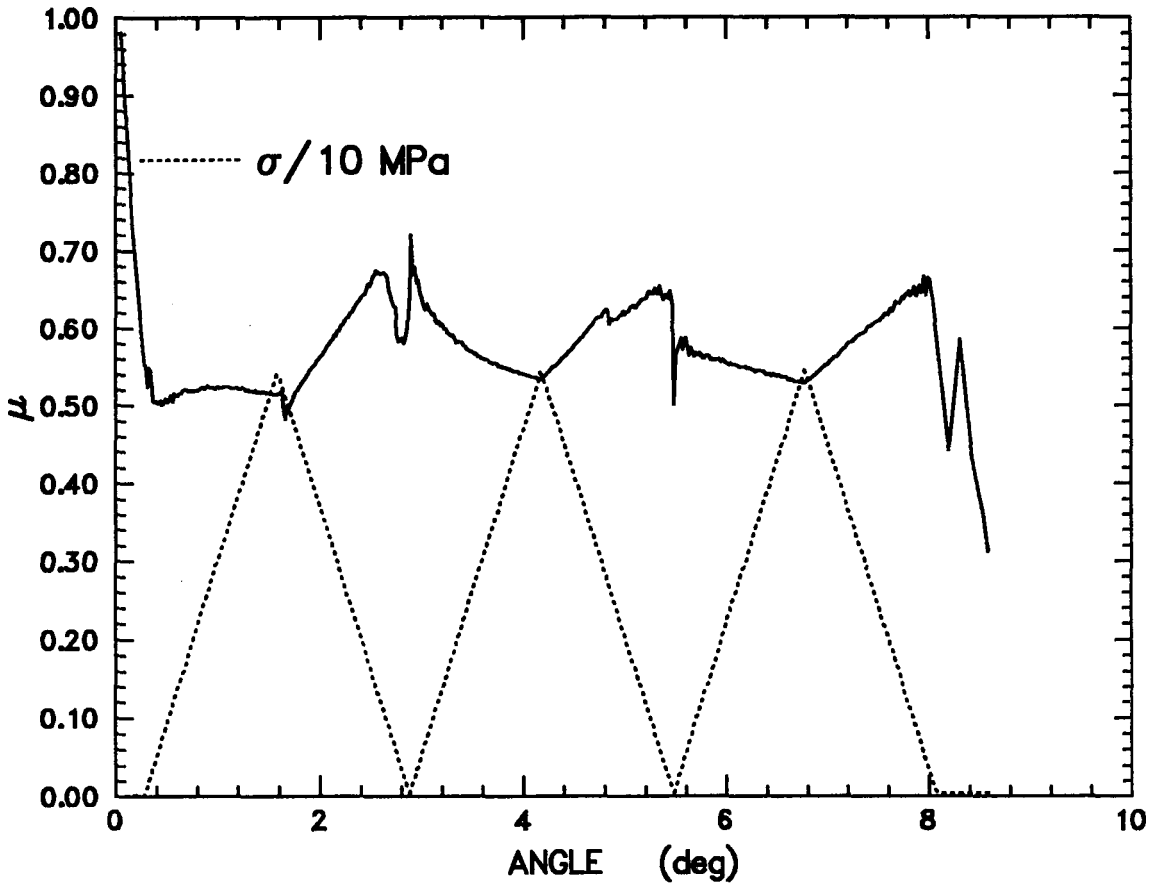

Figure 56: Experiment RFT049, normal stress-history test.

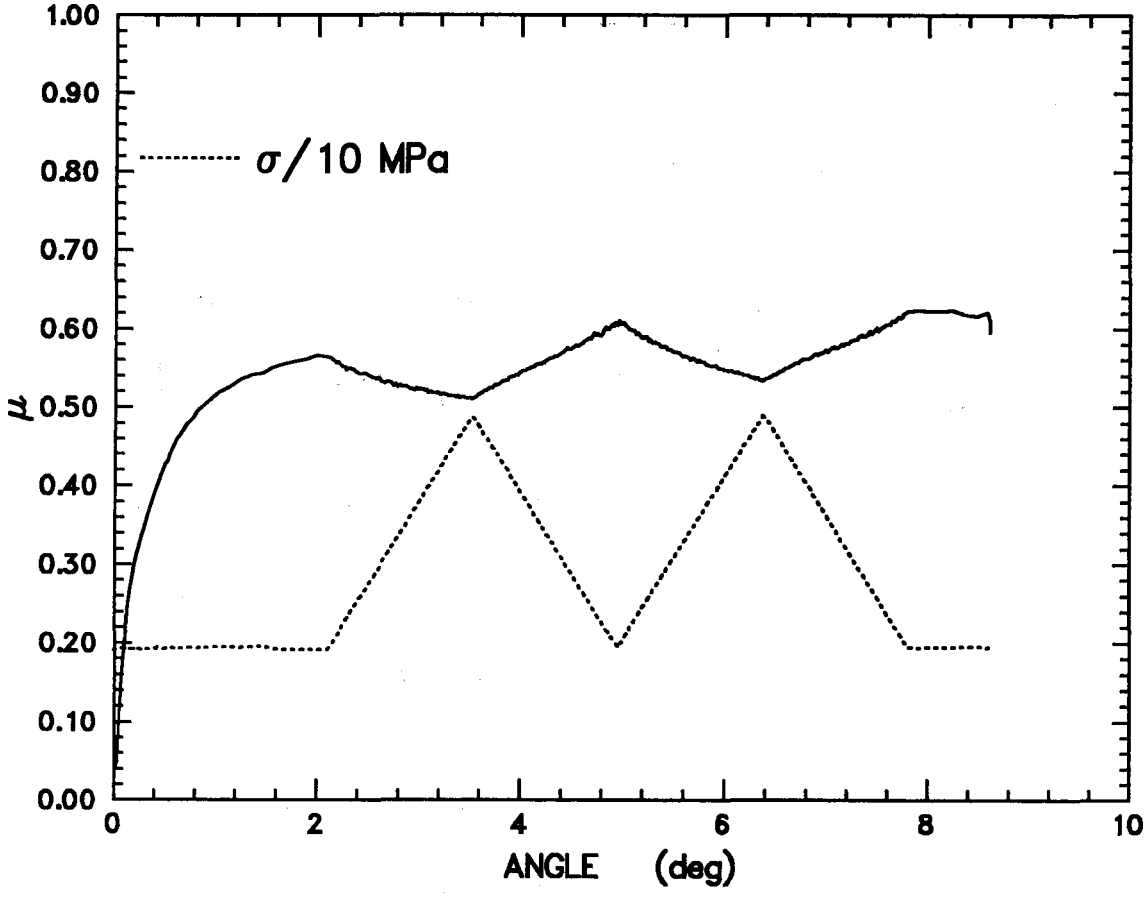

Figure 57: Experiment RFT050, normal stress-history test.

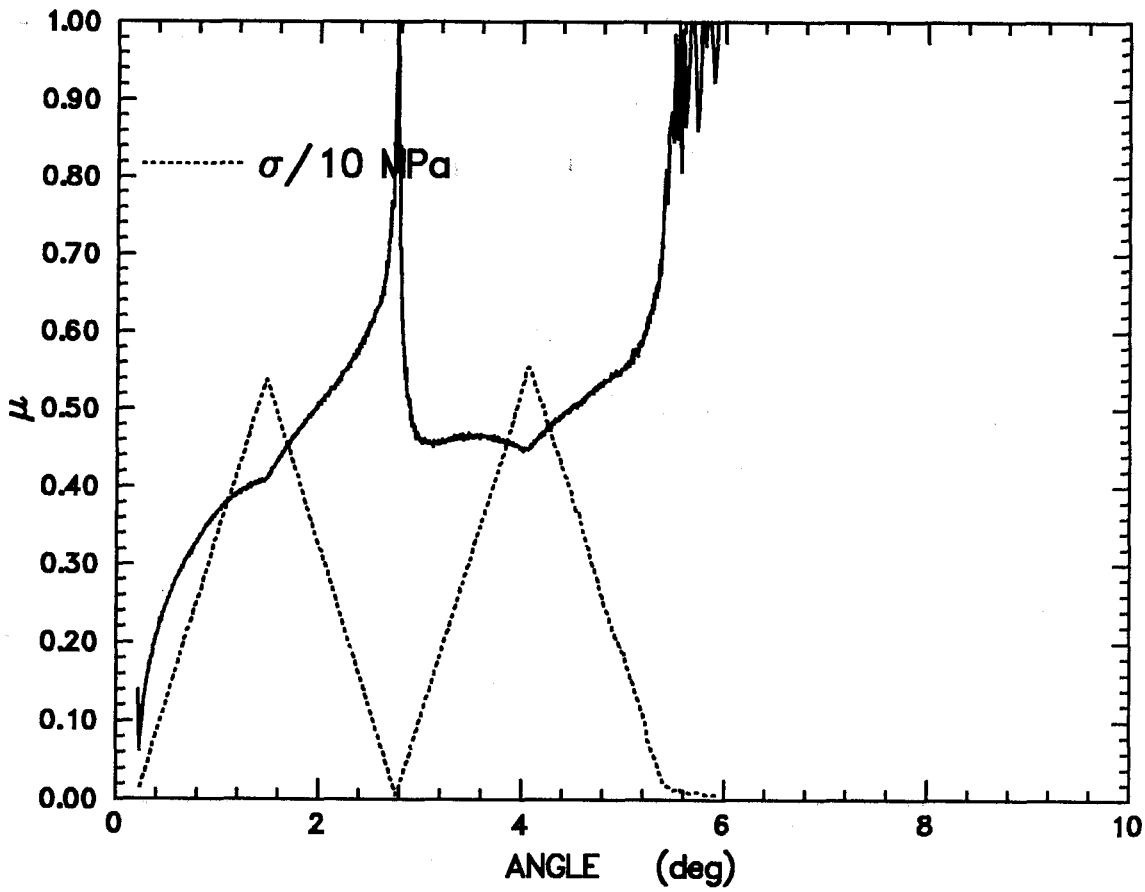

Figure 58: Experiment RFT051, normal stress-history test.

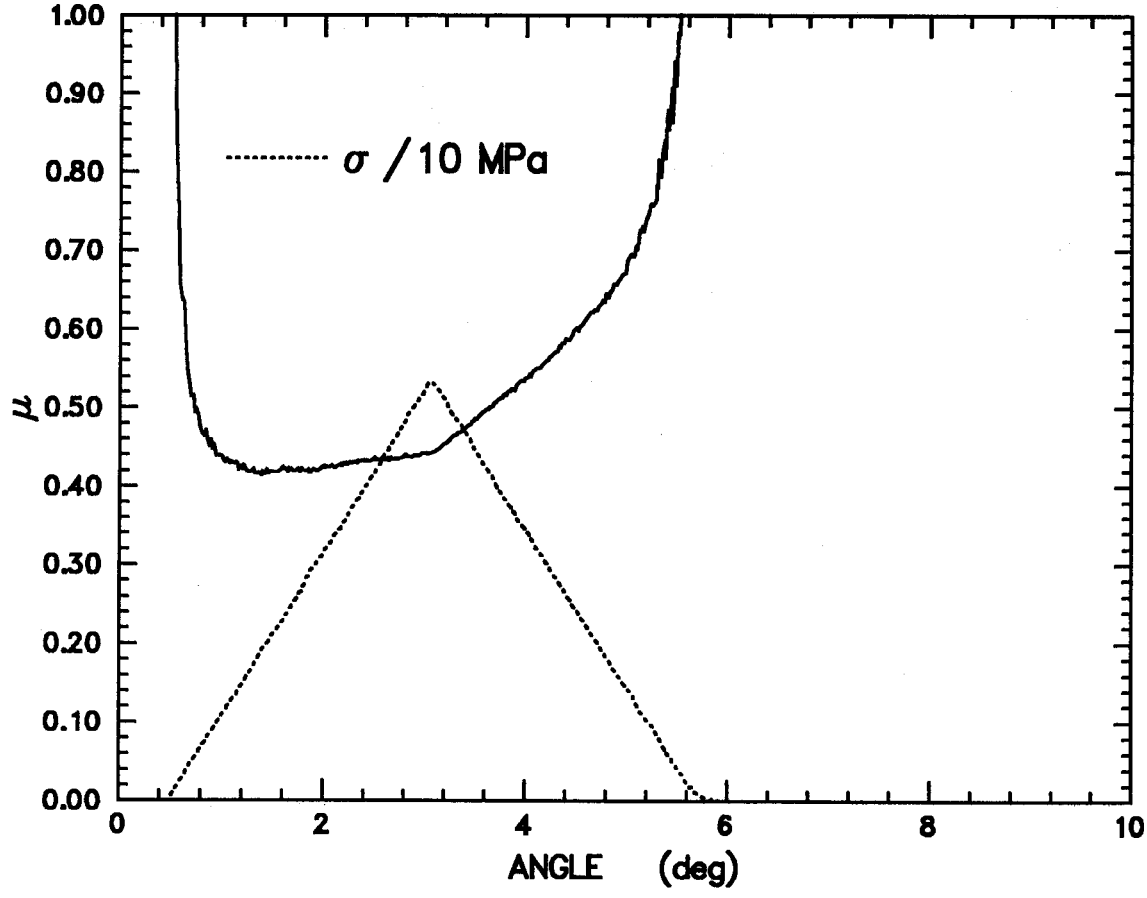

Figure 59: Experiment RFT052, normal stress-history test.

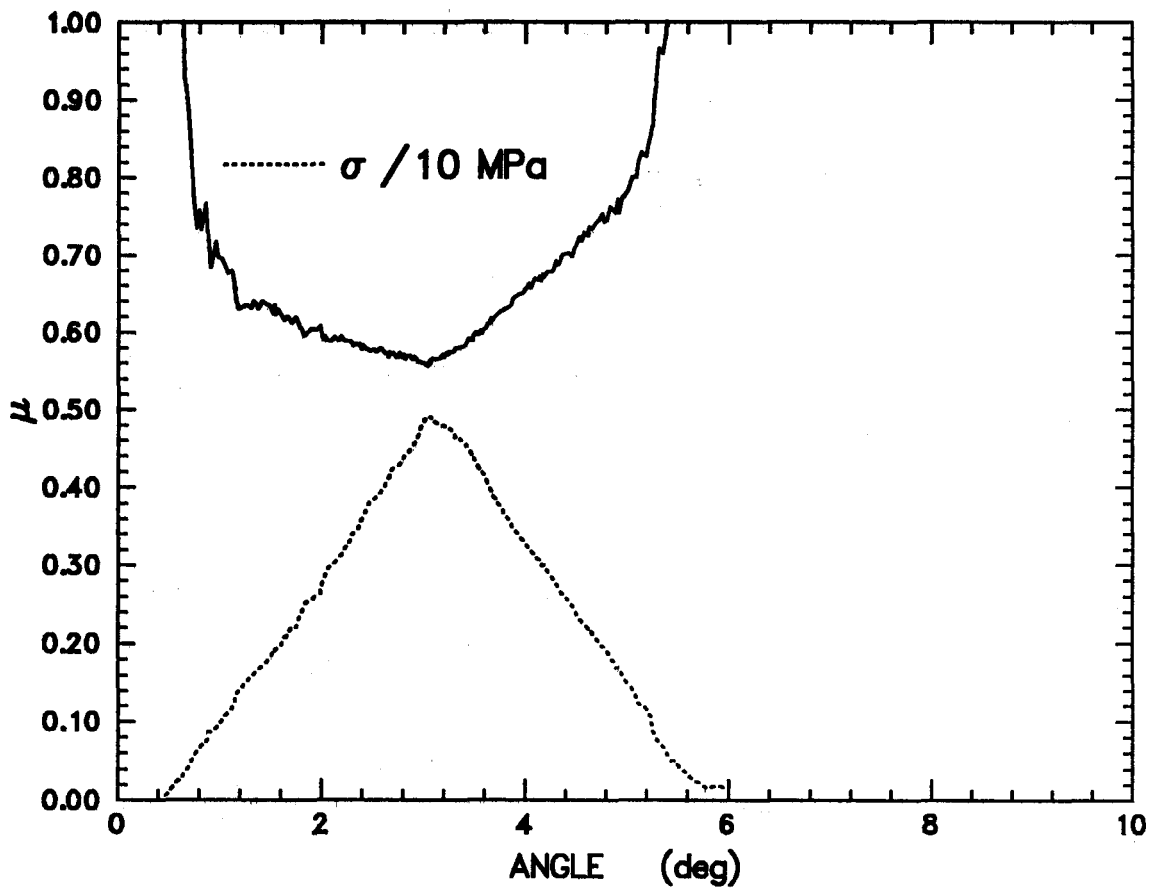

Figure 60: Experiment RFT053, normal stress-history test.

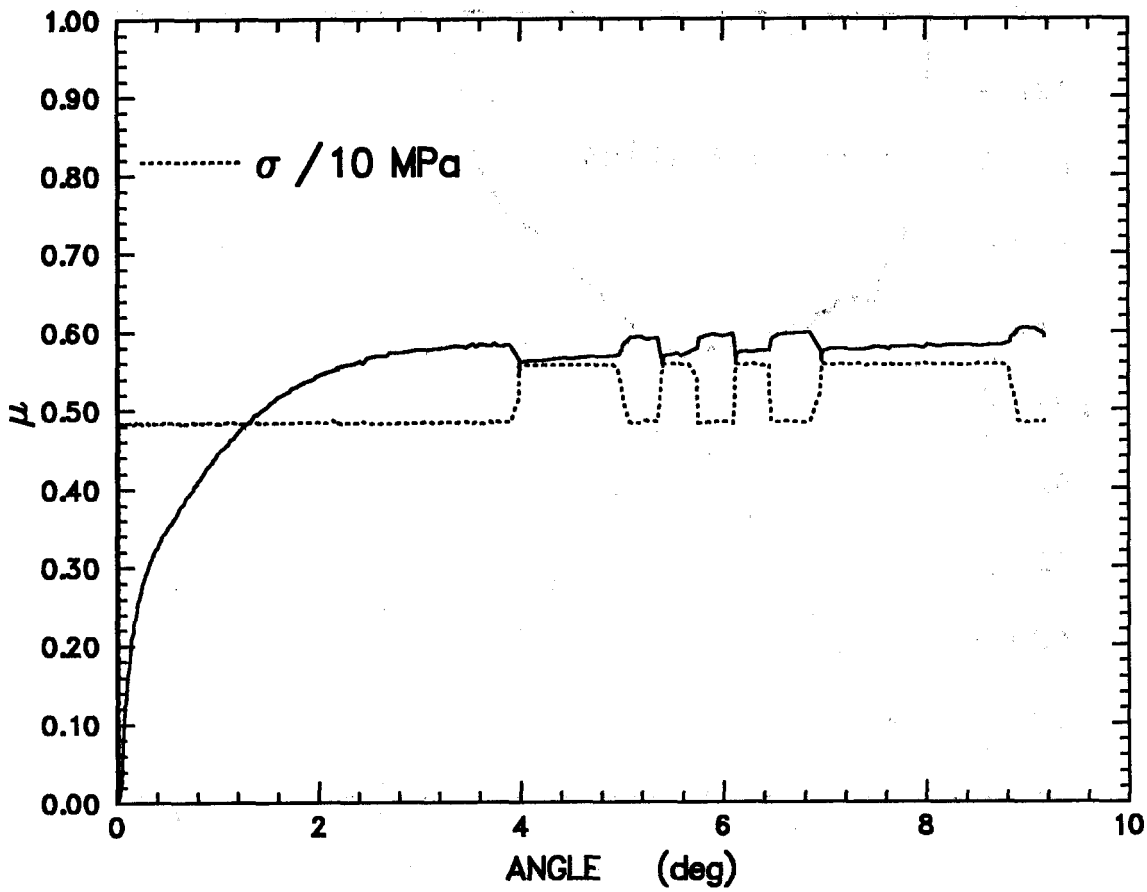

Figure 61: Experiment RFT055, normal stress-history test.

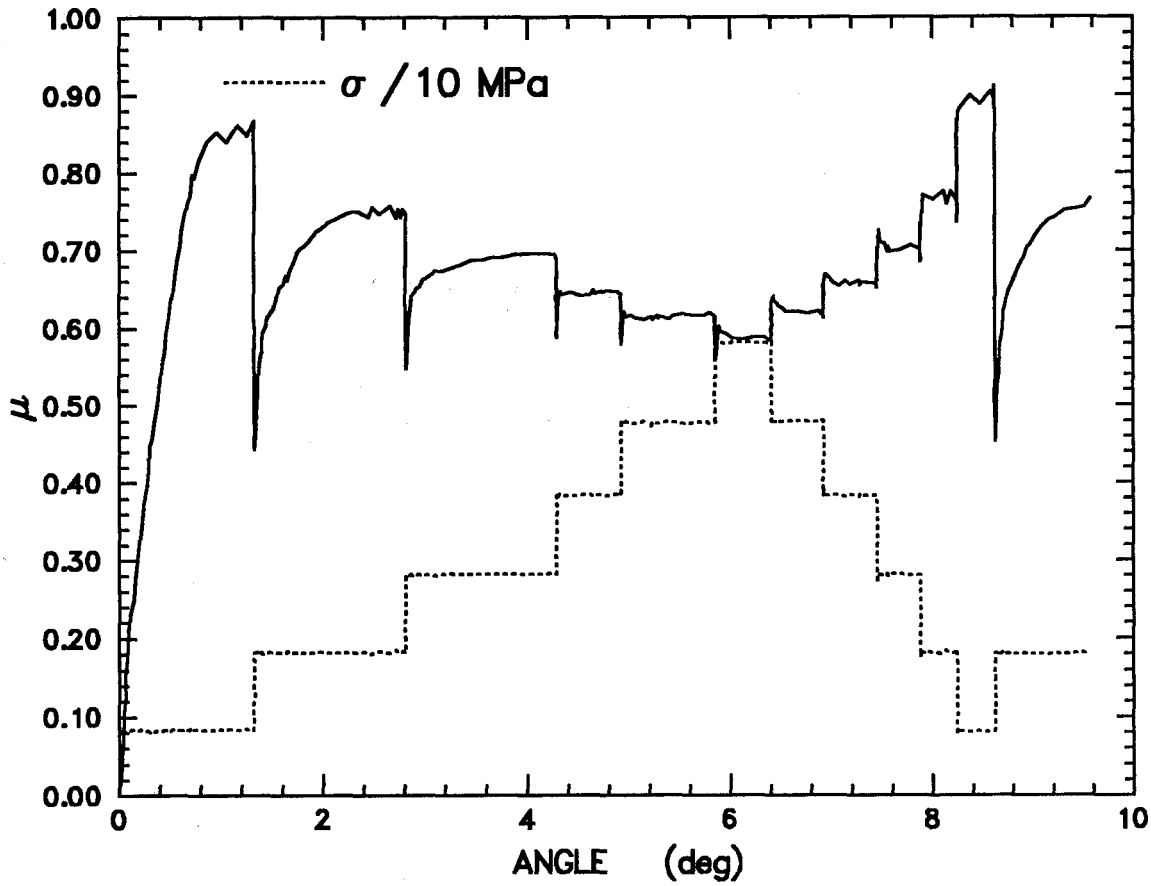

Figure 62: Experiment RFT056, normal stress-history test.

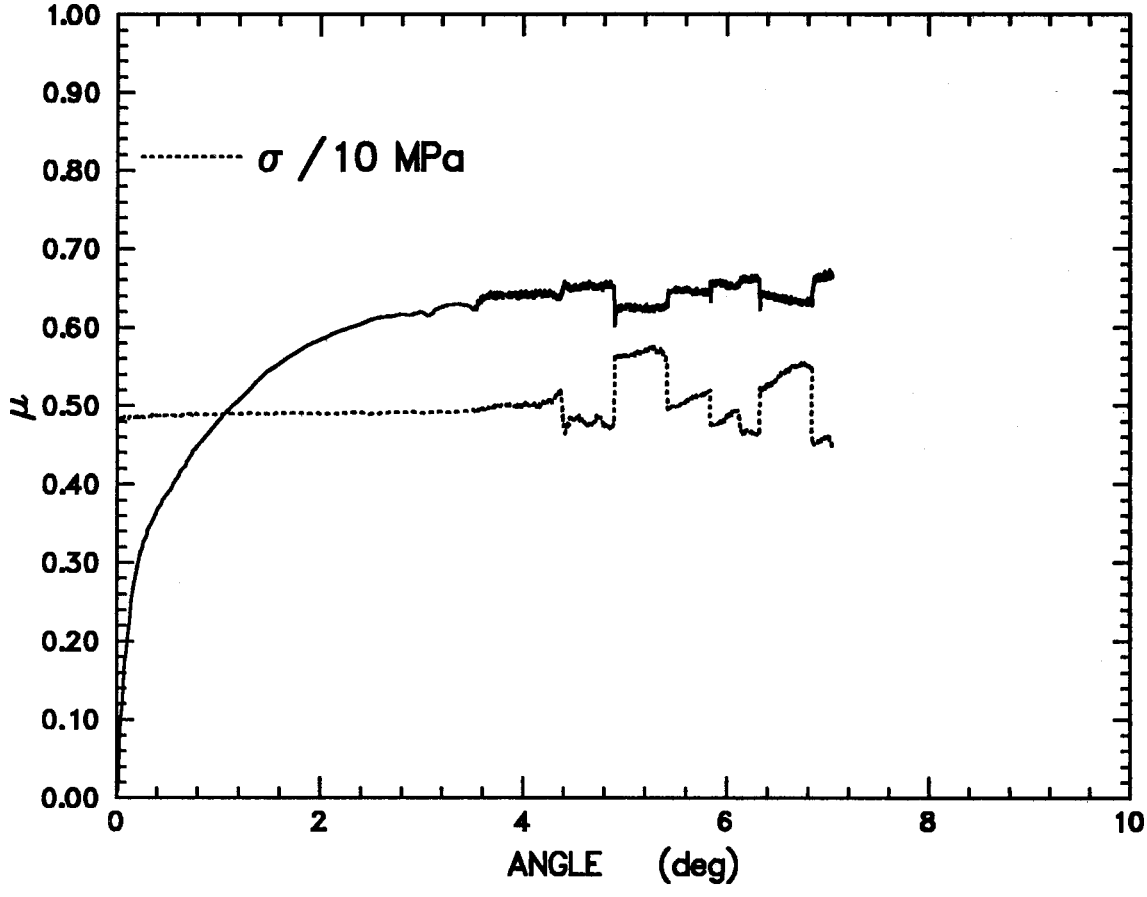

Figure 63: Experiment RFT057, normal stress-history test.

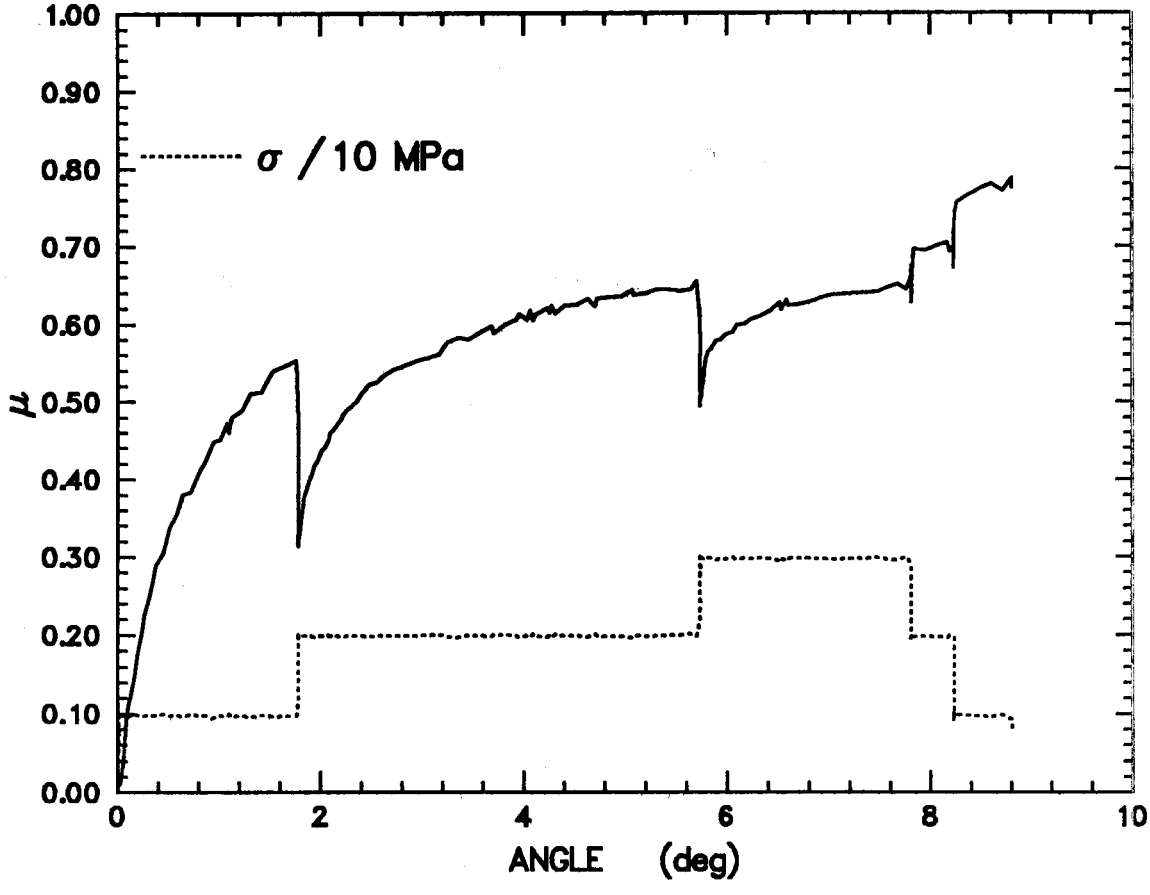

Figure 64: Experiment RFT060, normal stress-history test.

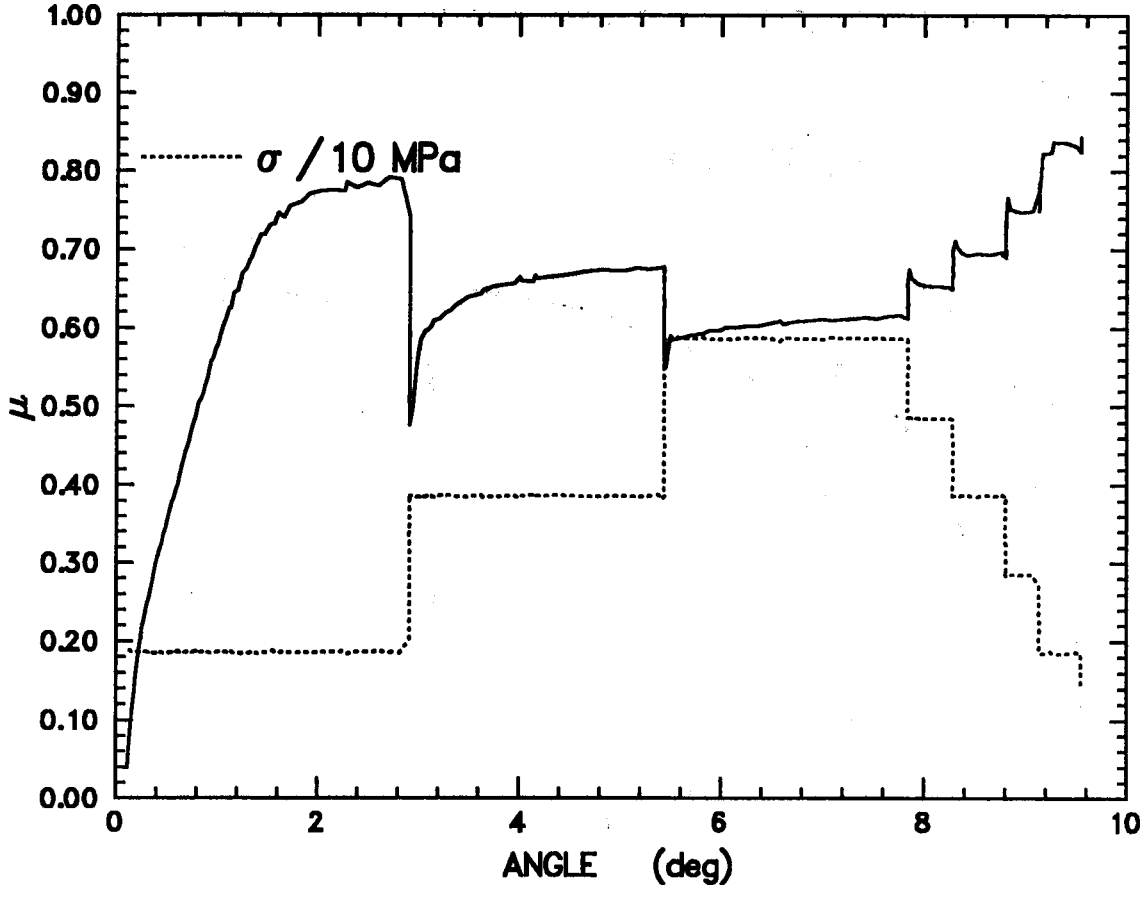

Figure 65: Experiment RFT061, normal stress-history test.

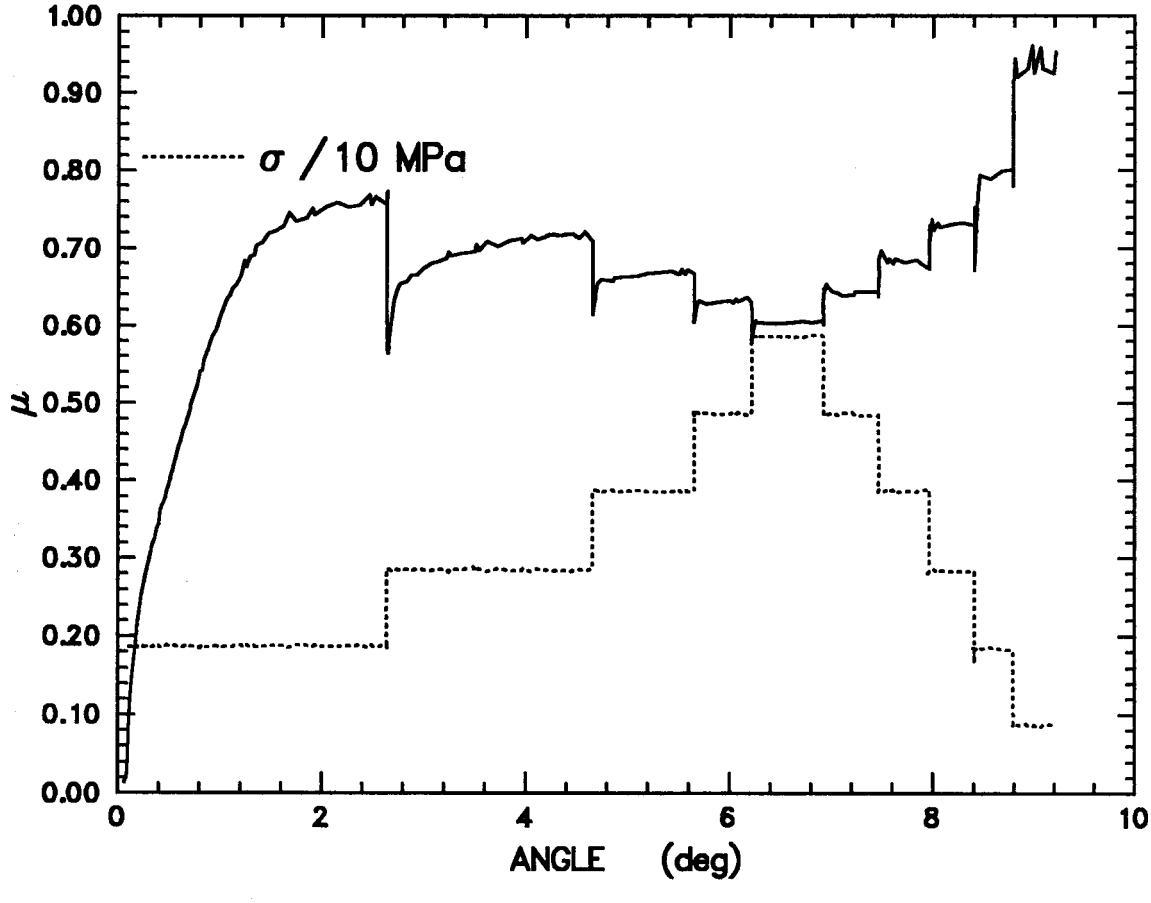

Figure 66: Experiment RFT062, normal stress-history test.

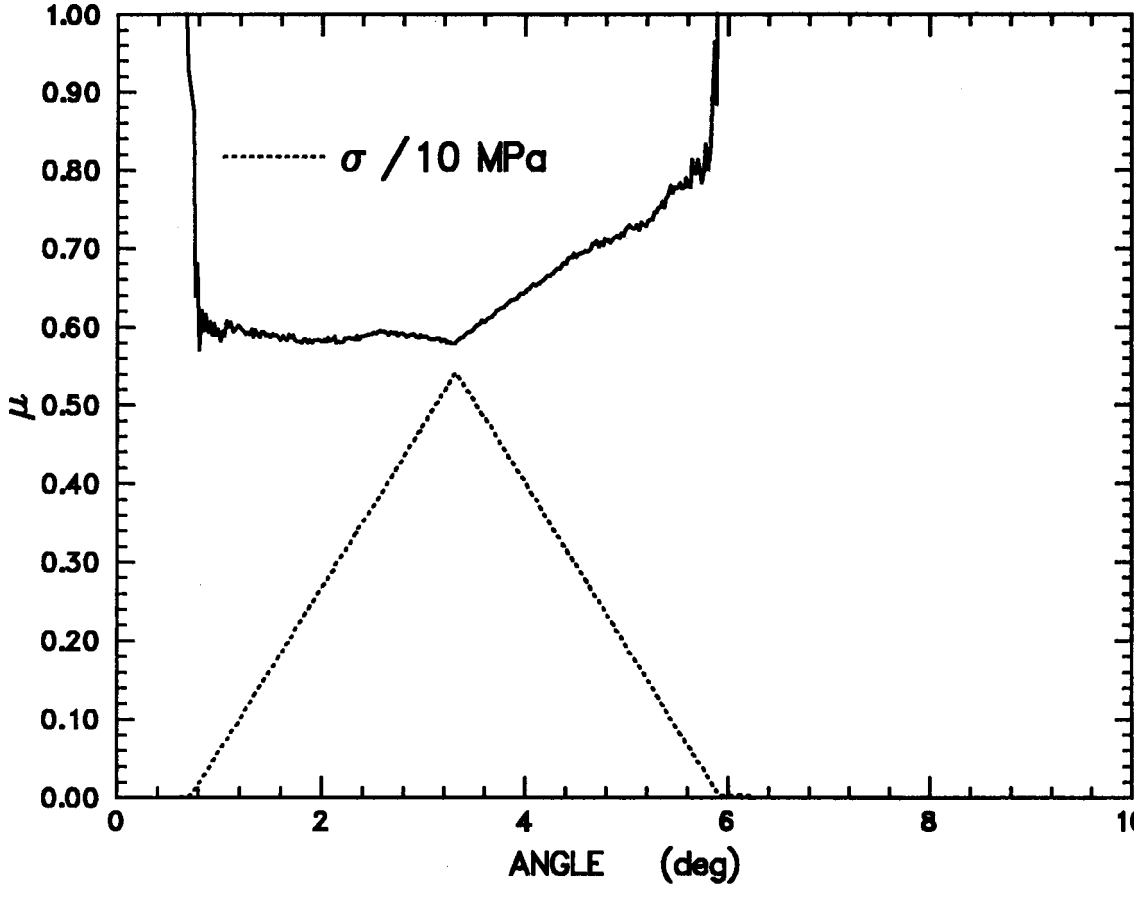

Figure 67: Experiment RFT063, normal stress-history test.

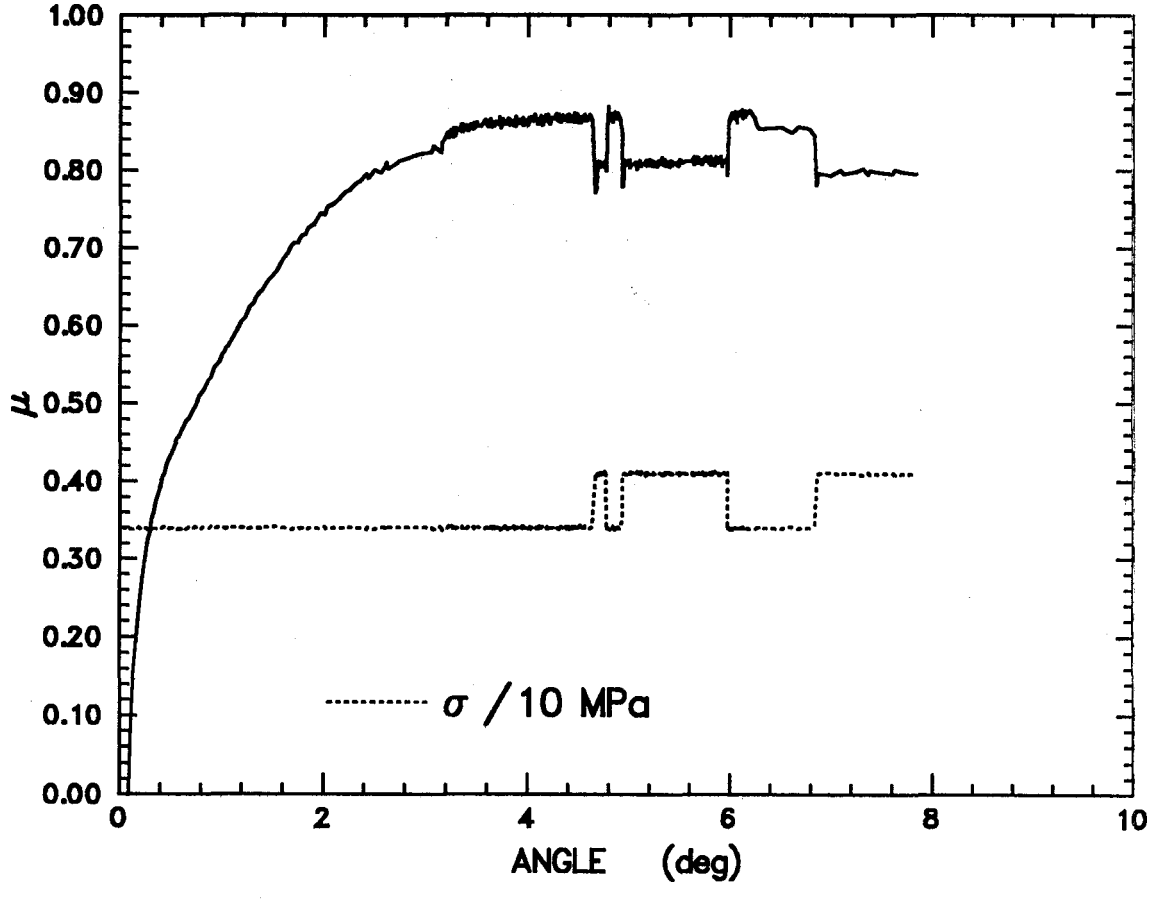

Figure 68: Experiment RFT064, normal stress-history test.

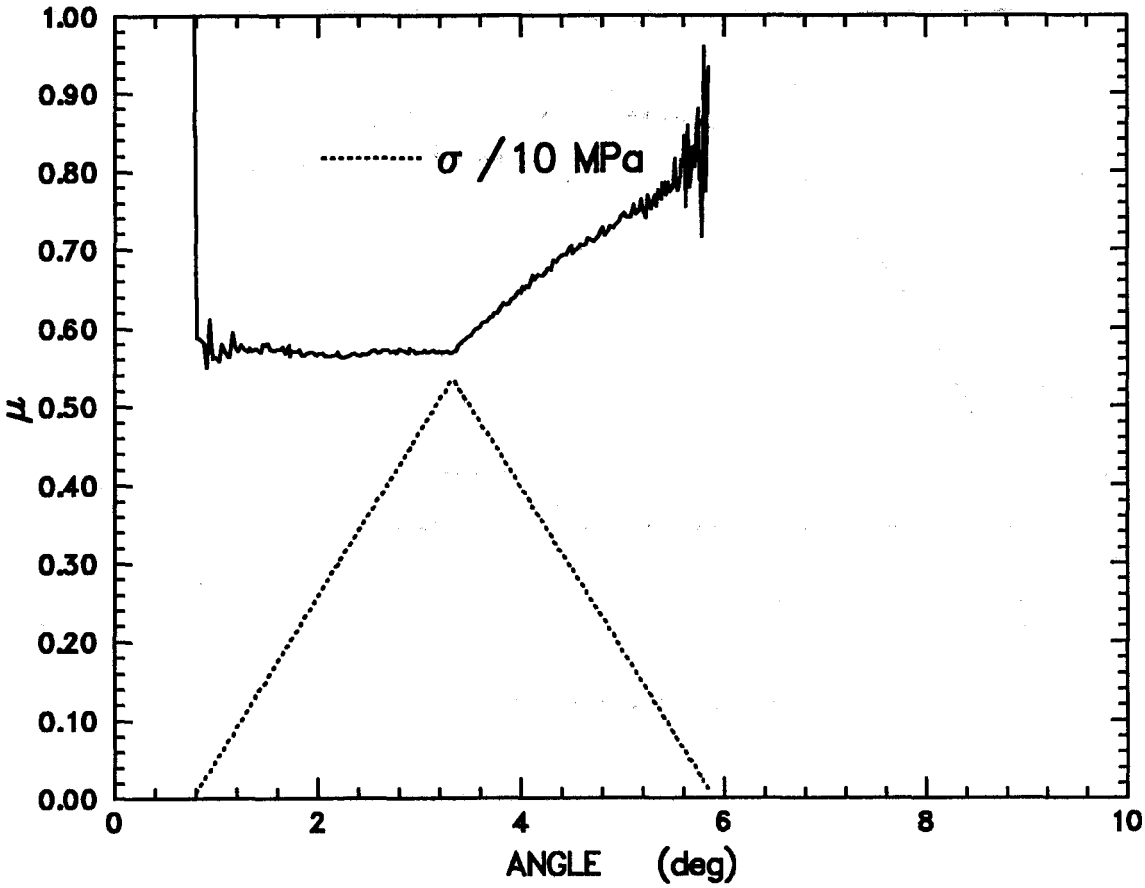

Figure 69: Experiment RFT065, normal stress-history test.

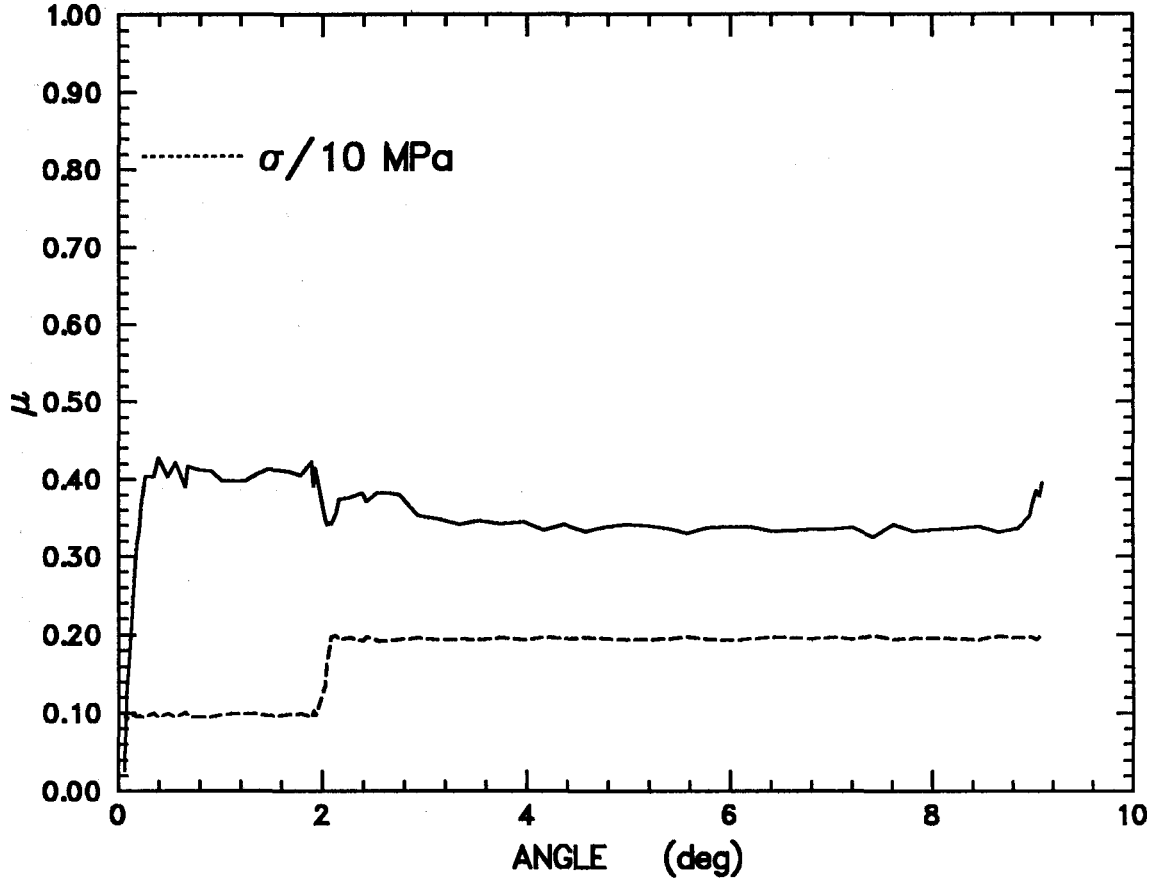

Figure 70: Experiment RFT066, normal stress-history test.

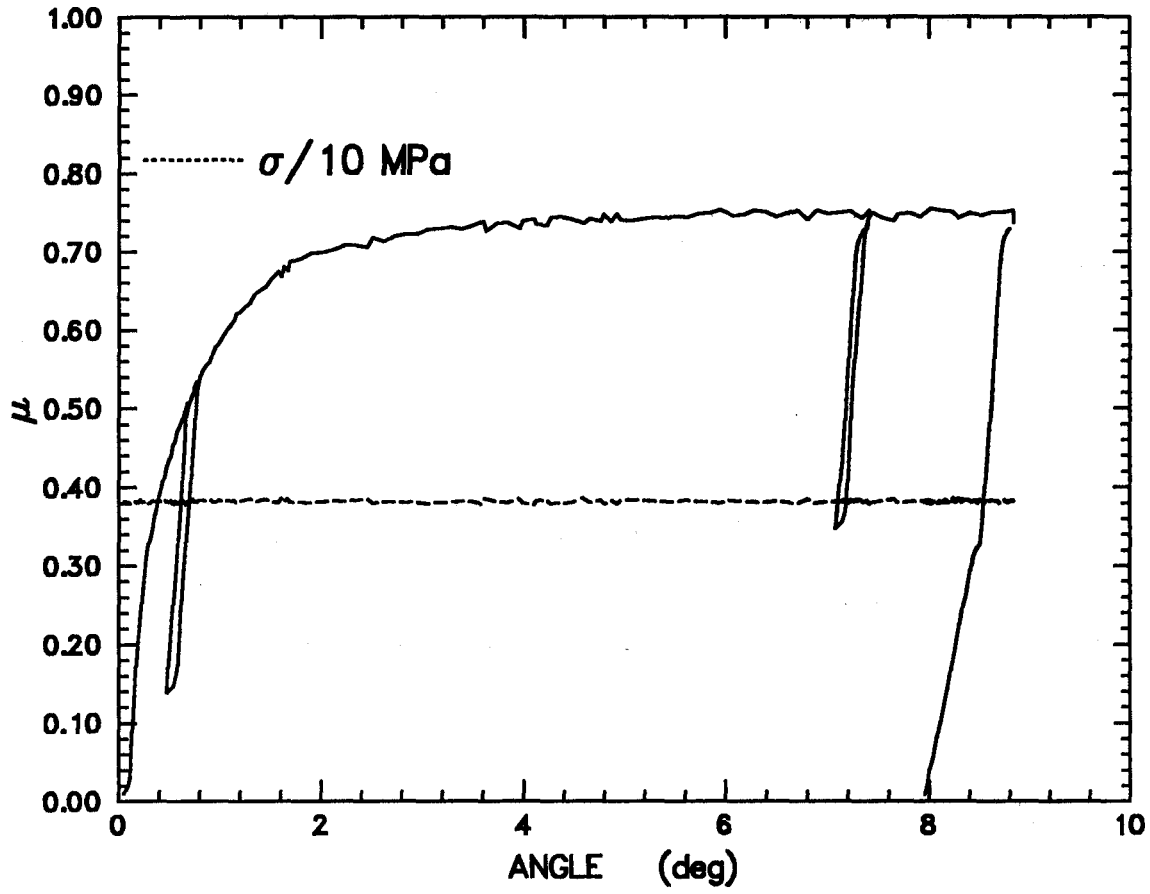

Figure 71: Experiment RFT071, normal stress-history test.

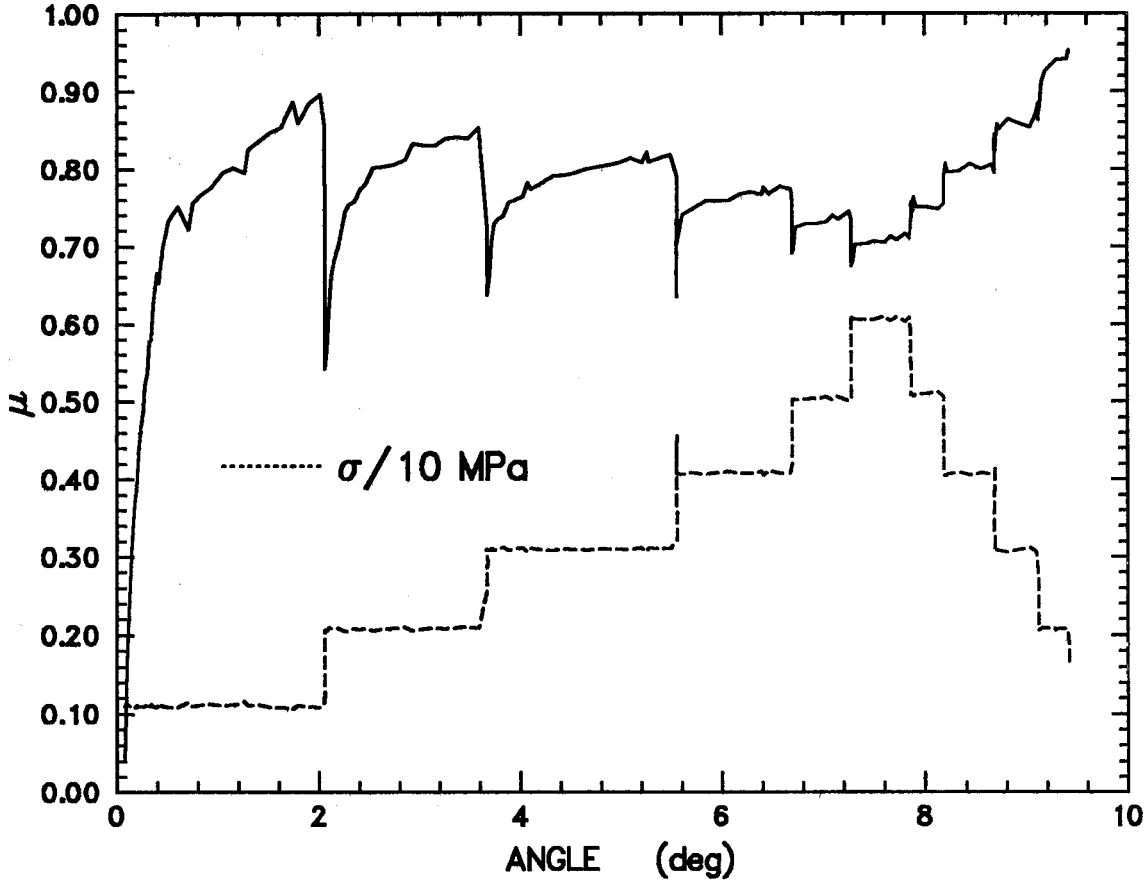

Figure 72: Experiment RFT073, normal stress-history test.

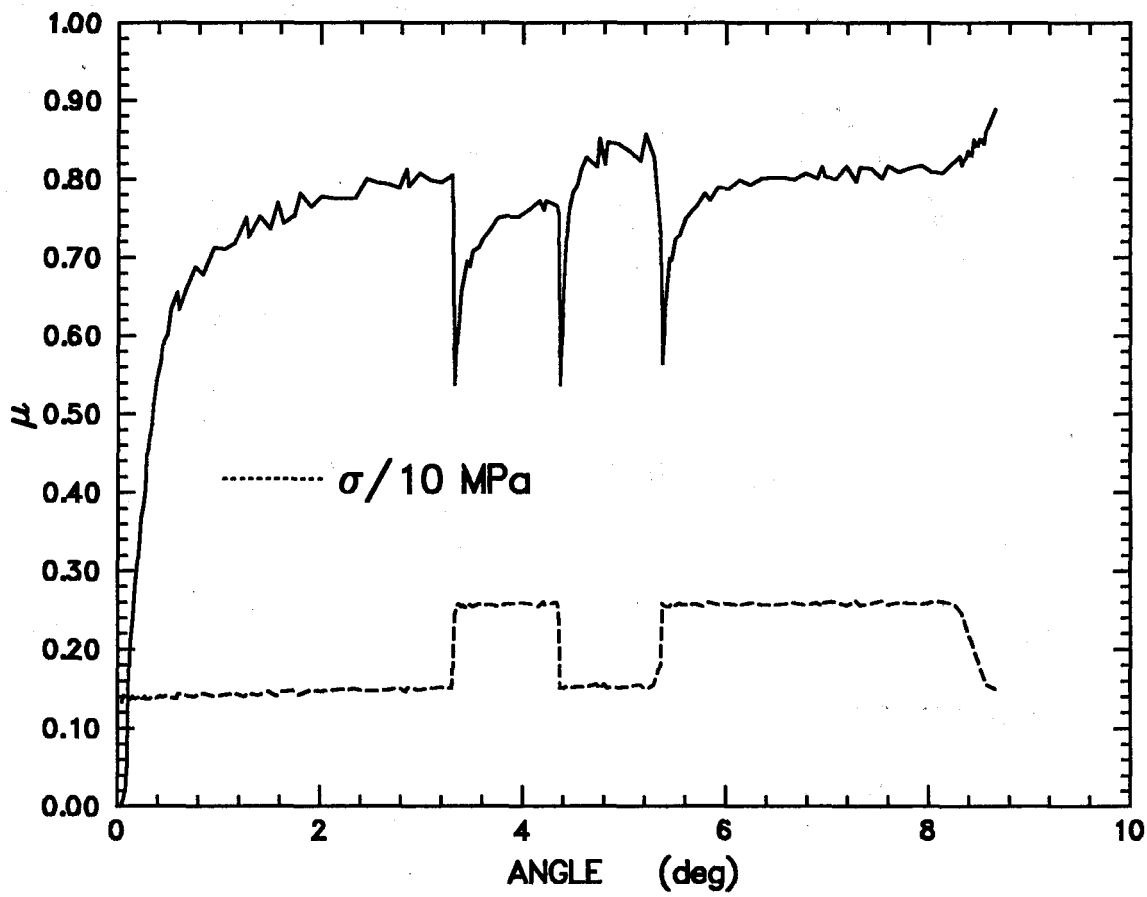

Figure 73: Experiment RFT074, normal stress-history test.

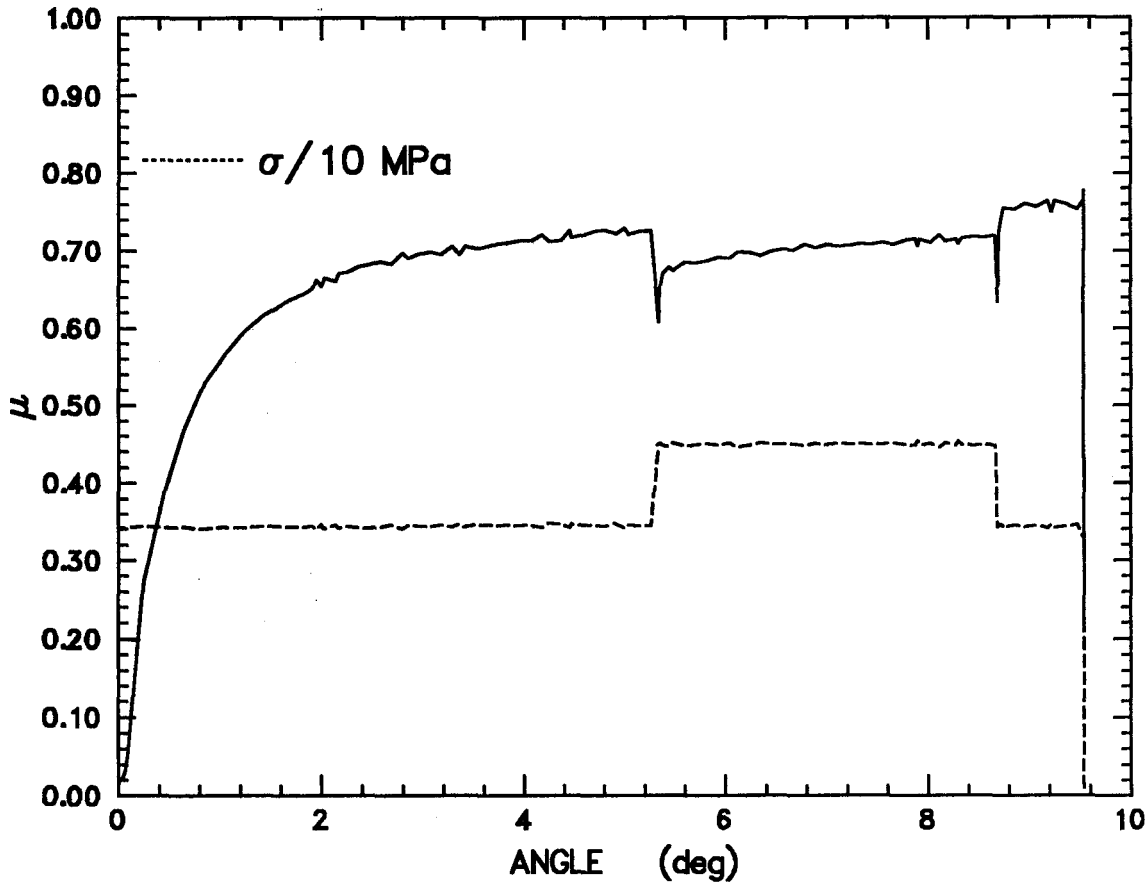

Figure 74: Experiment RFT075, normal stress-history test.

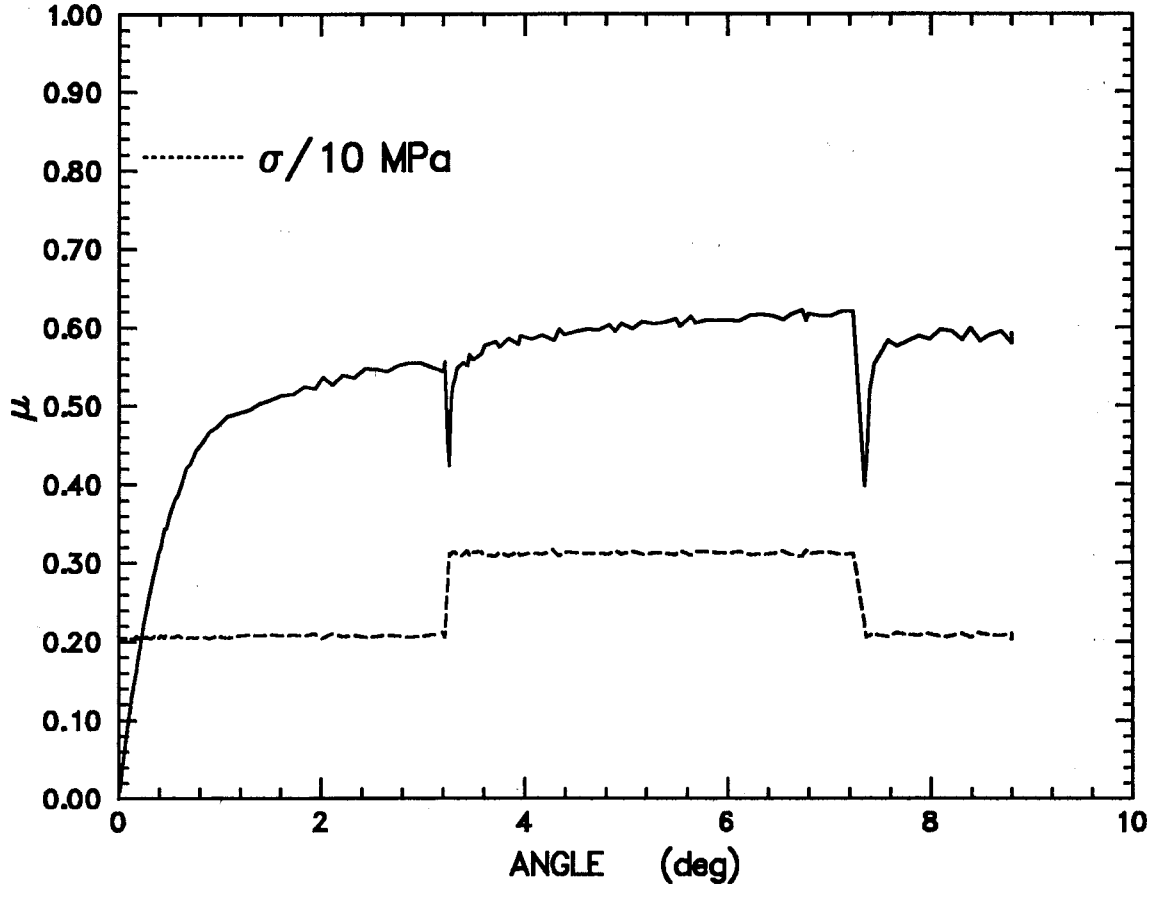

Figure 75: Experiment RFT076, normal stress-history test.

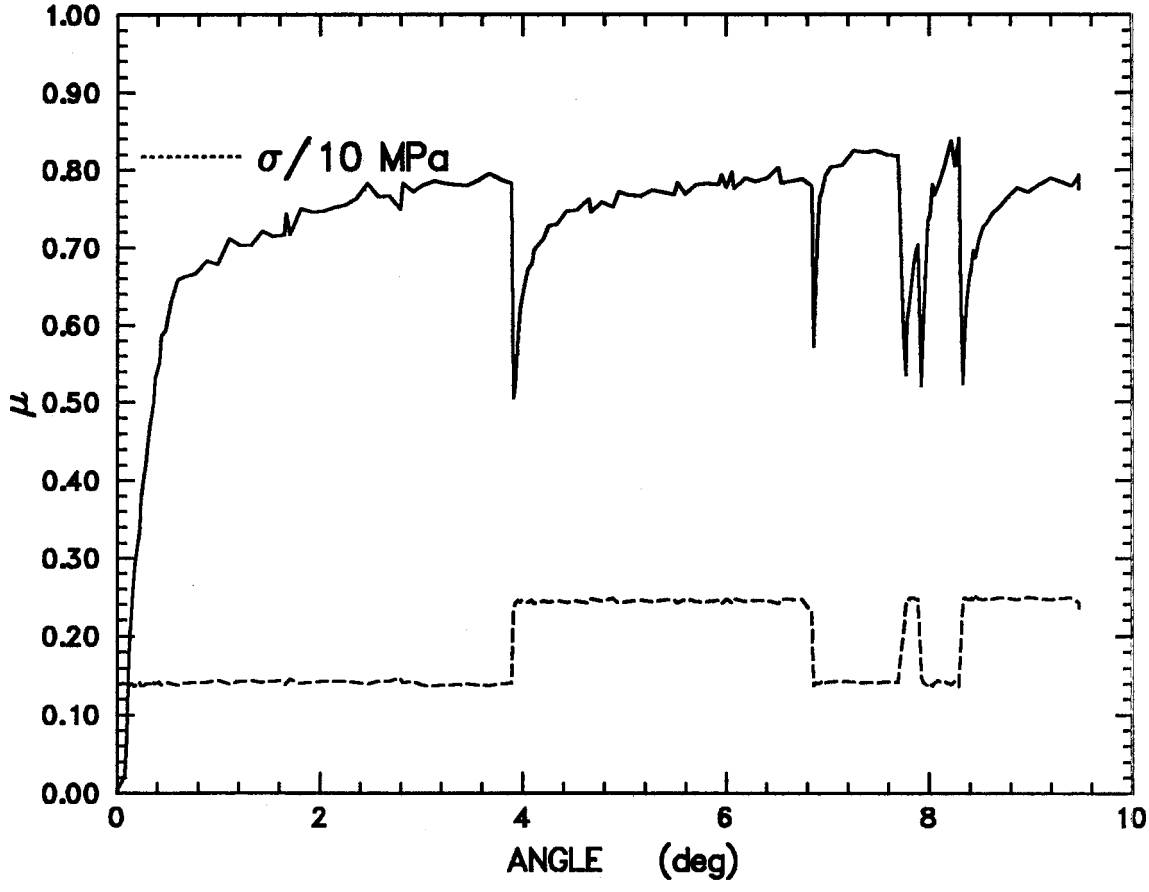

Figure 76: Experiment RFT077, normal stress-history test.

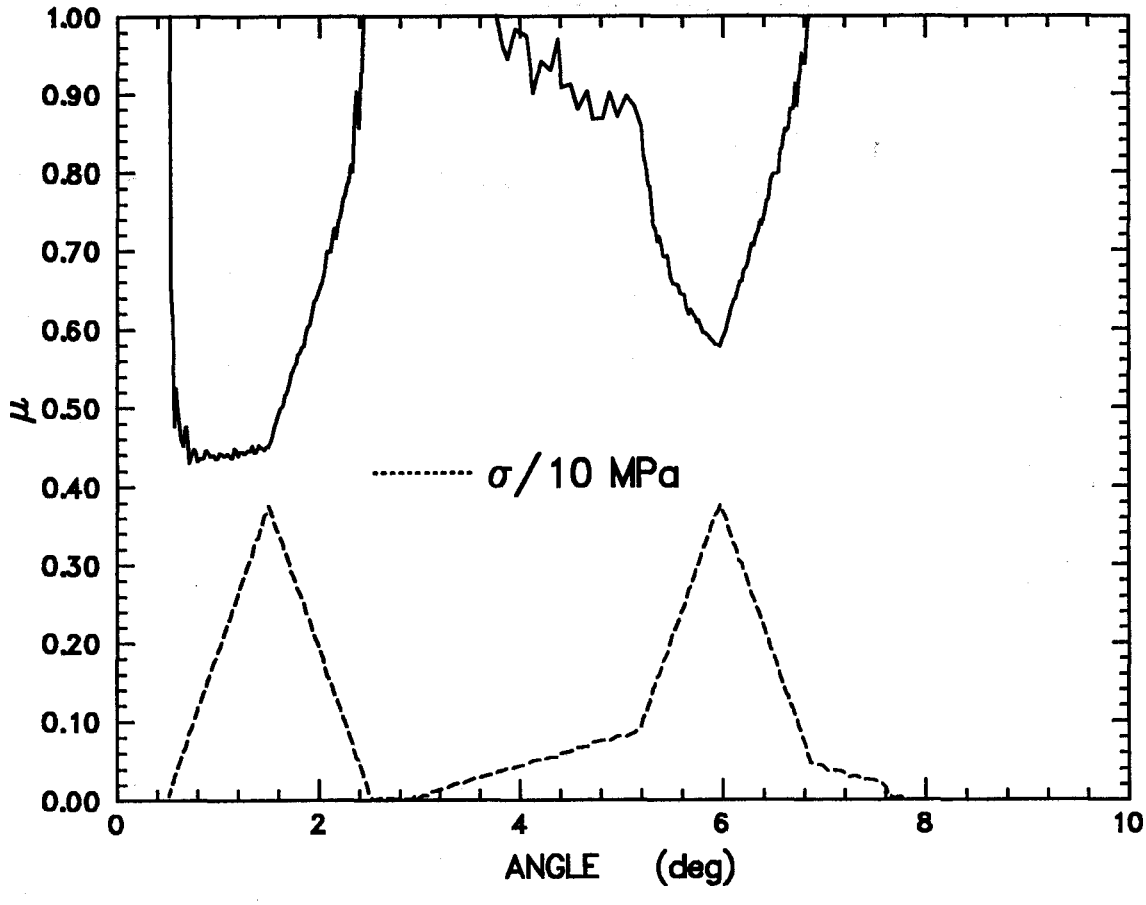

Figure 77: Experiment RFT078, normal stress-history test.

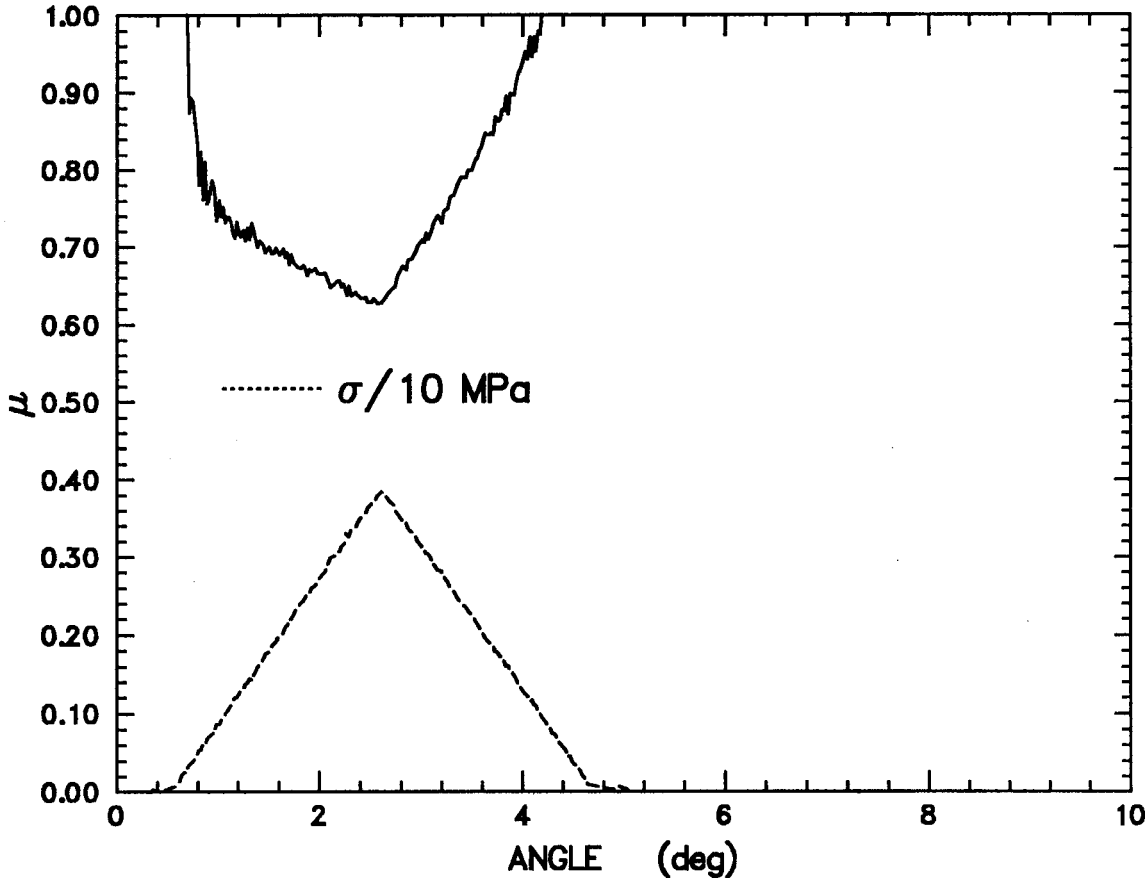

Figure 78: Experiment RFT079, normal stress-history test.

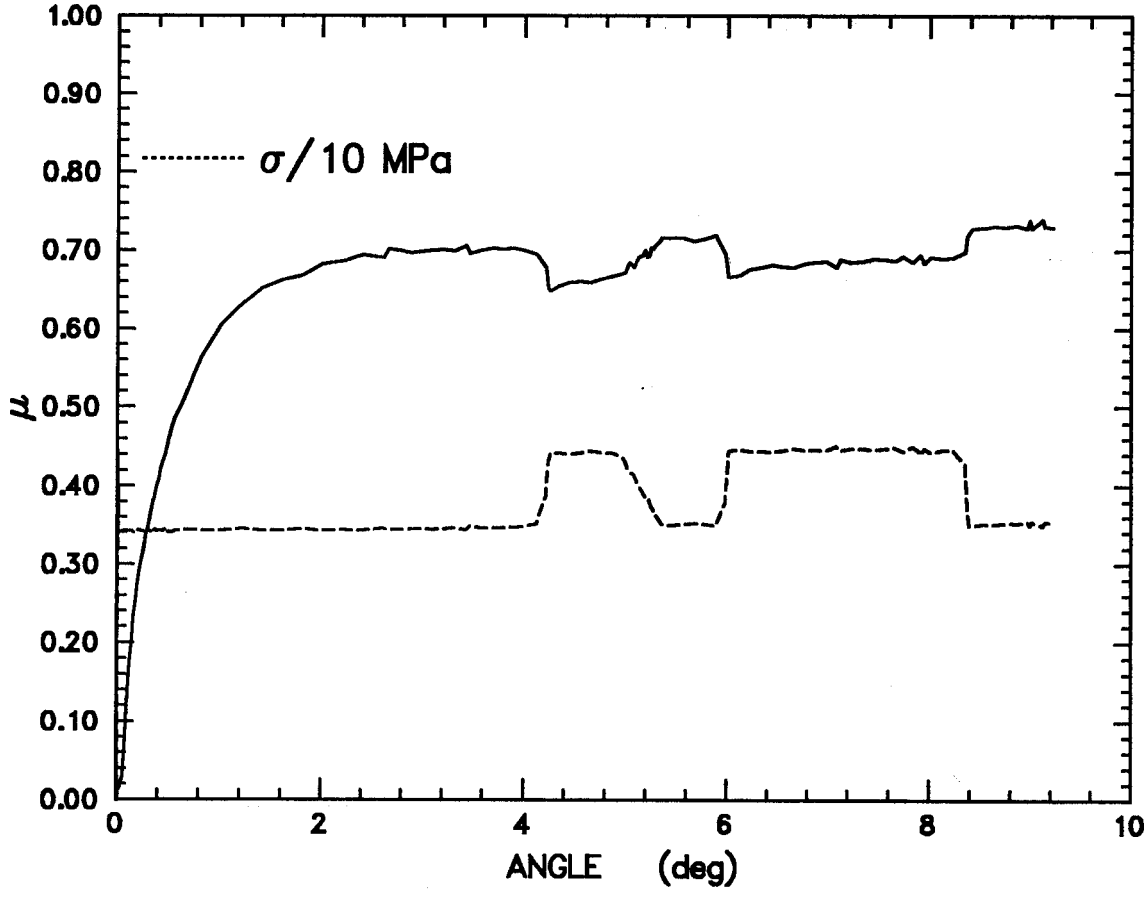

Figure 79: Experiment RFT080, normal stress-history test.

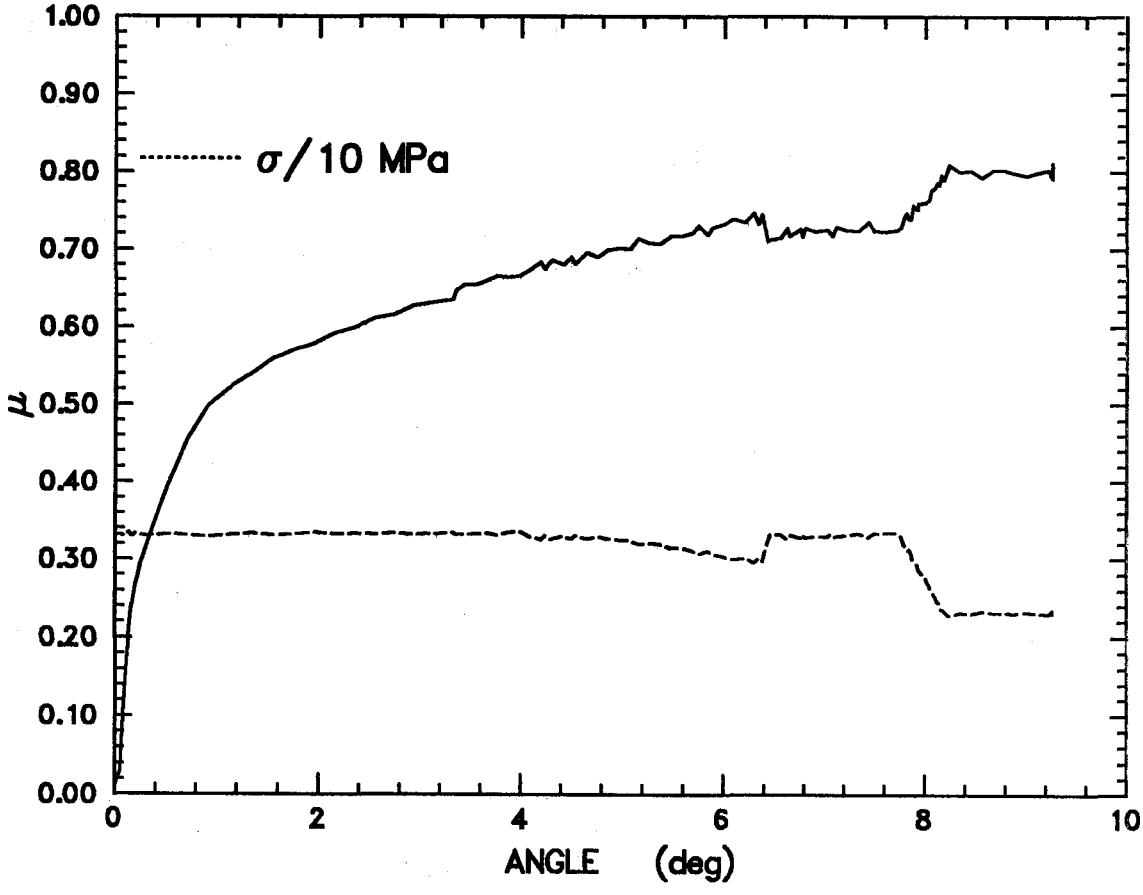

Figure 80: Experiment RFT081, normal stress-history test.

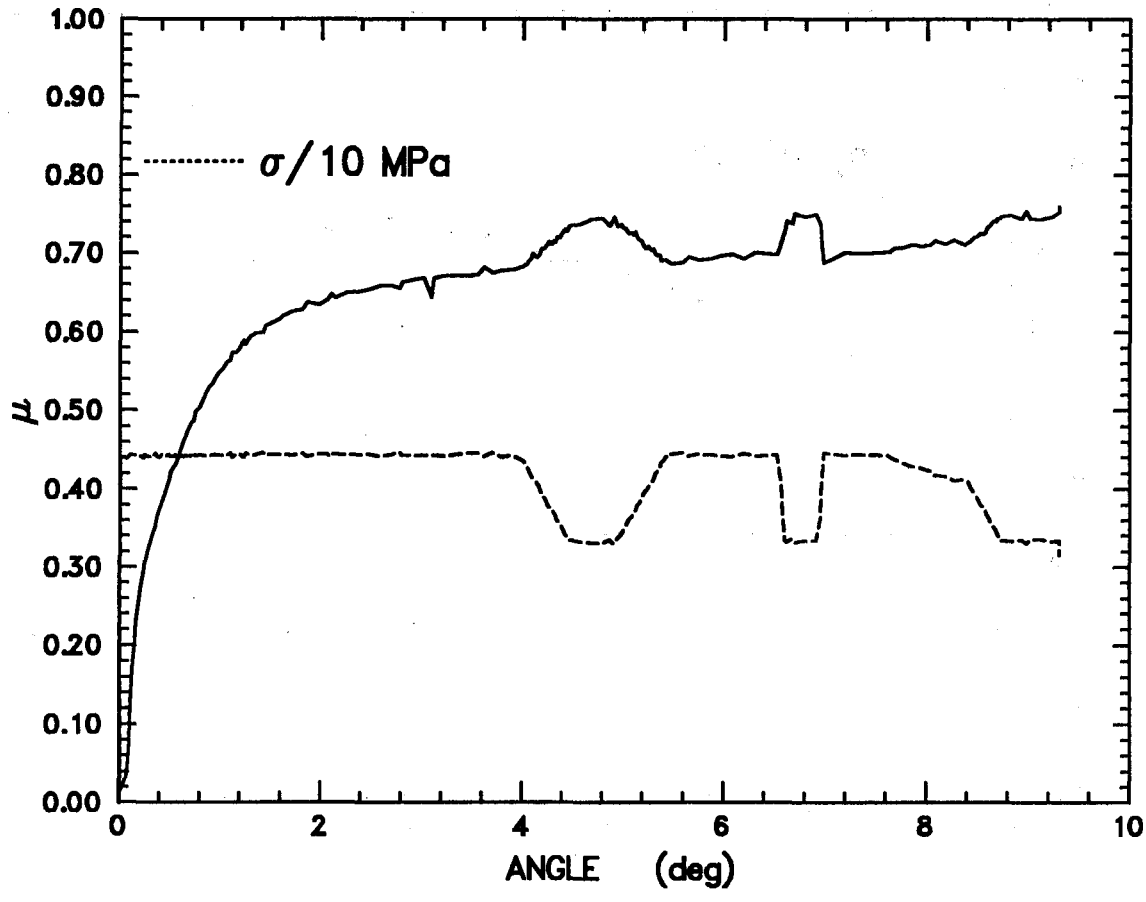

Figure 81: Experiment RFT082, normal stress-history test.

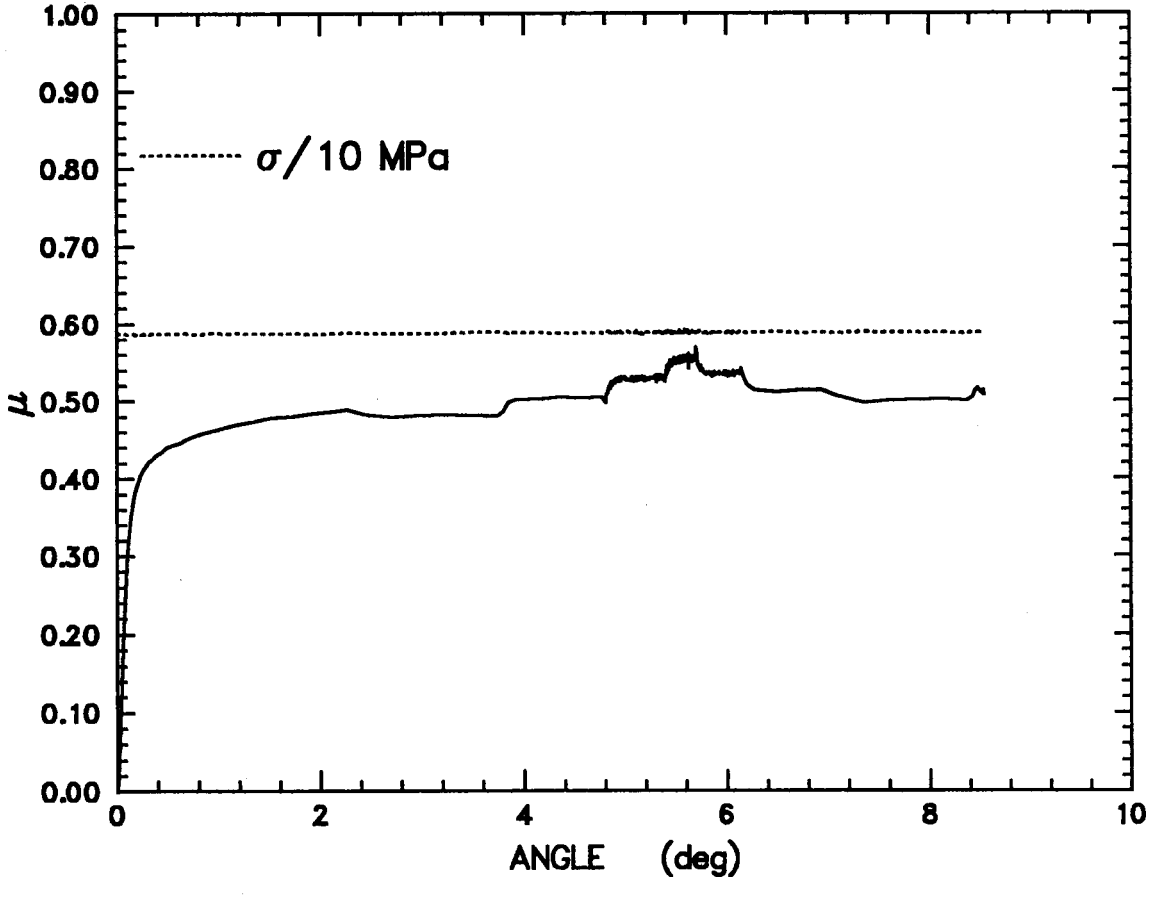

Figure 82: Experiment RFT028, velocity-history test.

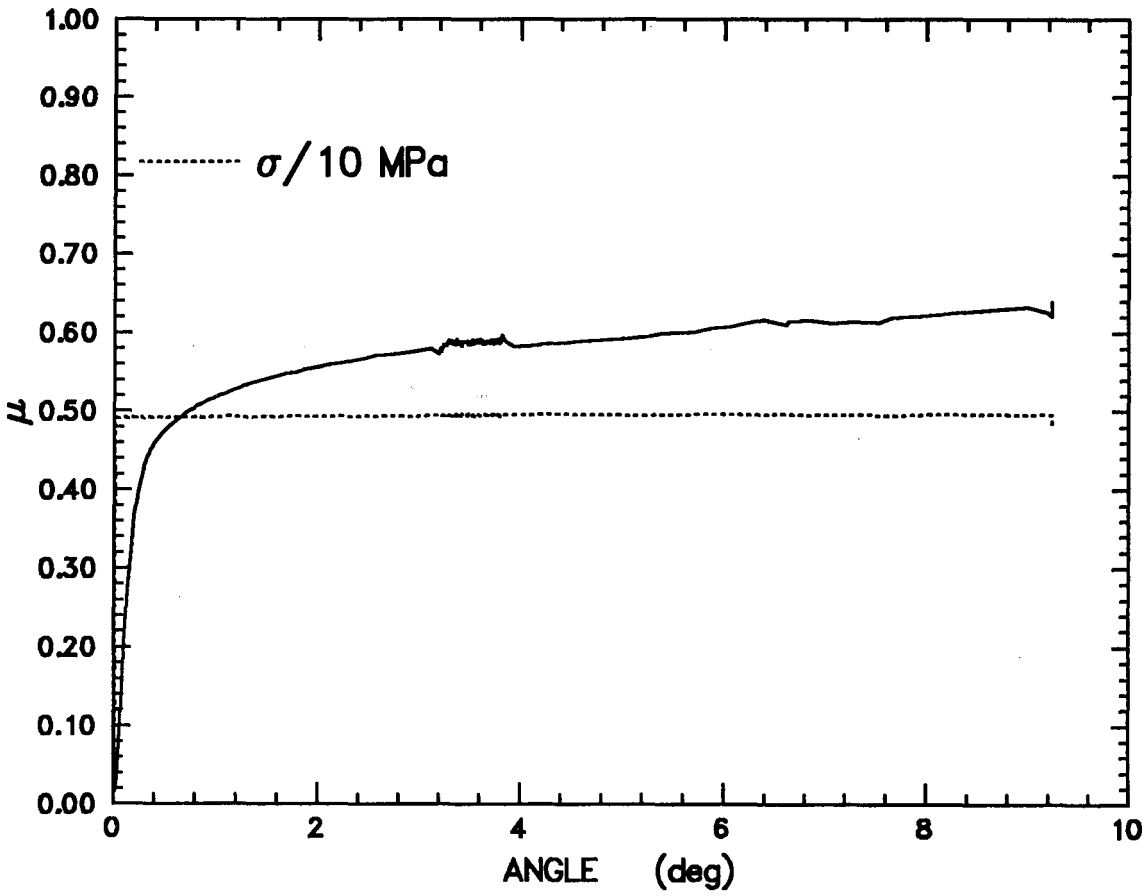

Figure 83: Experiment RFT038, velocity-history test.

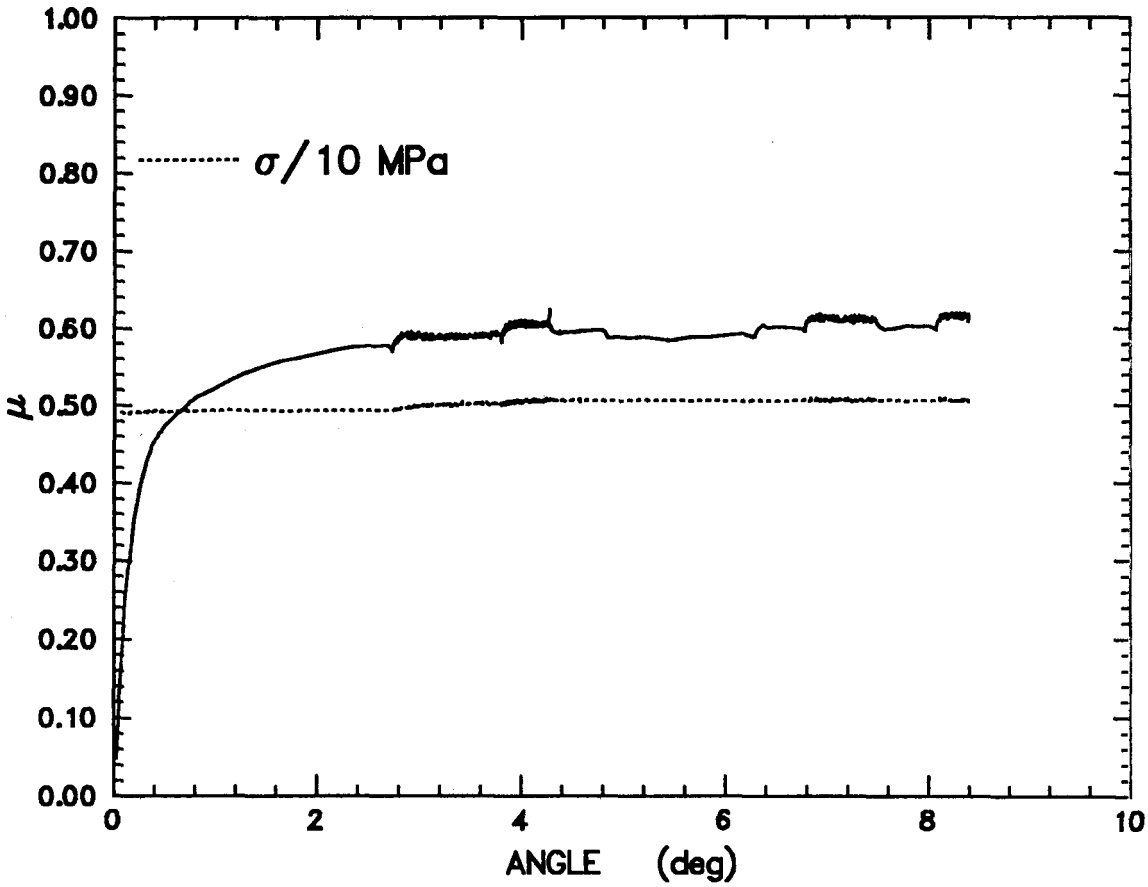

Figure 84: Experiment RFT043, velocity-history test.

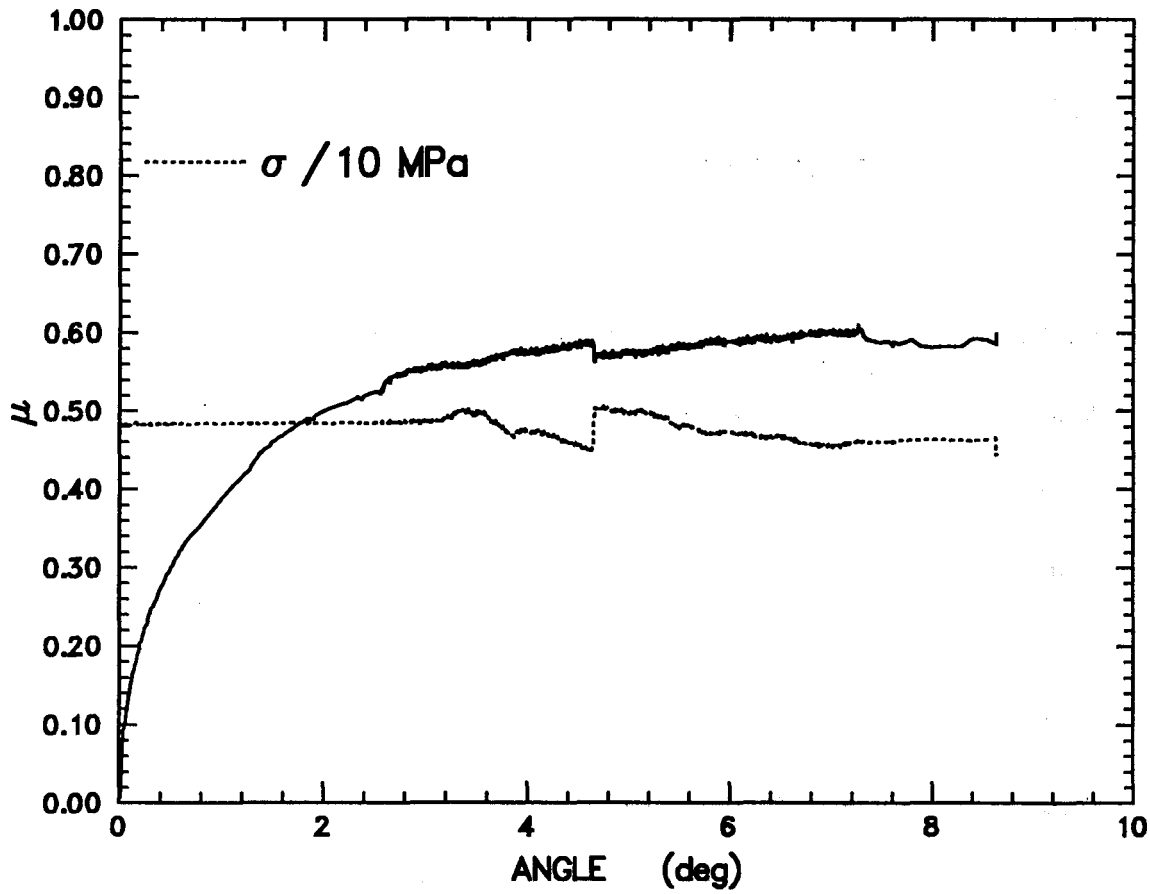

Figure 85: Experiment RFT054, velocity-history test.

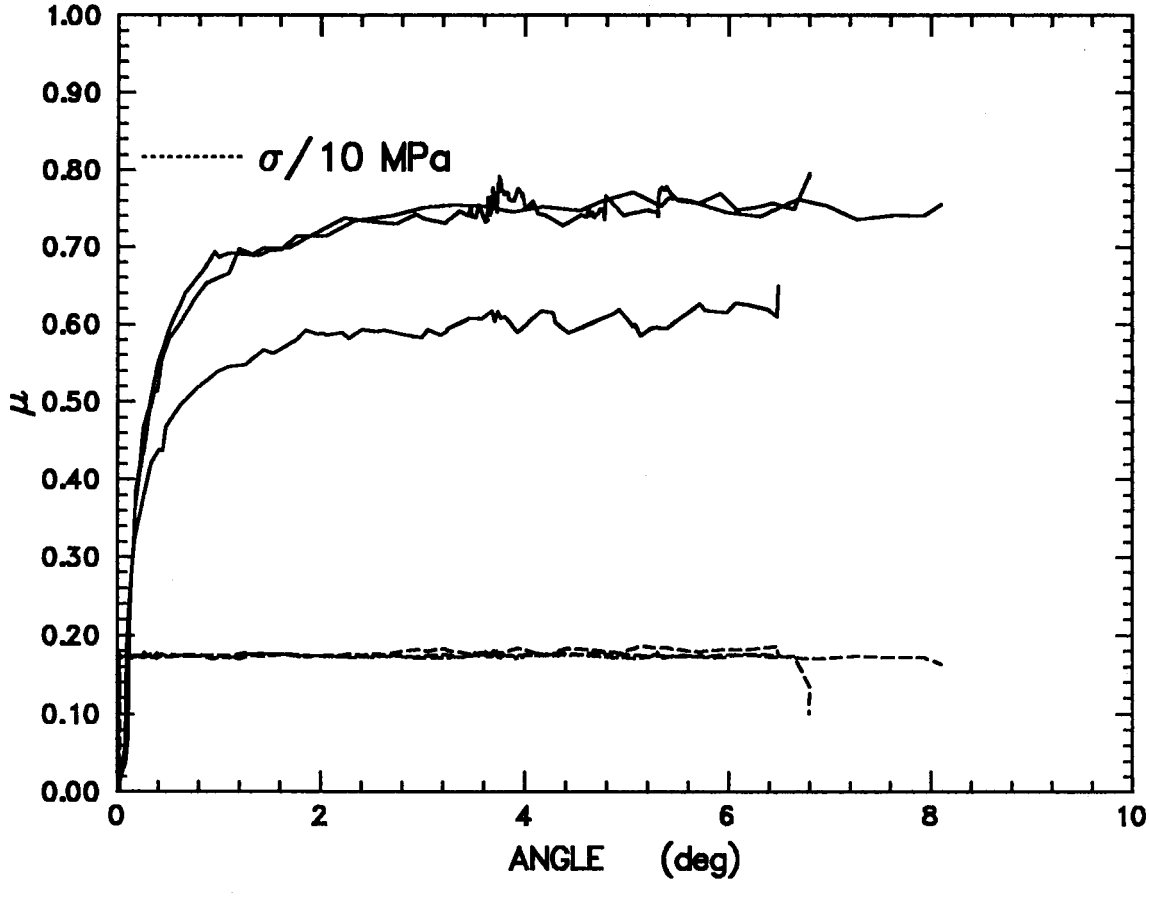

Figure 86: Experiment RFT083, velocity-history test.

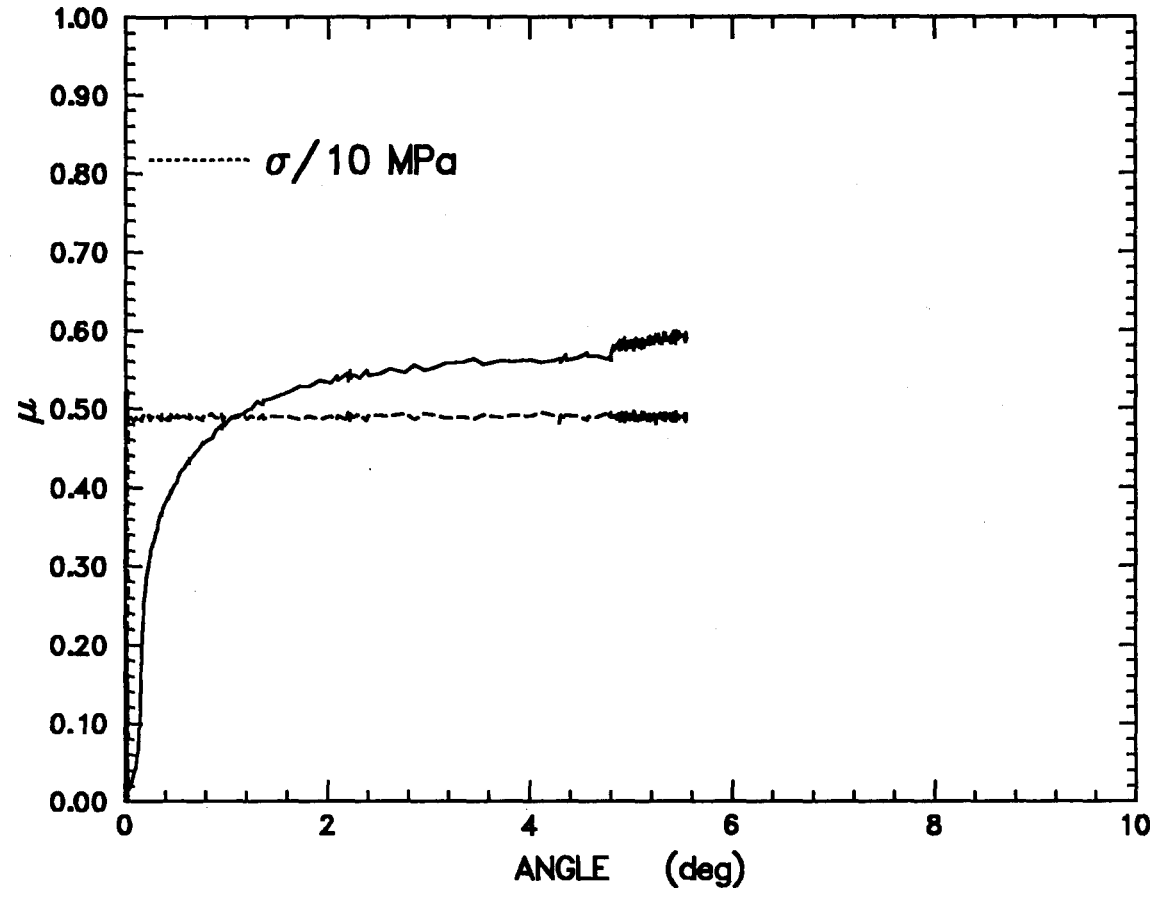

Figure 87: Experiment RFT084, velocity-history test.

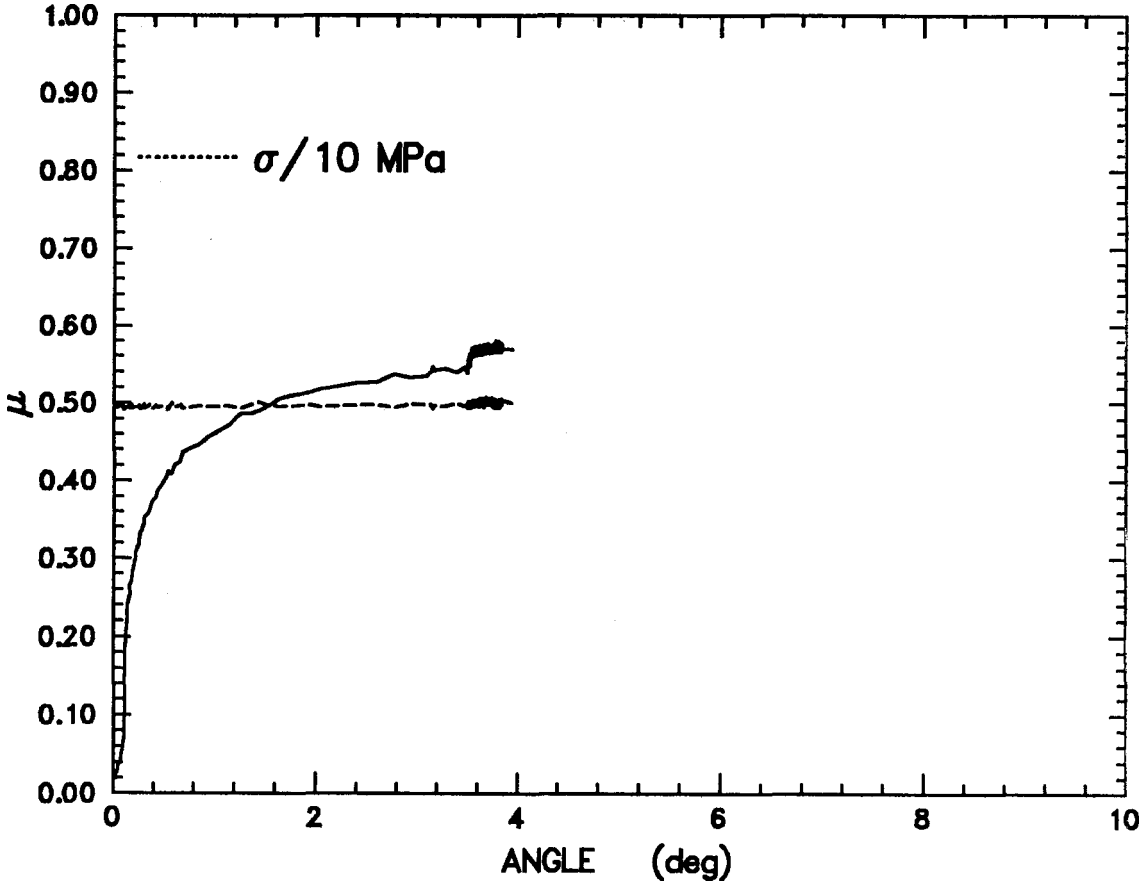

Figure 88: Experiment RFT085, velocity-history test.

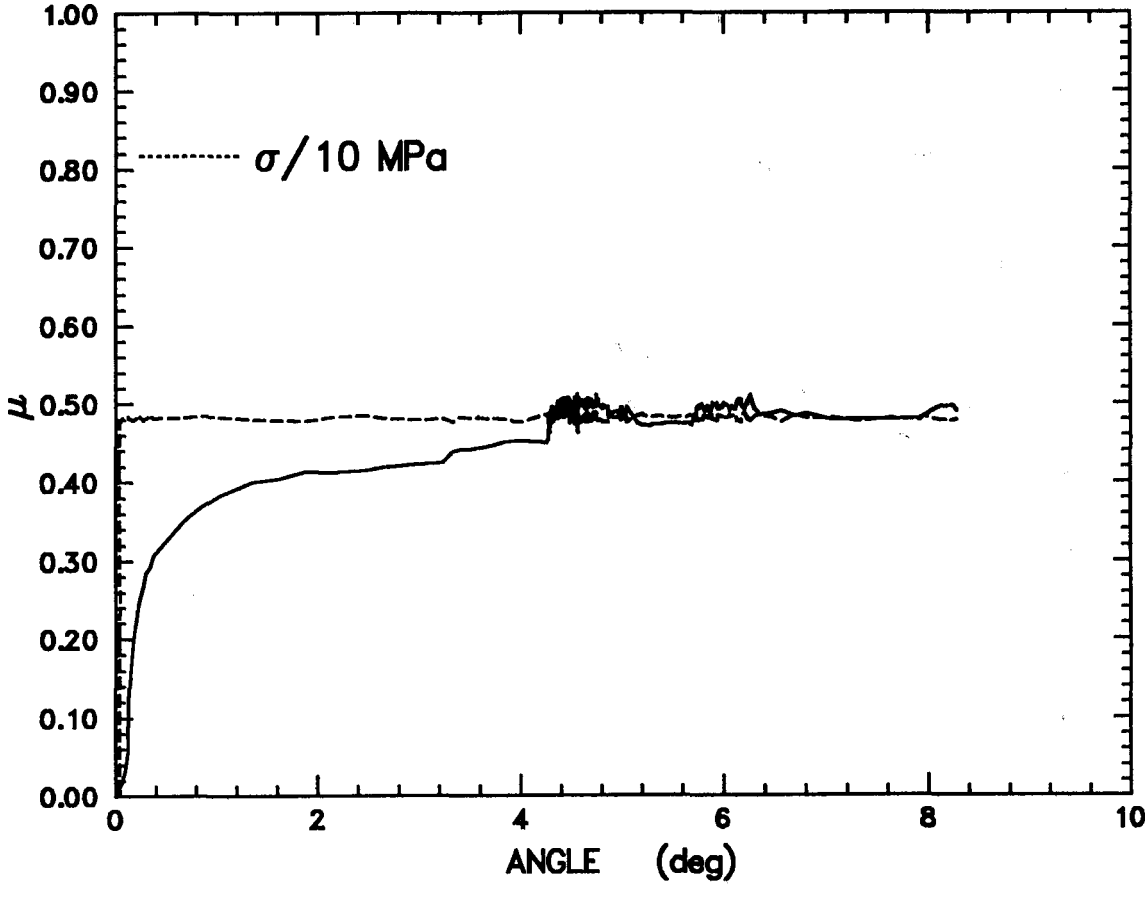

Figure 89: Experiment RFT086, velocity-history test.

DISTRIBUTION LIST

Samuel Rousso, Acting Director (RW-1)
Office of Civilian Radioactive
Waste Management
U.S. Department of Energy
Forrestal Bldg.
Washington, D.C. 20585

Ralph Stein (RW-30)
Office of Civilian Radioactive
Waste Management
U.S. Department of Energy
Forrestal Bldg.
Washington, D.C. 20585

M. W. Frei (RW-22)
Office of Civilian Radioactive
Waste Management
U.S. Department of Energy
Forrestal Bldg.
Washington, D.C. 20585

B. G. Gale (RW-23)
Office of Civilian Radioactive
Waste Management
U.S. Department of Energy
Forrestal Bldg.
Washington, D.C. 20585

F. G. Peters (RW-10)
Office of Civilian Radioactive
Waste Management
U.S. Department of Energy
Forrestal Bldg.
Washington, D.C. 20585

J. D. Saltzman (RW-20)
Office of Civilian Radioactive
Waste Management
U.S. Department of Energy
Forrestal Bldg.
Washington, D.C. 20585

S. J. Brocoum (RW-221)
Office of Civilian Radioactive
Waste Management
U.S. Department of Energy
Forrestal Building
Washington, D.C. 20585

V. J. Cassella (RW-123)
Office of Civilian Radioactive
Waste Management
U.S. Department of Energy
Forrestal Bldg.
Washington, D.C. 20585

S. H. Kale (RW-20)
Office of Civilian Radioactive
Waste Management
U.S. Department of Energy
Forrestal Bldg.
Washington, D.C. 20585

T. H. Isaacs (RW-40)
Office of Civilian Radioactive
Waste Management
U.S. Department of Energy
Forrestal Bldg.
Washington, D.C. 20585

D. H. Alexander (RW-332)
Office of Civilian Radioactive
Waste Management
U.S. Department of Energy
Forrestal Bldg.
Washington, D.C. 20585

C. Bresee (RW-10)
Office of Civilian Radioactive
Waste Management
U.S. Department of Energy
Forrestal Bldg.
Washington, D.C. 20585

Gerald Parker (RW-333)
Office of Civilian Radioactive
Waste Management
U.S. Department of Energy
Forrestal Bldg.
Washington, D.C. 20585

Chief, Repository Projects Branch
Division of Waste Management
U.S. Nuclear Regulatory Commission
Washington, D.C. 20555

NTS Section Leader
Repository Project Branch
Division of Waste Management
U.S. Nuclear Regulatory Commission
Washington, D.C. 20555

Document Control Center
Division of Waste Management
U.S. Nuclear Regulatory Commission
Washington, D.C. 20555

Carl P. Gertz, Project Manager (5)
Yucca Mountain Project Office
Nevada Operations Office
U.S. Department of Energy
Mail Stop 523
P.O. Box 98518
Las Vegas, NV 89193-8518

T. H. Beall (12)
Technical Information office
Nevada Operations Office
U. S. Department of Energy
P.O. Box 98518
Las Vegas, NV 89193-8518

C. L. West, Director
Office of External Affairs
U.S. Department of Energy
Nevada Operations Office
P.O. Box 98518
Las Vegas, NV 89193-8518

W. M. Hewitt, Program Manager
Roy F. Weston, Inc.
955 L'Enfant Plaza, Southwest
Suite 800
Washington, D.C. 20024

Technical Information Center
Roy F. Weston, Inc.
955 L'Enfant Plaza, Southwest
Suite 800
Washington, D.C. 20024

L. B. Ballou (3)
Actg. Technical Project Officer for YMP
Lawrence Livermore National Laboratory
Mail Stop L-204
P.O. Box 808
Livermore, CA 94550

N. E. Carter
Actg. Technical Project Officer for YMP
Science Applications International Corp.
101 Convention Center Dr.
Suite 407
Las Vegas, NV 89109

H. N. Kalia
Exploratory Shaft Test Manager
Los Alamos National Laboratory
Mail Stop 527
101 Convention Center Dr.
Suite P230
Las Vegas, NV 89109

D. T. Oakley (4)
Technical Project Officer for YMP
Los Alamos National Laboratory
N-5, Mail Stop J521
P.O. Box 1663
Los Alamos, NM 87545

L. R. Hayes (6)
Technical Project Officer for YMP
U.S. Geological Survey
P.O. Box 25046
421 Federal Center
Denver, CO 80225

K. W. Causseaux
NHP Reports Chief
U.S. Geological Survey
P.O. Box 25046
421 Federal Center
Denver, CO 80225

R. V. Watkins, Chief
Project Planning and Management
U.S. Geological Survey
P.O. Box 25046
421 Federal Center
Denver, CO 80225

Center for Nuclear Waste
Regulatory Analyses
6220 Culebra Road
Drawer 28510
San Antonio, TX 78284

R. L. Bullock
Technical Project Officer for YMP
Fenix & Scisson, Inc.
Mail Stop 403
101 Convention Center Dr.
Suite P250
Las Vegas, NV 89193-3265

James C. Calovini
Technical Project Officer for YMP
Holmes & Narver, Inc.
101 Convention Center Dr.
Suite 860
Las Vegas, NV 89109

Dr. David W. Harris
YMP Technical Project Officer
Bureau of Reclamation
P.O. Box 25007 Bldg. 67
Denver Federal Center
Denver, CO 80225-0007

M. D. Voegele
Science Applications International
Corp.
101 Convention Center Dr.
Suite 407
Las Vegas, NV 89109

J. A. Cross, Manager
Las Vegas Branch
Fenix & Scisson, Inc.
P.O. Box 93265
Mail Stop 514
Las Vegas, NV 89193-3265

P. T. Prestholt
NRC Site Representative
1050 East Flamingo Road
Suite 319
Las Vegas, NV 89119

A. E. Gurrola, General Manager
Energy Support Division
Holmes & Narver, Inc.
P.O. Box 93838
Mail Stop 580
Las Vegas, NV 89193-3838

A. M. Sastry
Technical Project Officer for YMP
MAC Technical Services
Valley Bank Center
101 Convention Center Drive
Suite P-113
Las Vegas, NV 89109

B. L. Fraser, General Manager
Reynolds Electrical & Engineering Co.
P.O. Box 98521
Mail Stop 555
Las Vegas, NV 89193-8521

P. K. Fitzsimmons, Director
Health Physics & Environmental
Division
Nevada Operations Office
U.S. Department of Energy
P.O. Box 98518
Las Vegas, NV 89193-8518

Robert F. Pritchett
Technical Project Officer for YMP
Reynolds Electrical & Engineering Co.
Mail Stop 615
P.O. Box 98521
Las Vegas, NV 89193-8521

Elaine Ezra
YMP GIS Project Manager
EG&G Energy Measurements, Inc.
P.O. Box 1912
Mail Stop H-02
Las Vegas, NV 89125

SAIC-T&MSS Library (2)
Science Applications International
Corp.
101 Convention Center Dr.
Suite 407
Las Vegas, NV 89109

Dr. Martin Mifflin
Desert Research Institute
Water Resources Center
2505 Chandler Avenue
Suite 1
Las Vegas, NV 89120

E. P. Binnall
Field Systems Group Leader
Building 50B/4235
Lawrence Berkeley Laboratory
Berkeley, CA 94720

J. F. Divine
Assistant Director for
Engineering Geology
U.S. Geological Survey
106 National Center
12201 Sunrise Valley Dr.
Reston, VA 22092

V. M. Glanzman
U.S. Geological Survey
P.O. Box 25046
913 Federal Center
Denver, CO 80225

C. H. Johnson
Technical Program Manager
Nuclear Waste Project Office
State of Nevada
Evergreen Center, Suite 252
1802 North Carson Street
Carson City, NV 89710

T. Hay, Executive Assistant
Office of the Governor
State of Nevada
Capitol Complex
Carson City, NV 89710

R. R. Loux, Jr., (3)
Executive Director
Nuclear Waste Project Office
State of Nevada
Evergreen Center, Suite 252
1802 North Carson Street
Carson City, NV 89710

John Fordham
Desert Research Institute
Water Resources Center
P.O. Box 60220
Reno, NV 89506

Prof. S. W. Dickson
Department of Geological Sciences
Mackay School of Mines
University of Nevada
Reno, NV 89557

J. R. Rollo
Deputy Assistant Director for
Engineering Geology
U.S. Geological Survey
106 National Center
12201 Sunrise Valley Dr.
Reston, VA 22092

Eric Anderson
Mountain West Research-Southwest
Inc.
Phoenix Gateway Center
432 North 44 Street
Suite 400
Phoenix, AZ 85008-6572

Judy Foremaster (5)
City of Caliente
P.O. Box 158
Caliente, NV 89008

A. T. Tamura
Science and Technology Division
Office of Scientific and Technical
Information
U.S. Department of Energy
P.O. Box 62
Oak Ridge, TN 37831

L. Jardine
Project Manager
Bechtel National Inc.
P.O. Box 3965
San Francisco, CA 94119

R. Harig
Parsons Brinckerhoff Quade &
Douglas
1625 Van Ness Ave.
San Francisco, CA 94109-3679

Dr. Roger Kasperson
CENTED
Clark University
950 Main Street
Worcester, MA 01610

Robert E. Cummings
Engineers International, Inc.
P.O. Box 43817
Tucson, AZ 85733-3817

Dr. Jaak Daemen
Department of Mining and
Geotechnical Engineering
University of Arizona
Tucson, AZ 85721

Department of Comprehensive Planning
Clark County
225 Bridger Avenue, 7th Floor
Las Vegas, NV 89155

Economic Development Department
City of Las Vegas
400 East Stewart Avenue
Las Vegas, NV 89109

Planning Department
Nye County
P.O. Box 153
Tonopah, NV 89049

Director of Community Planning
City of Boulder City
P.O. Box 367
Boulder City, NV 89005

Commission of the European
Communities
200 Rue de la Loi
B-1049 Brussels
Belgium

Lincoln County Commission
Lincoln County
P.O. Box 90
Pioche, NV 89043

Community Planning & Development
City of North Las Vegas
P.O. Box 4086
North Las Vegas, NV 89030

City Manager
City of Henderson
Henderson, NV 89015

ONWI Library
Battelle Columbus Laboratory
Office of Nuclear Waste Isolation
505 King Avenue
Columbus, OH 43201

Librarian
Los Alamos Technical
Associates, Inc.
P.O. Box 410
Los Alamos, NM 87544

Dr. N. L. Carter, Director
Center for Tectonophysics
Texas A & M University
College Station, TX 77843

D. K. Parrish
RE/SPEC, Inc.
Post Office Box 14984
Albuquerque, NM 87191

J. D. Blacic
Los Alamos National Laboratory
Post Office Box 1663
Mail Stop J-980
Los Alamos, NM 87545

J. D. Weeks
Box 1846
Geology Department
Brown University
Providence, RI 02912

T. E. Tullis
Box 1846
Geology Department
Brown University
Providence, RI 02912

A. L. Ruina
TAM
Thurston Hall
Cornell University
Ithaca, NY 14853

J. D. Byerlee
MS 77
NCER
U. S. Geological Survey
345 Middlefield Rd.
Menlo Park, CA 94025

D. Lockner
MS 77
U. S. Geological Survey
345 Middlefield Rd.
Menlo Park, CA 94025

J. H. Dieterich
U. S. Geological Survey
345 Middlefield Rd.
Menlo Park, CA 94025

J. M. Logan
Center for Tectonophysics
Texas A & M University
College Station, TX 77843

E. C. Drumm
Department of Civil Engineering
110C Perkins Hall
The University of Tennessee
Knoxville, TX 37996-2010

1521 R. D. Krieg
1523 E. P. Chen
3141 S. A. Landenberger (5)
3154-1 C. L. Ward (8) for DOE/OSTI
3151 W. I. Klein (3)
6240 W. C. Luth
6241 H. C. Hardee
6242 S. R. Brown
6242 D. J. Holcomb
6242 W. A. Olsson (10)
6242 L. W. Teufel
6242 W. R. Wawersik
6242 D. H. Zeuch
6243 T. M. Gerlach
6300 R. W. Lynch
6300-1 T. O. Hunter
6300 100/124213/SAND88-0660/TBD
6300 YMPCRF
6311 A. L. Stevens
6311 C. Mora
6312 F. W. Bingham
6313 T. E. Blejwas
6313 R. E. Finley
6313 F. B. Nimick
6313 R. H. Price
6314 J. R. Tillerson
6314 S. J. Bauer
6314 L. S. Costin
6315 L. E. Shephard
6316 R. P. Sandoval
6317 S. Sinnock
7541 R. M. Zimmerman
6332 WMT Library (20)
6410 N. R. Ortiz, Actg.
8524 J. A. Wackerly